1-1-2014

A Comprehensive Study Of Nonlinear Effects Of Coupling Materials In Ultrasound Infrared Imaging

Yuyang Song
Wayne State University,

Recommended Citation

Song, Yuyang, "A Comprehensive Study Of Nonlinear Effects Of Coupling Materials In Ultrasound Infrared Imaging" (2014). *Wayne State University Dissertations.* Paper 924.

A COMPREHENSIVE STUDY OF NON-LINEAR EFFECTS OF COUPLING MATERIALS IN SONICIR IMAGING

by

YUYANG SONG

DISSERTATION

Submitted to the Graduate School

of Wayne State University,

Detroit, Michigan

in partial fulfillment of the requirements

for the degree of

DOCTOR OF PHILOSOPHY

2014

MAJOR: ELECTRICAL ENGINEERING

Approved by:

Advisor Date

ACKNOWLEDGMENTS

First of all, I would like to express my special appreciation and thanks to my Advisor, Professor Xiaoyan Han. You have been a tremendous mentor for me. I would like to thank you for encouraging my research and for allowing me to grow as a research scientist. Your knowledge and logical way of thinking have been of great value for me and provided a good basis for this research. Your advice on both my research and life has been priceless.

Warm thanks should also give to Professor Lawrence ’Skip’ Favro, for his valuable advice and friendly help. His extensive discussions around my study at Xiaoyan’s Group have shed light on the path of this thesis work.

My sincere thanks are due to the members of my doctoral dissertation committee, Professor John Liu, Ph.D., Professor Golam Newaz, Ph.D., and Professor Mark.Cheng, Ph.D., for their invaluable time and patience to help me get through this thesis work.

During my study as a PhD student in the lab, I have collaborated with many colleagues for whom I have great regard. I like to thank my colleagues and also friends — Wei Li, Qi He, A.SAbhijith ,Zeeshan Ahmed, Xinyue Zhao and Ding Zhang for their help and friendship. Special thanks should also goes to Anthony Lubowicki, without your help for the experimental suggestions and handy work, these thesis can not be finished. And I wish to extend my warmest thanks to all those who have helped me with my work.

I owe my loving thanks to my wife Qianqian Chen, my sons Carter Song. They had sacrificed so much for me. Their love and support without any complaint or regret has enabled me to complete this project. Without their encouragement and understanding it would have been impossible for me to finish this work.

My special gratitude is due to my father, Shulin Song, my mother, Liming Liu, my sister Yuyan Song, and my father in-law, Youliang Chen, mother-in-law, Shuhua Yang for their loving and selfless support.

This project was sponsored in part by the DOT/FAA William J. Hughes Technical Center's Airworthiness Assurance Center of Excellence. The financial supports by them are gratefully acknowledged.

TABLE OF CONTENTS

LIST OF TABLES

CHAPTER ONE

INTRODUCTION

1. Introduction to Nondestructive Evaluation

Nondestructive Evaluation (NDE), also called Nondestructive Testing (NDT) and Nondestructive Inspection (NDI), refers to technologies that evaluate or inspect the test object while not destroy it [1]. It is a multi-disciplinary study for the investigating of cracks/defects in different components. Ultrasonic, radiographic, electromagnetic, and optic methods are employed to probe interior microstructure and characterize subsurface features such as cracking and corrosion [2]. NDT examines and analyze any materials, components or structures, reveals the presence of defects which can be evaluated against safety criteria. It is the major tools in quality control and safety assurance extensively applied in industries from defense, to aerospace to automotive and to power generation. NDE plays the important role not only in the quality control of the finish products but also during various stages of manufacturing. Through the effective and reliable use of NDT methods, the modern concepts like total quality management that aimed to obtain almost defect free components, is possible. NDT is also used for condition monitoring of various items during operation to predict and assess the remaining life of the component while retaining its structural integrity [3]. The commonly used methods are showed bellowing [4]:

LIQUID PENETRANT TESTING (PT):

PT can check surface or subsurface cracks. Usually, a brightly dye liquid is sprayed to the target's surface. Because of capillary effect, the liquid is pressed into cracks. After enough long time, the surplus penetrant media is cleaned and a different developer (usually chalk poser) is spayed. Due to reverse capillary effect, the powder is drawn out of the crack, resulting in a much more visible colored indication on the surface. This technique is widely used to detect surface defects[4].

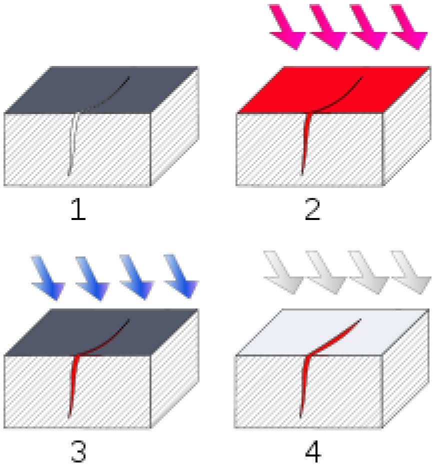

Figure 1.1 PT testing method principles

MAGNETIC PARTICLE TESTING (MT):

MT is good at detecting surface/sub-surface cracks/defects in ferrous materials. This method applies magnetic field on materials and visible ferrous particles are sprayed on the sample surface at same time. The defects in a surface of the target cause discontinuities in the magnetic flow. Such distortion at this location will cause loss of the magnetic and give clues for cracks. [4]

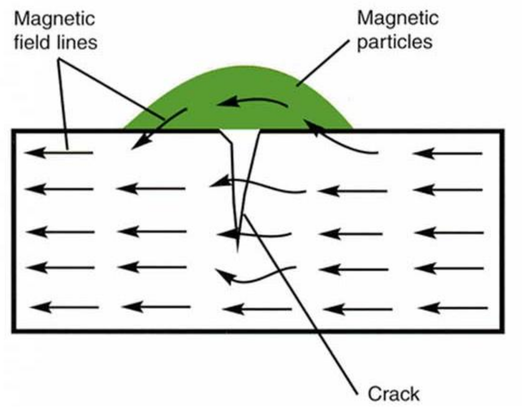

Figure 1.2 Schematic showing of MT techniques

EDDY CURRENT TESTING (ET):

Eddy current testing can be used to detect cracks/defects in thin metal materials. This technology can also be used for thickness measurements for sheet metals used in aerospace industry. It has both field portable and fixed system instruments. This technology can examine large areas very quickly without any coupling liquids. But this technology is limited to metals and cannot be used on plastics. [4].

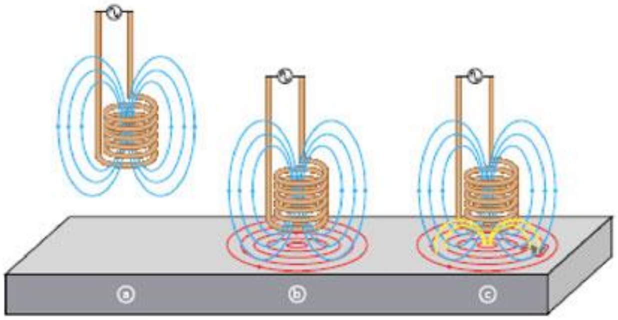

a—The alternating current flowing through the coil at a chosen frequency generates a magnetic field around the coil.

b—When the coil is placed close to an electrically conductive material, eddy current is induced in the material.

c—If a flaw in the conductive material disturbs the eddy current circulation, the magnetic coupling with the probe is changed and a defect signal can be read by measuring the coil impedance variation.

Fig.1.3 Schematic showing of ET techniques

RADIOGRAPHIC TESTING (RT):

This NDE technology uses X-rays produced by an X-ray tube. The basic principle of such NDE inspection technology is similar with that for medical radiography. Radiation is penetrated through a weld solid object projected to a photographic film. The image is obtained through the film the internal structure. The amount of energy absorbed by the object depends on its density and thickness. Energy passed through the object will be dark after the film is developed. The thickness changes due to cracks/discontinuities in the object will appear as dark when they are filmed [4].

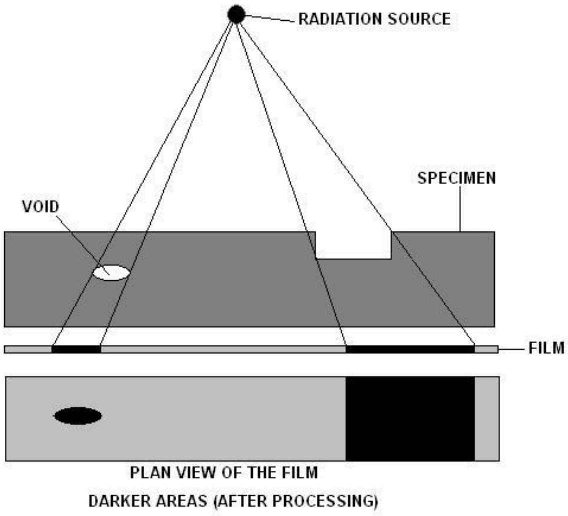

Fig.1.4 Schematic showing of RT techniques

ULTRASONIC TESTING (UT):

UT can be used to test materials which can transmit mechanical vibrations. It can detect all kind of flaws and permits three dimensional interpretations. The principle of UT technology is conversion of electronic pulse to mechanical vibrations. Because of their different acoustic nature, the flaws can reflect returning different pulses, which are re-converted to electric energy and displayed as signals. The position and size of the flaws is determined from the location/size of the reflected signals [4].

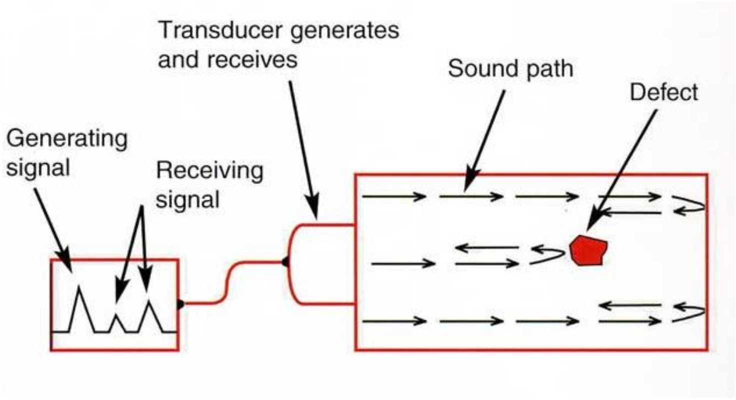

Fig.1.5 Schematic showing of UT techniques

2. Sonic Infrared (IR) imaging Technique

Only a few years old in the non-destructive evaluation family, Sonic Infrared (IR) Imaging is already proven as a powerful NDE technique for detecting surface or subsurface defects such as cracks, delimitations, and disbands in metals, composites, coatings, and ceramics. In this technique, an ultrasound vibration with a frequency range from 20 kHz to 40 kHz is applied on a target material within a second. The traveled ultrasonic sound waves through defects cause rubbing and clapping of the surface. Such frictional vibration creates heat in the crack area, which can be detected and recorded by modern IR camera [5]. The sequence of this technique is shown in Figure 1.6.

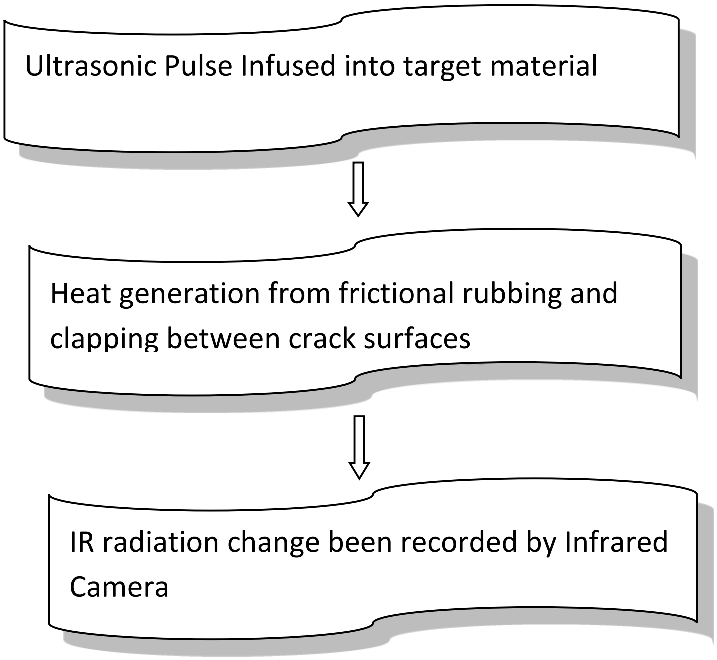

Figure 1.6 Flowchart of the Sonic IR Imaging technique.

The technique has proven to be a powerful tool for detecting surface and subsurface cracks, and disbonds in metallic and composite materials [5-8]. The minimum detected crack so far is 20μm. Besides, it is much faster than other techniques. The general processing time for this technique is less than 1 minute. The NDE research group in Wayne State University, where this technique was invented, has detected flaws from aircraft parts (jet engines, turbine blades, etc), automotive specimens etc[6]. Some of the samples are shown in Figure 1.7. There are tiny surface or subsurface cracks in these samples, which are invisible to our naked eyes, while these cracks are obvious in IR image system as a comparison in the figure 1.8.

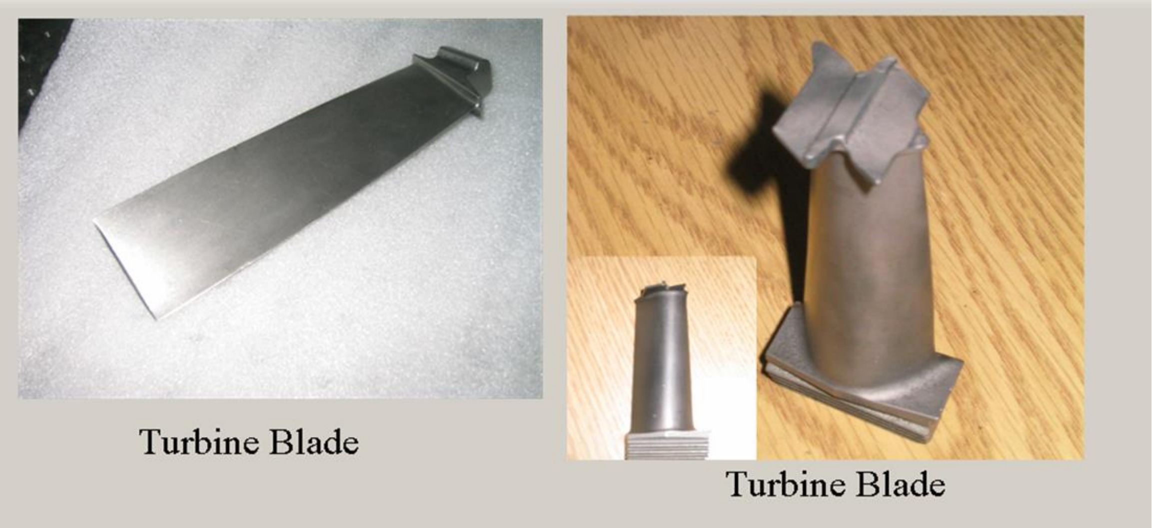

Figure 1.7 samples with defects

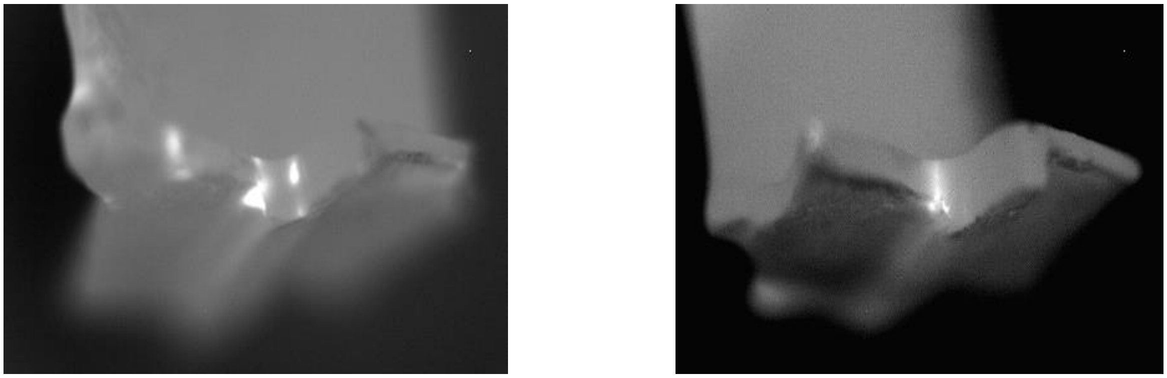

Figure 1.8 Flaw detection by Sonic IR Imaging technique

3. Literature review on coupling materials research of Sonic IR imaging system

Quantitative NDE analysis has been a big trend in NDE development, which is also a critic research topic in this area. Different quantitative analysis techniques had been developed for different NDE techniques, especially in the detection of the length and depth of cracks in different materials. Huge results had been published on quantitative NDE in other field such as Acoustic Emission, ultrasonic [1, 3, 4] etc. Till now, quantitative research is just limited on the detection of the length of the cracks; the depth of the crack is also a mystery for most of the NDE researchers. As a novel non-destructive evaluation technique, Sonic IR imaging has been improved significantly since its invention. Meanwhile, quantitative characterization of Sonic IR techniques has also been developed. In SonicIR Imaging system, the ultrasonic pulse is introduced into the specimen by the ultrasonic power supply, which can be considered as the input; the vibration velocity from the crack and the infrared signal captured by the IR camera can be taken as the output of the system. The importance of finding out quantitative relationships between them is above mentioned. The change of input parameters can effect the output in various ways and thus influence the detect ability and the ultimate output from the system. Till now, temperature time curve of the infrared image in the defects is developed for the quantitatively characterization of heat propagation. Other quantitative data has been calculated such as thermal energy from the heating in the defects, acoustic energy output from the sample vibration. As for this technique, increasing the efficiency of the system is more realistic and applicable. Obviously, a higher signal to noise ratio means a higher probability of crack detection. Research in producing higher signals is vital for different applications of sonic IR imaging. Factors that affect the IR signal are as follows: the pulse frequency, the coupling material between the ultrasonic transducer and the target, the loading force of the transducer on the target, and the targets own material characteristics (i.e. density, geometry, thermal diffusivity)[9-13] . Coupling materials, which were originally used to prevent from marking the sample in an experiment by the ultrasound transducer, were found important in the course of the development of Sonic IR technology by some of the authors. Research conducted on the coupling materials back a few years ago was limited due to the stage of the technology at the time. Although different kind of coupling materials have been used since the advent of this technique, it has only been recently that the quantitatively analysis is been conducted for different coupling materials in order to optimize the efficiency of the system for a given sample [13-16]. It has been reported in a previous paper that duct tape is more effective than leather. A comprehensive study on the effect of different coupling materials on SonicIR system is needed. Jacob et al. [17] uses this technique with different coupling materials in constant loading force to estimate the fatigue crack propagation under cyclic loading. From his paper, we realize that the loading force between the ultrasound transducer and a coupling material is also a factor. The research on the effect of different loading force for SonicIR system is also needed. In the sonicIR system, the effect of driving frequency is also critical. There are a lot of research on the relationship between heat generation mechanism and the driving frequency [18-19]. G. Busse et al.[20] used frequency modulated ultrasound to improve the detecability of the cracks. Stephen et al.[21,22] reported on the use of different resonant frequency or broadband actuator to increase of the heating of cracks. In our lab, the comprehensive study on the effect of driving frequency on SonicIR system is highly demanded.

4. Objective of the Research Work

There are three major purposes of my research work. One is to investigate the effect of coupling material on the SonicIR system; the second one is to investigate the effect of loading force between transducer and samples; the last one is to investigate the effect of driving frequency to the sonicIR system. Three frequency systems are enrolled in the system, one is 20KHz power supply system, one is 30KHz and the other one is 40KHz power supply system. Most important part of the research is to investigate the non-linear effect of the coupling material in SonicIR system. Six different kinds of coupling materials such as duct tape, laminated business card, nonlaminated business card, Teflon, gasket materials and leather are investigated as commonly used materials in our lab. Quantitatively evaluation of the relationship between the vibrational acoustic energy and thermal energy in the crack is conducted. Meanwhile, FEA (Finite Element Analysis) were used as numerical analysis tools in this study to compare with the experimental data.

The following research results was output during the PhD work:

1) Quantitatively characterization of the ultrasonic IR techniques, thermal energy and acoustic energy of different coupling materials in one frequency at a predefined loading force. The relationship between the vibrational acoustic energy and thermal energy were discussed, Correlation analysis between the acoustic energy and the thermal energy in the crack was researched as well. The physical reason behind the difference for these different coupling materials were investigated and the acoustic impedance theory was proposed.

2) Investigation of the loading force to the non-linear coupling of the SonicIR system. The relationship between the vibrational acoustic energy and thermal energy for different loading force with one coupling material was also discussed. The acoustic energy and thermal energy calculated in the cracks are combined together for the correlation analysis.

3) Investigation of the effect of driving frequency to the non-linear coupling in SonicIR system. Again, quantitative characterization between thermal energy and acoustic energy on this system for different frequency system were compared. The correlation analysis between vibration and thermal image were also used as quantitative characterization tool.

4) Based on the acoustic impedance theory, similar research was conducted on Fan-disk sample. And, the quantitative analysis were formatted based on the comparison matrix similar to Al bar sample.

5) FEA model was developed for Al bar with center-edge crack sample in SonicIR system, the comparison between chaos and no-chaos were discussed. In addition to that, coupling materials were introduced in the model for the first time, the results from the thermal energy and acoustic energy as normal as experimental were quantitatively characterized. Meanwhile, the effect of the input frequency to the SonicIR system was discussed from the perspective of FEA simulation.

CHAPTER TWO

EXPERIMENTAL SETTING

The schematic of the experimental setup is shown in Figure 2. 1. Fig.2.2 and Fig.2.3 show the 3D front view of the settings and the optical image of the settings as well. The major sample used to conduct all the experiments is an aluminum bar with an edge-through crack. The dimension of the sample is 240*40*2.48mm, with the crack length about 10mm. The infrared camera has a focal plane of 640 X 512 pixel array. The transducer is positioned at one end of the Al bar, and the other end of the Al bar is clamped tightly. Different ultrasound systems(20KHz, 30KHz and 40KHz) were used as excitation source to inject ultrasound pulse to the sample. Two laser Doppler vibrometers were pointed and focused at two points across the crack to measure the relative vibration of the crack. A coupling material was always placed between the ultrasound transducer tip and the sample. Typically, about one square inch of a coupling material was used in a Sonic IR experiment. The following coupling materials were chosen from the ones we have experienced with in the past: folded duct tapes (2LayerDT), laminated business cards (LamBC, with plastic films on both sides of the card), non-laminated business cards (NonLamBC, basically paper), Teflon, Gasket material, and leather. Photos of sample materials of these types are shown in Fig.2.4. For each coupling material, the transducer is pushed against on it at a predefined load. Each coupling material is tested twice sequentially without releasing the transducer. In each experiment, the input ultrasound pulse length is set the same, the ultrasound transducer was placed at the same spot on the sample with a coupling material in between, and the camera position was also kept the same.

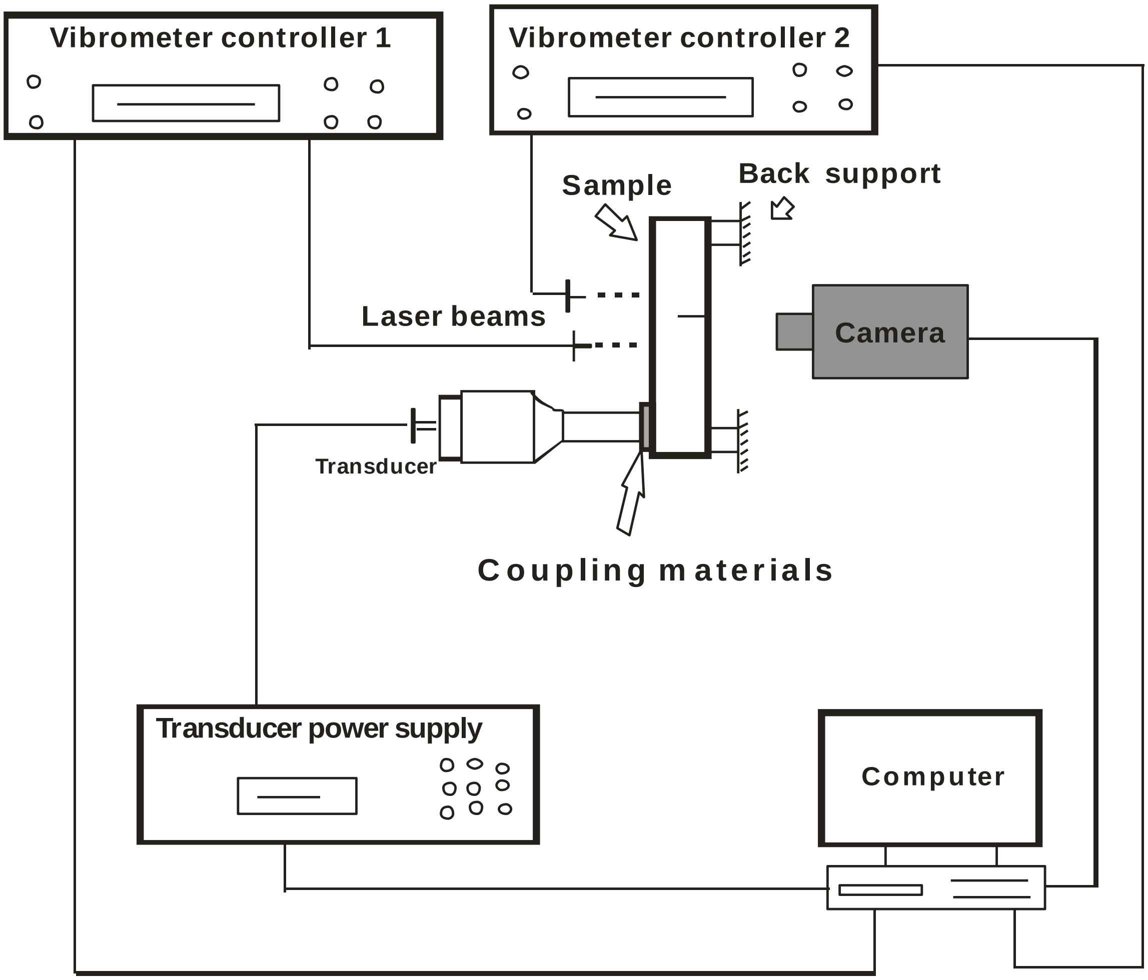

FIGURE 2.1 Schematic drawing of experimental setup

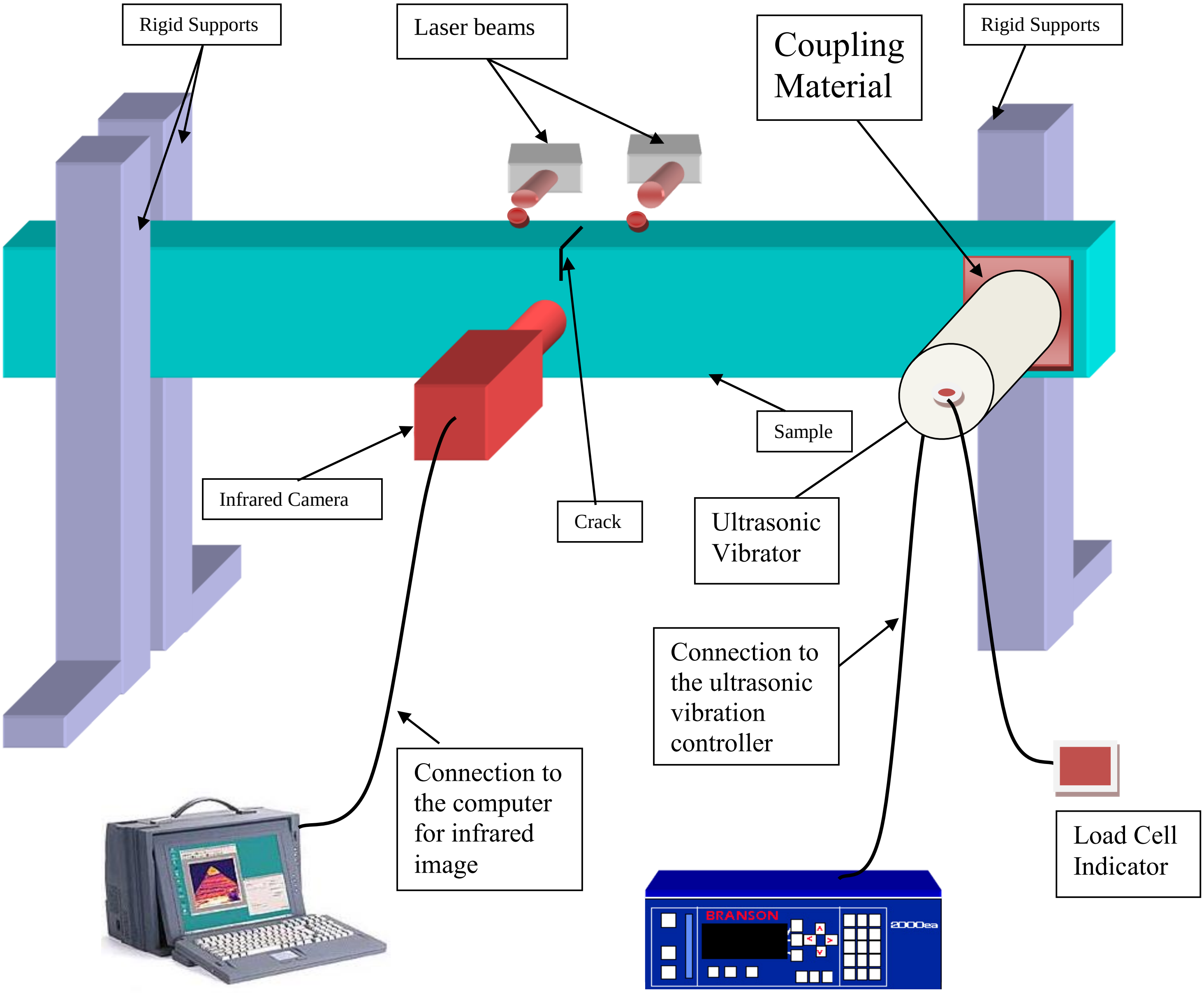

Figure 2.2 3D Front view of the system

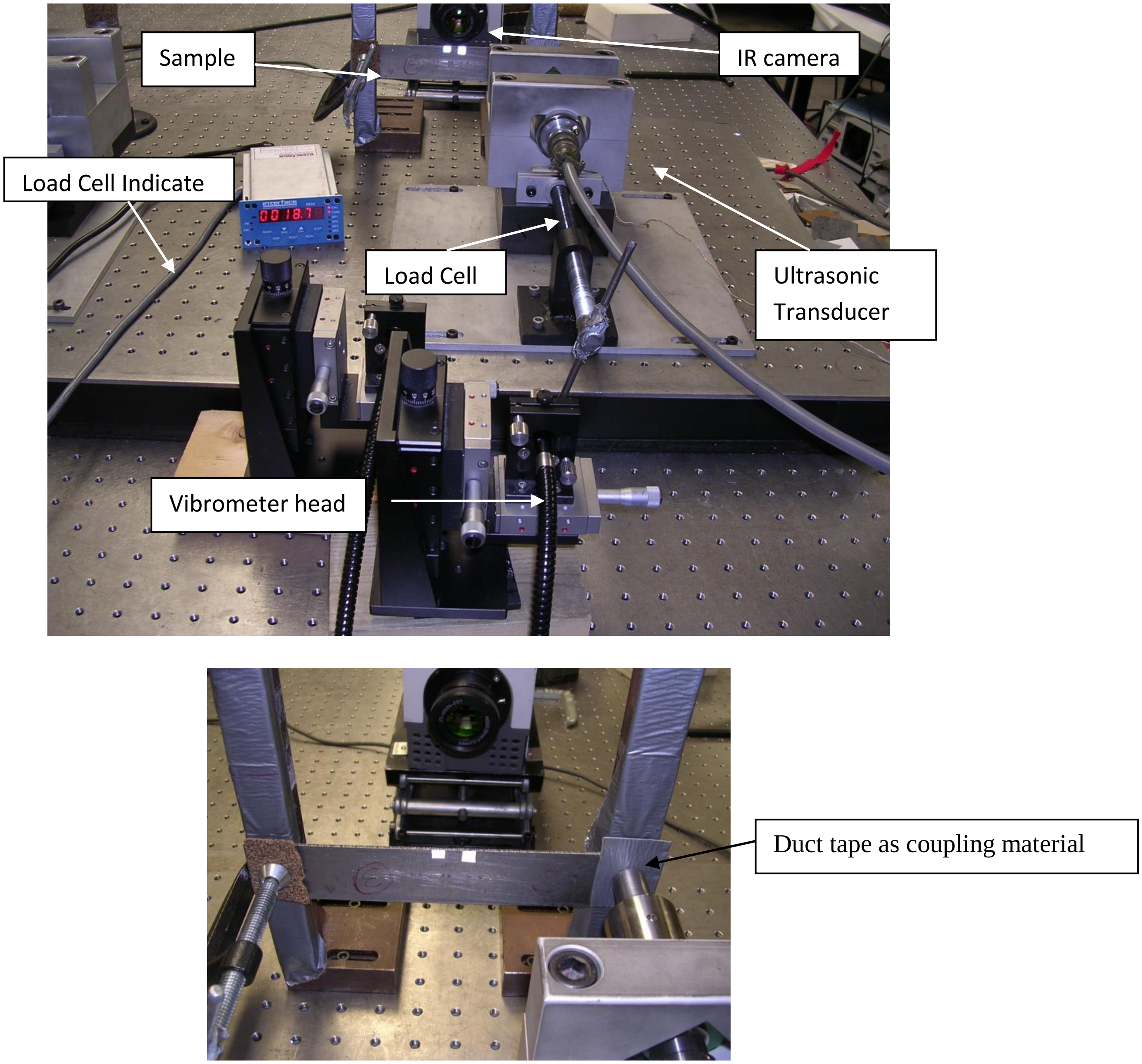

Figure 2.3 Optical Image of the coupling material on Al bar

a .

Folded Single Layer Duct Tape(0.6mm)

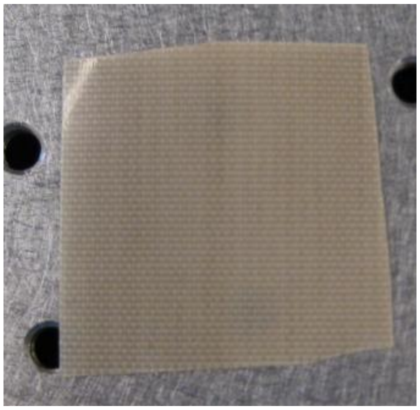

c. Teflon(0.25mm)

威恩州立大學電子與計算機工程系

韓　曉　艷

助 理 教 授

美國密歇根州底特律市
郵編：48202
電話：(313) 577-3646, 3-4335
傳真：(313) 577-1101, 7743
電子信箱：xhan@ece.eng.wayne.edu

b. Laminated Business card (LamBC) 0.11mm (Courtesy of Xiaoyan Han)

WAYNE STATE
UNIVERSITY

ELECTRICAL AND COMPUTER
ENGINEERING
5050 ANTHONY WAYNE DRIVE
DETROIT, MICHIGAN 48202
TEL: (313) 577-3646
LAB: (313) 577-5802, 993-4335
FAX: (313) 577-1101, 7743
XHAN@ENG.WAYNE.EDU

COLLEGE OF
ENGINEERING

XIAOYAN HAN
ASSOCIATE PROFESSOR

d. Nonlaminated Business Card(NonLamBC) 0.33mm (Courtesy of Xiaoyan Han)

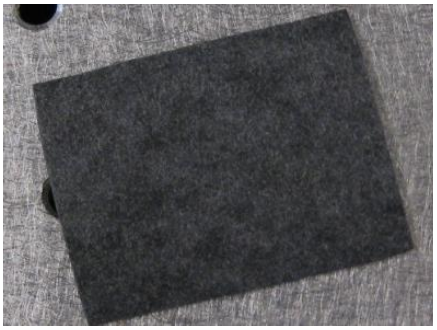

e. f. Gasket Material(0.8mm)

g.leather(1.6mm)

Figure 2.4 Optical Image of coupling materials

Introduction to the system:

Currently Sonic IR Imaging system includes 3 major subsystems: Central Control subsystem, Image-capture subsystem, Ultrasonic Gun subsystem & Power supply subsystem.

1. Central Control subsystem:

Central Control subsystem is the center of the whole system. It contains a computer loaded with camera control software; trigger control software and image analyze software.

Camera Control Software: Phoenix DAS Image-Pro Plus

Trigger control and image analysis software: OldMain (developed in our lab).

2. Image-capture subsystem:

Image-capture subsystem contains the IR cameras and Lens. System employed Indigo Phoenix IR Camera model 9803 and 9803 with 13mm and 25 mm F/2.3 MWIR lens.

IR Cameras:

Phoenix Model 9803 and 9809

Spectral Range (Micron)	1.5~5.0
Resolution (Pixel)	640(H) x 520(V)
Detector Size (um)	25 x 25
Integration Time (us)	<50
Max frame rate	100 fts in full frame; 22 kHz in smallest window(4x128)
Minimum Detectable temperature change (C)	0.02

Table 2-1 Camera Specifications

Lens: INDIGO 13mm F/2.3 MWIR Len

INDIGO 25mm F/2.3 MWIR Len

3. Ultrasonic Gun subsystem & Power supply subsystem [18]:

There are totally 3 types of ultrasonic guns and 2 types of power supplies in service right now. The 20KHz, 30KHz and 40 KHz ultrasonic guns and Branson 900MA 20 kHz ultrasonic welding generator and Branson. A WSU homemade trigger signal generator and synchronization box is connected between this subsystem and the central control computer subsystem for the synchronization of the ultrasonic and the imaging. The Ultrasonic guns are customized from ultrasonic welding equipments, it is made up of a converter, a booster and a horn (or transducer), as shown in Figure2.5. Fig.2.6 shows the Schematic drawing of different power supply frequency system for 20KHz, 30KHz and 40KHz. These drawings show the difference of the frequency system, but the transducer tip all have same size, .75 inch, which makes the impact area all the same.

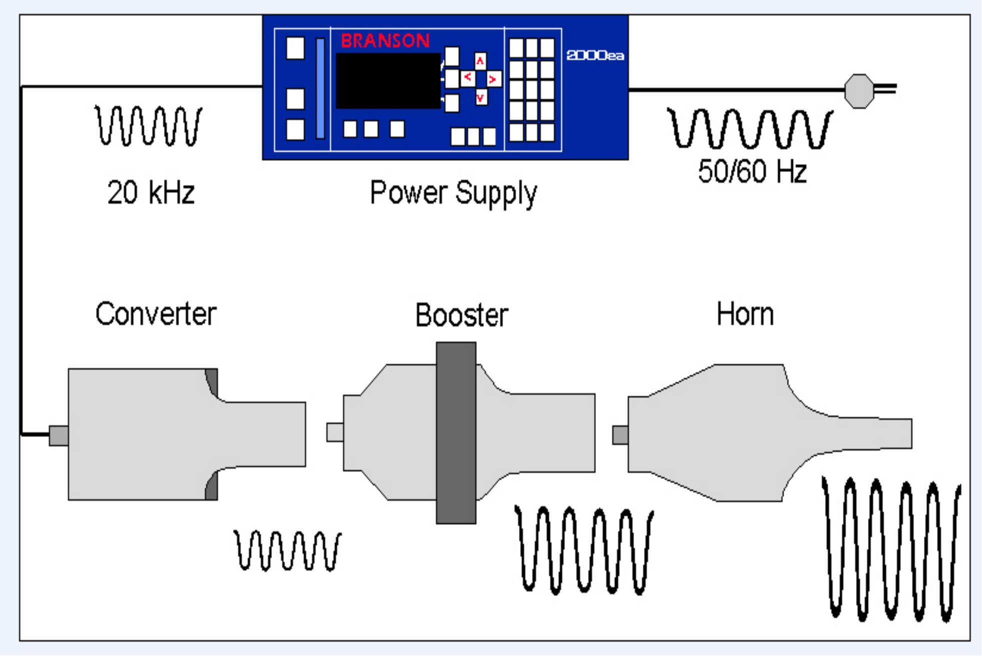

Figure2.5 power supply and components of ultrasonic guns

40 kHz Transducer

30 kHz Transducer

20 kHz Transducer

Fig.2.6 Schematic drawing of different power supply frequency system

4. Strain Indicator subsystem:

In order to get the force between the ultrasonic gun tip and coupling material, a load cell is used. A digital interface is linked to the load cell to get the load force directly.

5. Laser Vibrometer

In order to monitor the vibration of the crack surfaces, laser vibrometers are used to measure the velocities of the crack surfaces or other vibration spot at any position of the sample when the sample is excited by ultrasonic wave.

Laser Type	Helium Neon
Wavelength (nm)	633
Cavity length (mm)	205
Output Center Frequency (MHz)	40
Max Sampling Frequency (KHz)	2560
Maximum Samples	67108864

Table 2-2 Laser Vibrometer Specification

CHAPTER THREE

EXPERIMENTAL RESULTS AND ANALYSIS

3.1Theoretical background

In order to get the quantitative evaluations on results of IR sonic imaging; two basic tools are developed in our lab. One is thermal energy calculation tool; another is acoustic energy calculation tool. Thermal energy comes from the IR image, for the specific area of interests, the higher the thermal energy, the higher the temperature of the sample has.

The formula for the calculation of thermal energy was brought out as [30, 31]

$$\sum\sum P(i,j,t)-\sum\sum B(i,j,t_{0^-}) \quad (1)$$

Here, (i, j) is the pixel at the ith row and jth column. The variable t is the time, B (i, j, t_{0-}) is the initial pixel value before the excitation; it is also called the background. The total thermal energy with the background subtracted can be obtained by summing the above quantity in expression (1) over the time during which the IR image sequence was acquired. The temperature change is directly related to the pixel values in the IR images.

Another useful tool is acoustic energy calculation package, which stands for the energy output from sample vibration. Acoustic energy was calculated according to the following expression [32, 33, 34]:

$$E=\int |S(t)|^2\,dt \quad (2)$$

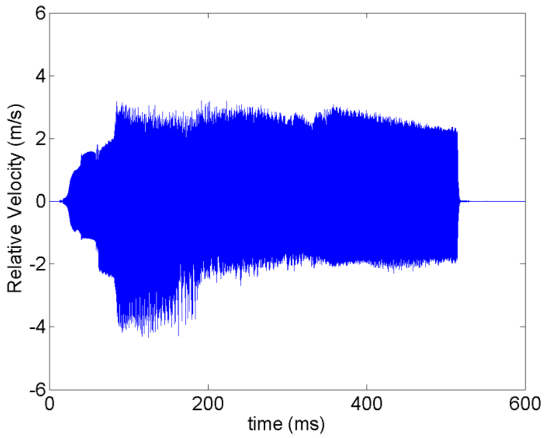

Fig.3.1 Vibration waveform example

Where S(t) is the velocity with respect to time, as we can check out in Figure3.1 from the relative velocity time curve[26]. The velocity of the vibration is acquired from the reflective tape on each side of the crack. The square of the relative velocity is used as a measure of the acoustic power. In turn, the integration over the excitation period can be used as the measure of the acoustic energy. For example, the total acoustic energy for this typical coupling material is 45586.8.

The efficiency of a coupling material is defined as the ratio of acoustic energy and thermal energy [32,33]:

$$TA= {ThermalEnergy}/{AcousticEnergy} \qquad (3)$$

The Camera calibration and temperature calculation

Using the same camera and at the same room temperature, the camera is calibrated to a stable status. Each of the pixel value is calibrated to corresponding temperature with black body which has uniform temperature distribution. Then in the real experimental, using the same camera parameter settings, we can easily calculate the temperature change corresponding to the change of the pixel values. Here, in our experimental, the relationship between the pixel value and the temperature change is:

$$T = pixelvalue \times 4.19 \times 10^{-3}(1 \pm 1.35\%) \qquad (4)$$

6 basic common used coupling materials, which are 2 layer duct tape(2LayerDT), Teflon, laminated business card(LamBC), nonlaminated business card(NonLamBC), gasket materials, leather as shown in Fig.2.6 are used in the experiments. The experiments are conduct on three aspect views as shown in three sections. First, we investigate the effect of the coupling materials in SonicIR, in this section, we use one frequency system(20KHz) and one defined loading force, but compare the experiment results on different coupling materials. Secondly, we focus on the comparison of the loading force in SonicIR system. In this section, we use different loading force but only using one coupling material and one frequency system(20KHz). Thirdly, we focus on the effect of driving frequency on sonicIR system. In this section, we compare the result of different frequency system for different coupling materials in SonicIR system.

3.2 Non-Linear effect of coupling materials on SonicIR at Al bar structure

3.2.1 Effect of coupling materials

In this section, we will discuss the effect of coupling materials on sonicIR system. For each coupling material, the transducer is pushed against on it at a predefined load, which is 168N in our experiment. Each coupling material is tested twice sequentially without releasing the transducer. In each experiment, the input ultrasound pulse length is set the same, the ultrasound transducer was placed at the same spot on the sample with a coupling material in between, and the camera position was also kept the same. The experiment settings are shown in Fig.3.2. The experiment results are interpreted in these aspects: the dependence of acoustic energy on coupling materials; the dependence of thermal energy on coupling materials; the correlation between the acoustic energy and thermal energy in the crack. And all the experiment results are shown as bellowing:

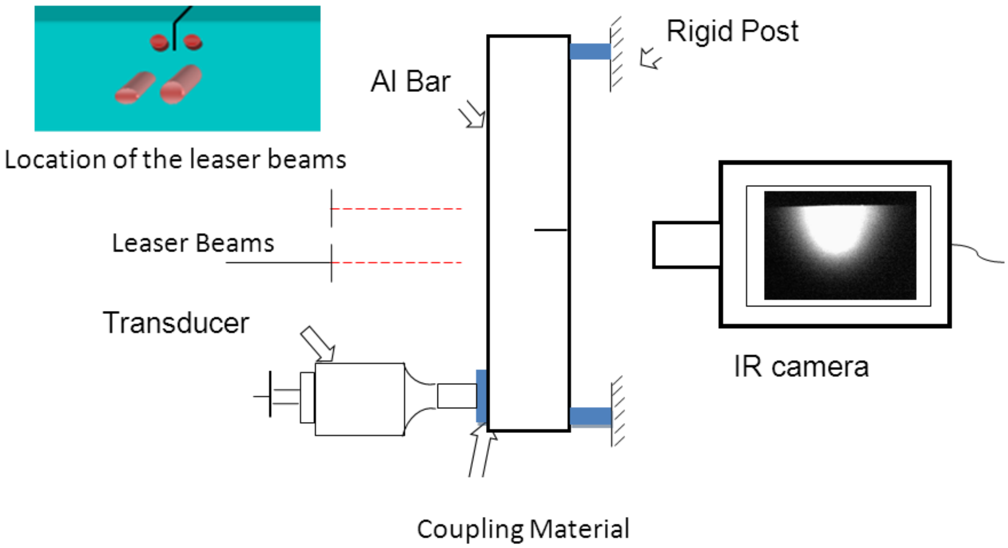

Fig.3.2 Overview of the experiment settings

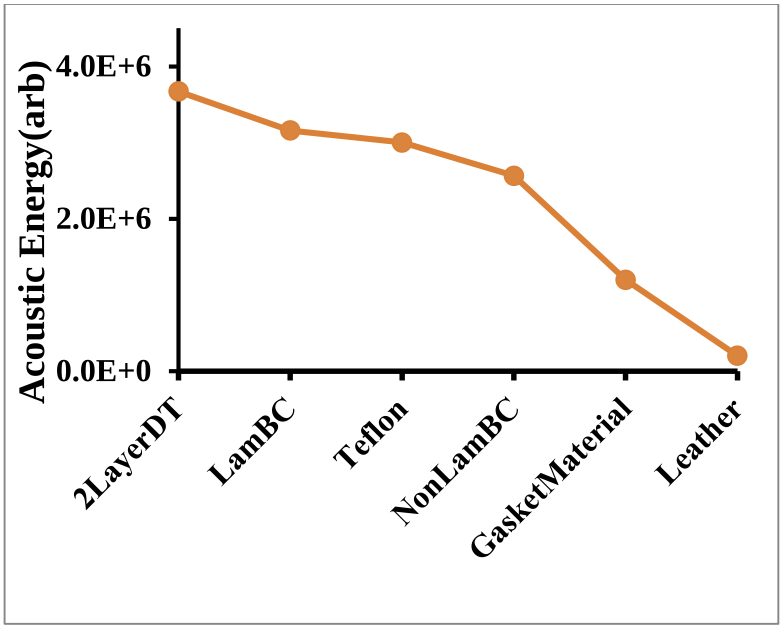

Fig.3.3 Acoustic Energy for different coupling materials for 20KHz system at 168N

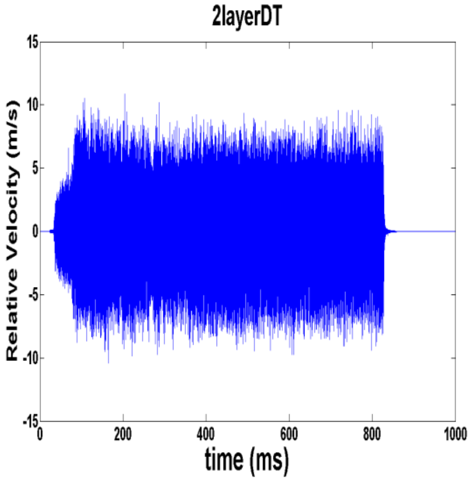

Waveform and its spectrum of 2layerDT

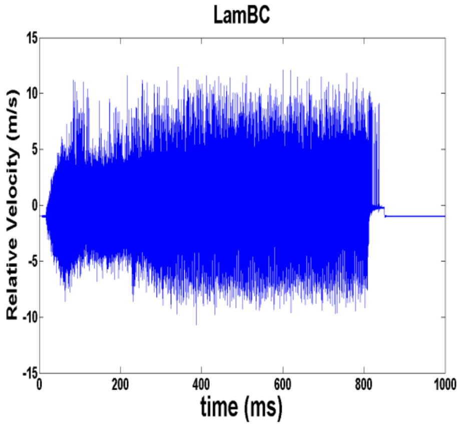

Waveform and its spectrum of LamBC

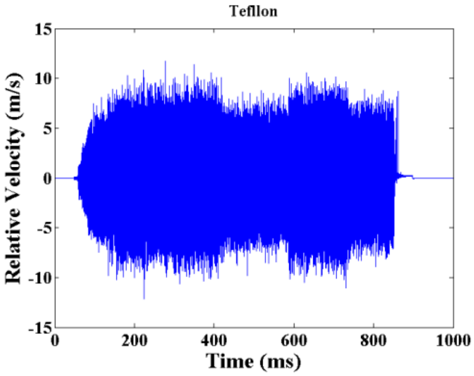

Waveform and its spectrum of Teflon

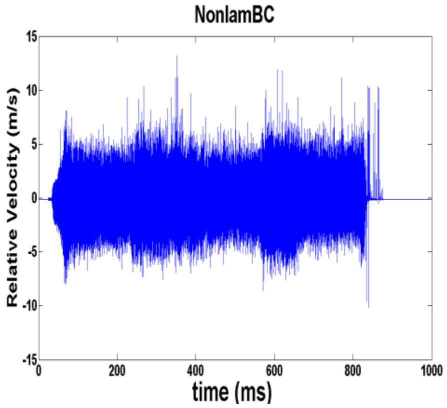

Waveform and its spectrum of NonLamBC

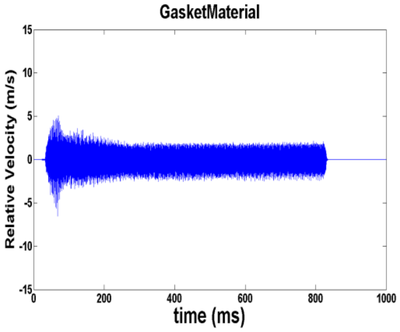

Waveform and its spectrum of GasketMaterial

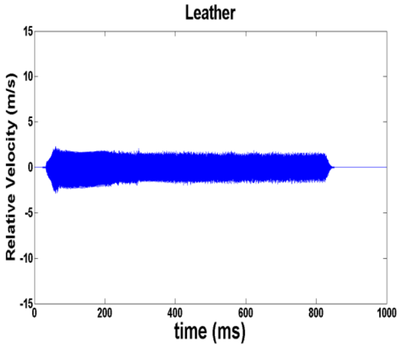

Waveform and its spectrum of Leather

Fig.3.4 6 groups of waveform and spectrum for these coupling materials

Fig.3.3 shows the results of acoustic energy calculated from expression (2) at one spot of the crack for six coupling materials using the 20 kHz ultrasound system. The ultrasound transducer is loaded with 168Newton. The acoustic energy at the crack is plotted in the order from the highest to the lowest in the order of 2LayerDT, LamBC, Teflon, NonLamBC, GasketMaterial and Leather correspondingly. When these coupling materials are used, the velocity waveforms of the relative motion of the crack faces measured with the laser vibrometer are plotted for the six coupling materials, as shown in Fig.3.4 respectively. The data acquisition sampling rate was set as 512 kHz for laser vibrometers. By comparing the waveforms, we can see that the amplitudes of the waveforms for a) 2layerDT, b) LamBC, c) Teflon, d) NonLamBC, e) GasketMaterial, and f) Leather follow the same trend as the acoustic energy plot for the six coupling materials in Figure 3.5

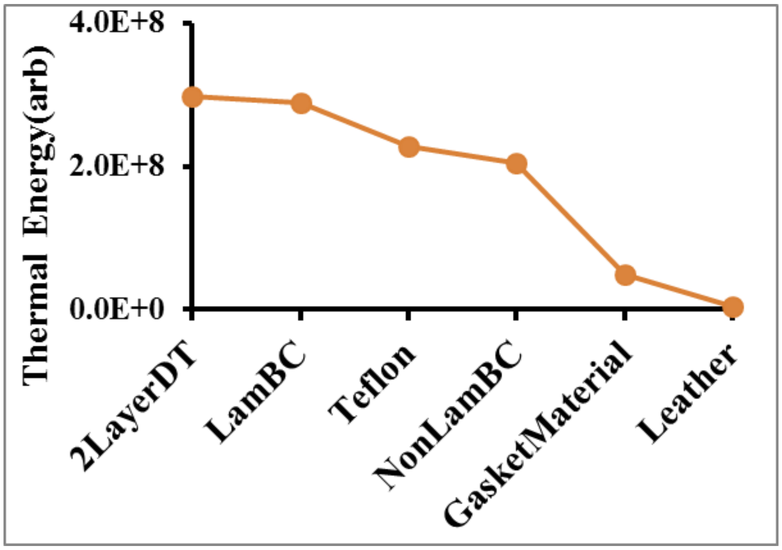

Fig.3.5 Thermal Energy for different coupling materials for 20K system at 168N

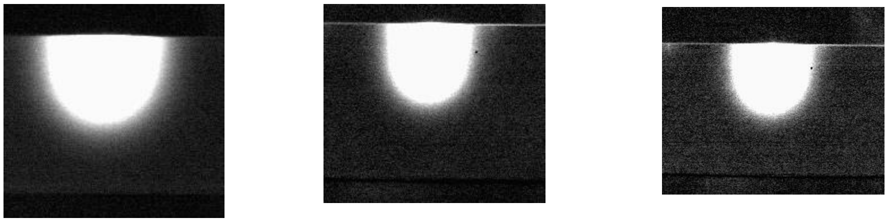

2layerDT LamBC Teflon

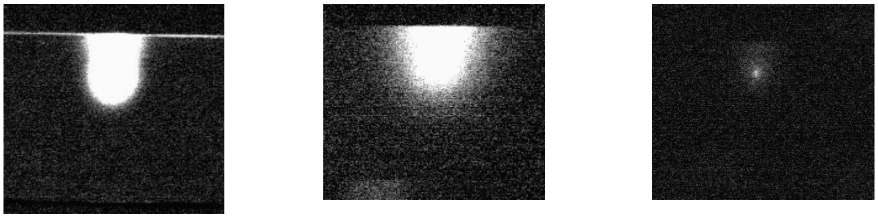

NonLamBC GasketMaterial Leather

Fig.3.6 Thermal Image for 6 coupling materials

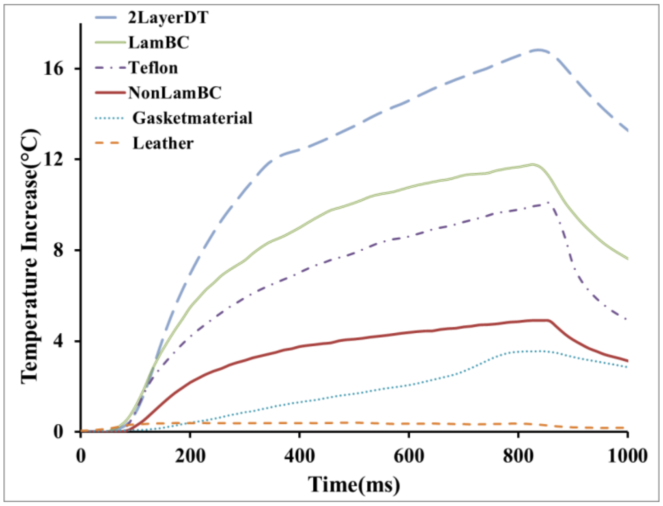

Fig.3.7 T-t plot of different coupling materials at 168N for 20kHz

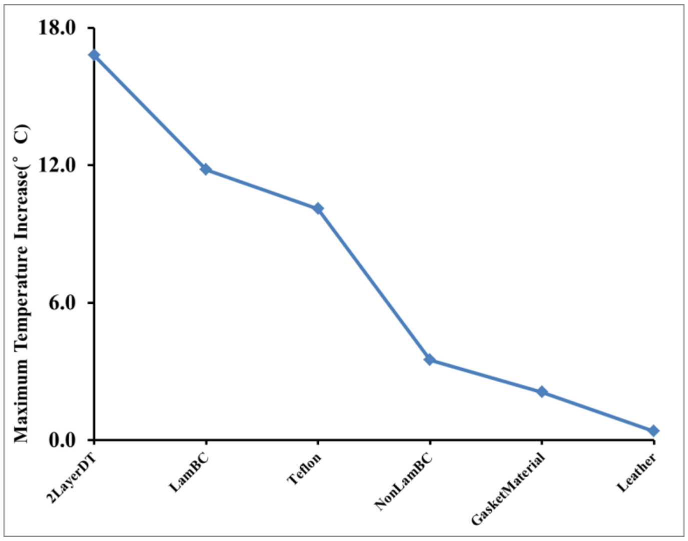

Fig. 3.8 Maxium temperature increase for different coupling materials

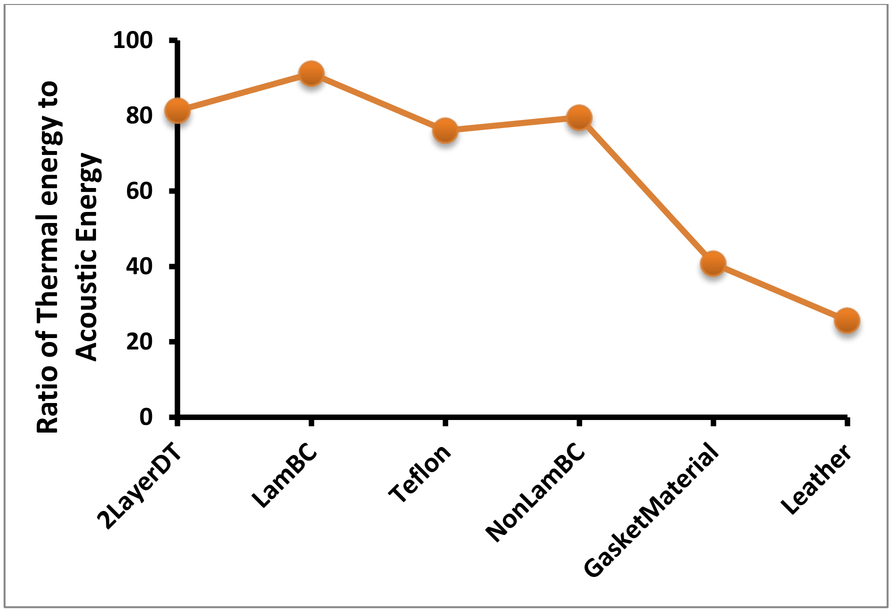

Fig. 3.9 Ratio of thermal energy to acoustic energy

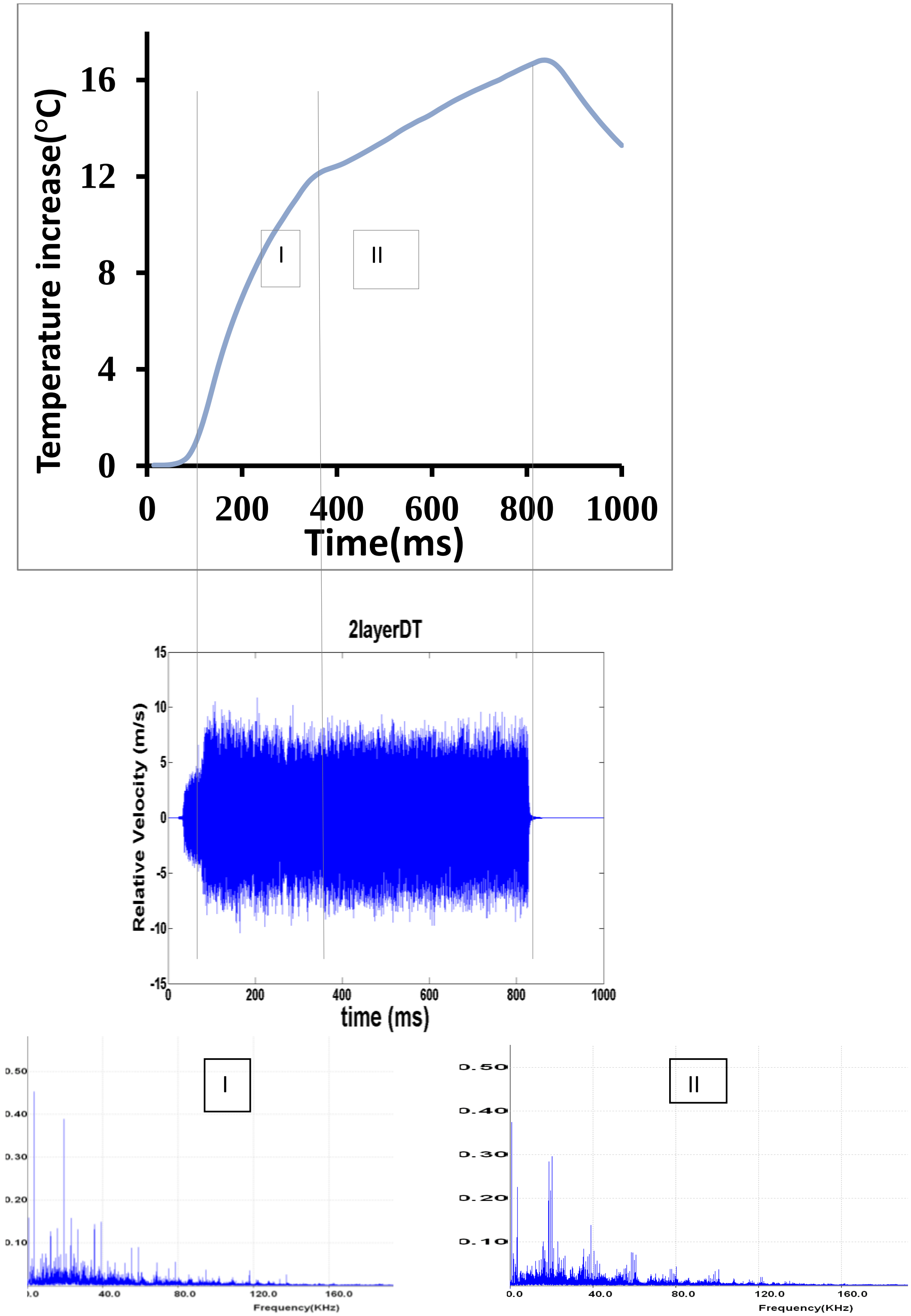

Fig. 3.10 Correlating crack vibration and crack heating via waveforms/spectra and temperature -time plot in the case of 2layerDT as a coupling material

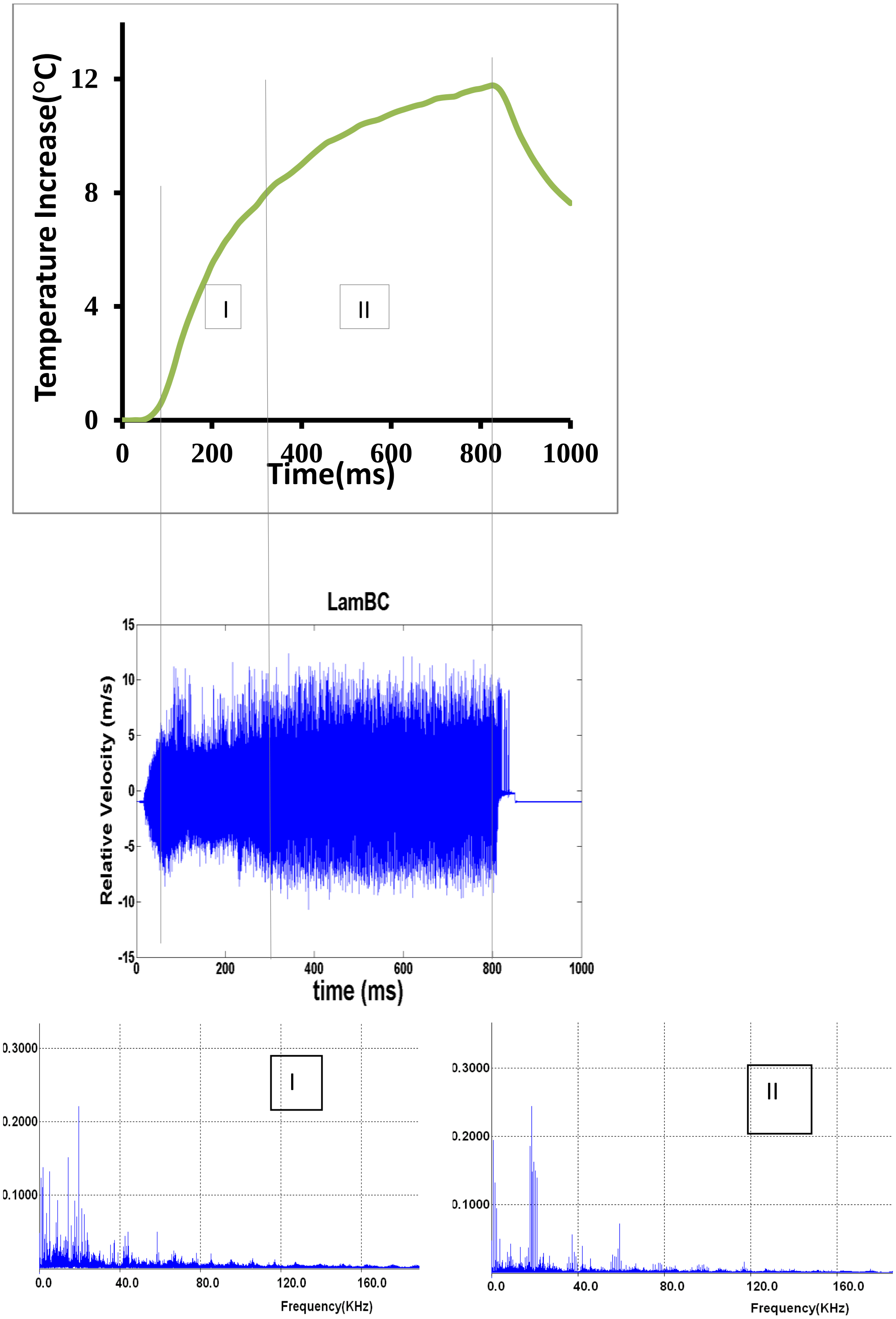

Fig.3.11 Correlating crack vibration and crack heating via waveforms/spectra and temperature -time plot in the case of LamBC as a coupling material

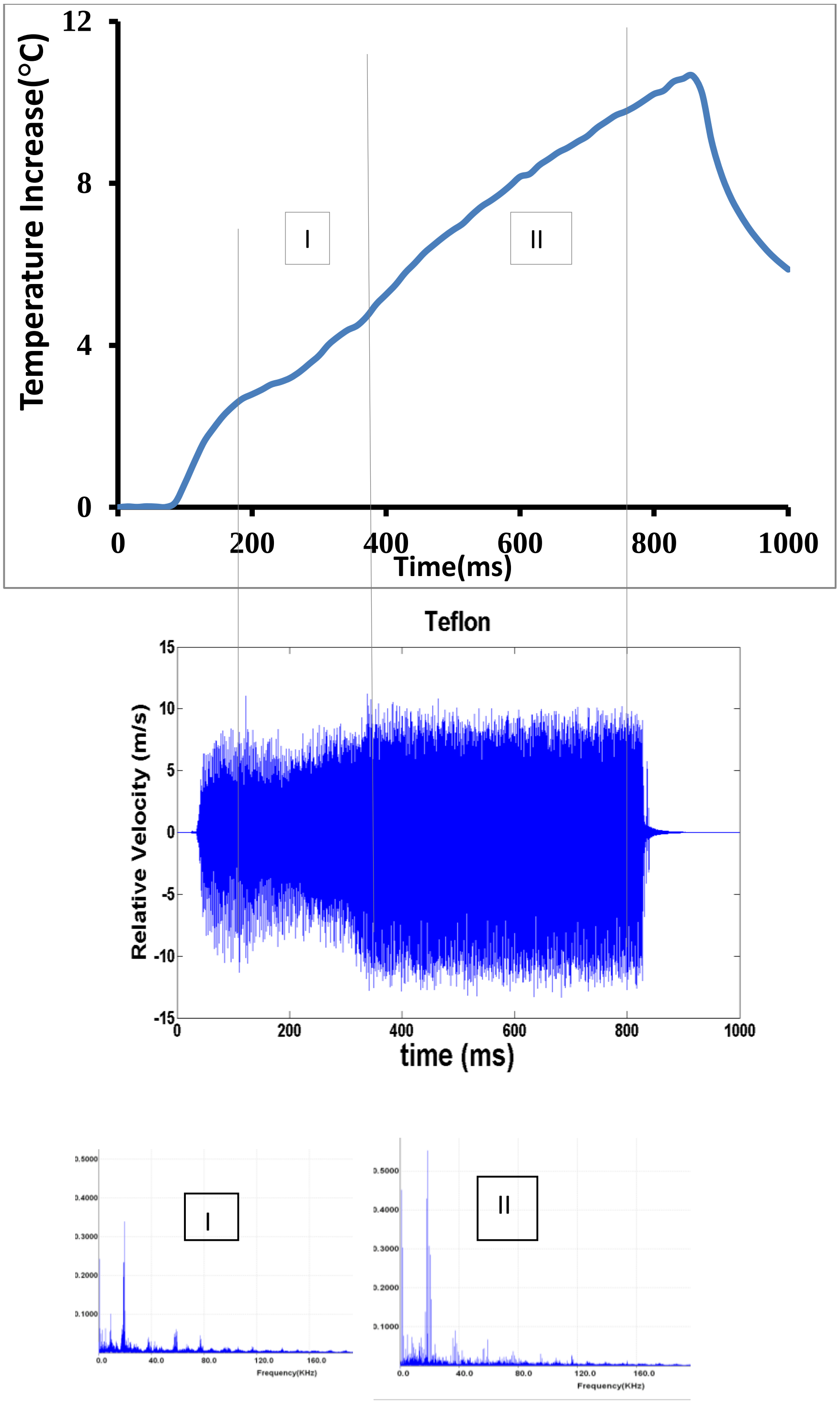

Fig. 3.12 Correlating crack vibration and crack heating via waveforms/spectra and temperature -time plot in the case of Teflon as a coupling material

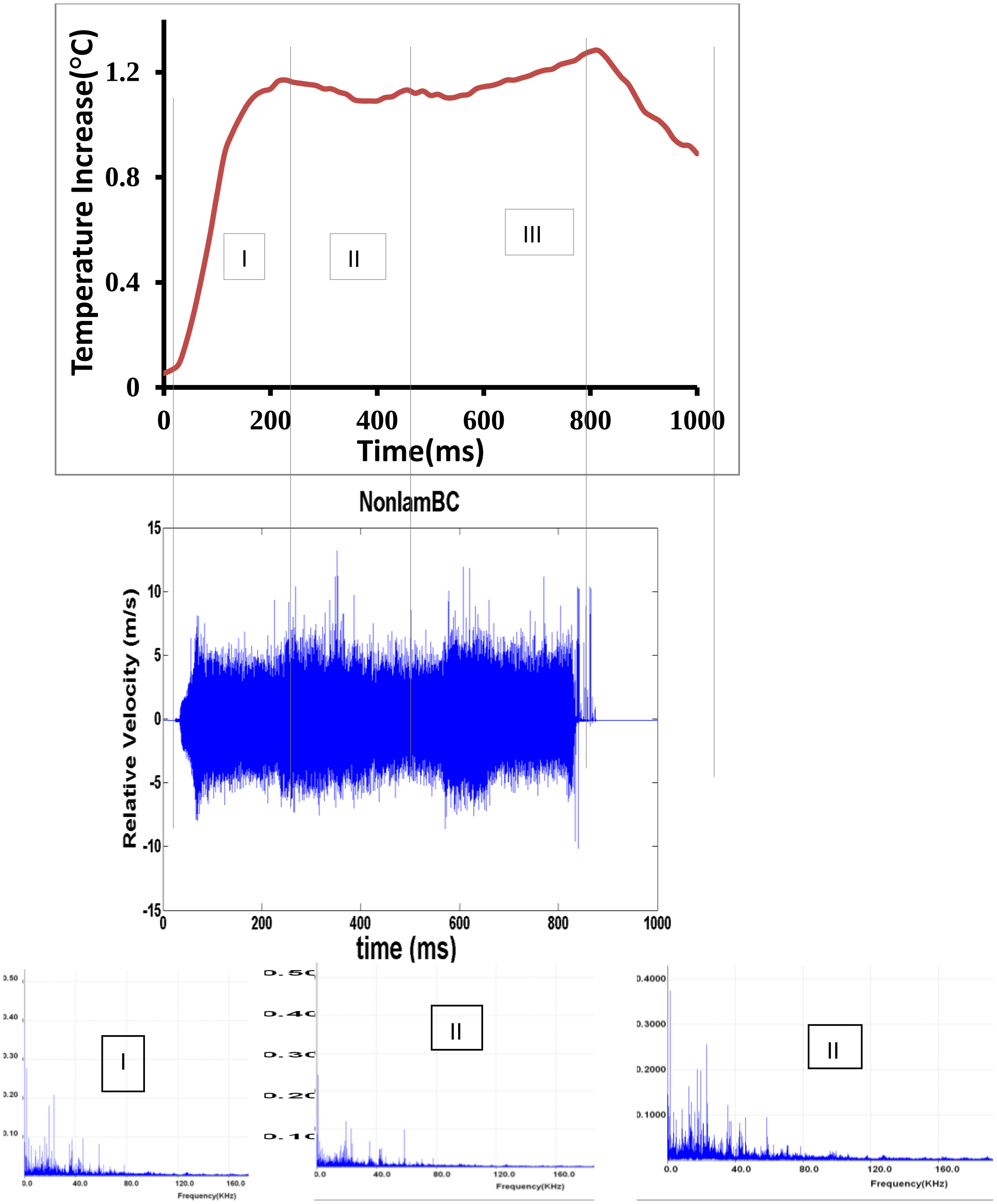

Fig.3.13 Correlating crack vibration and crack heating via waveforms/spectra and temperature -time plot in the case of nonlamBC as a coupling material

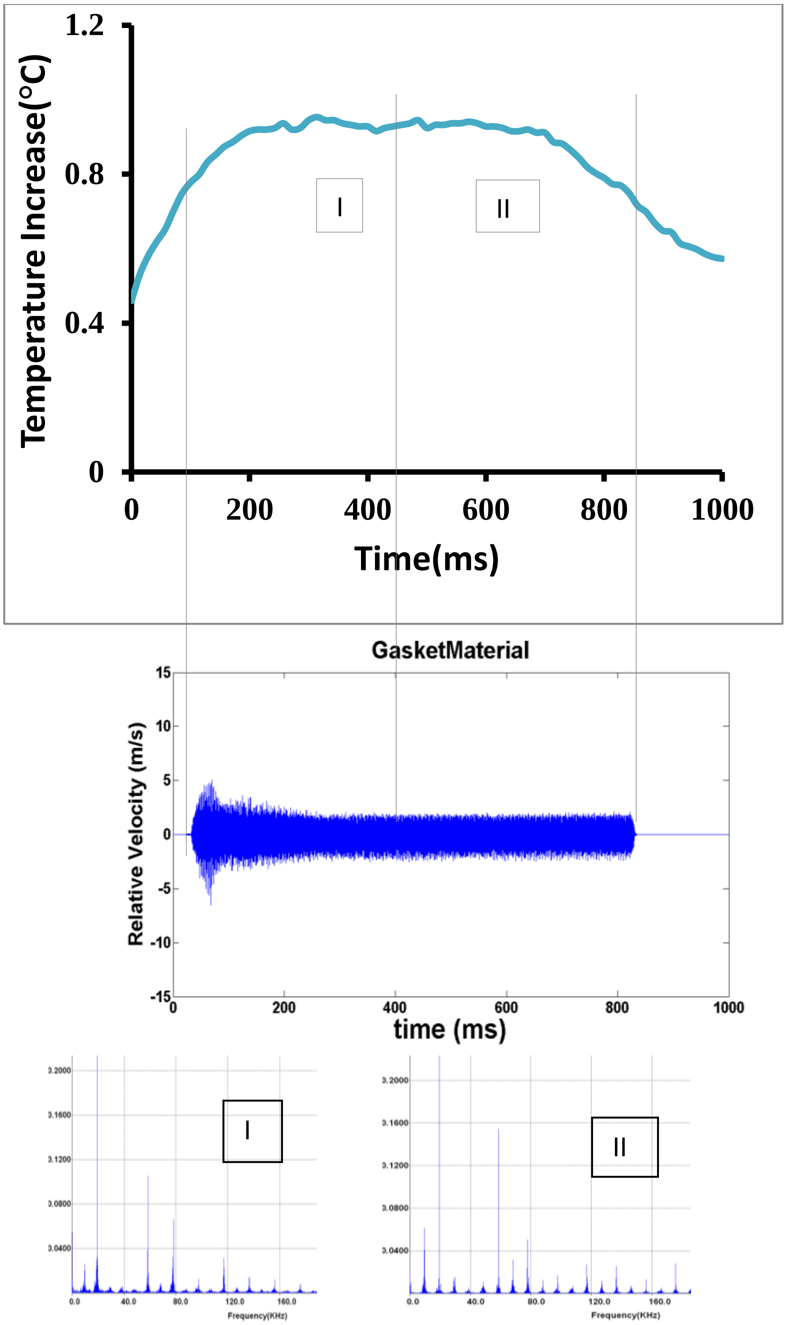

Fig.3.14 Correlating crack vibration and crack heating via waveforms/spectra and temperature -time plot in the case of GasketMaterail as a coupling material

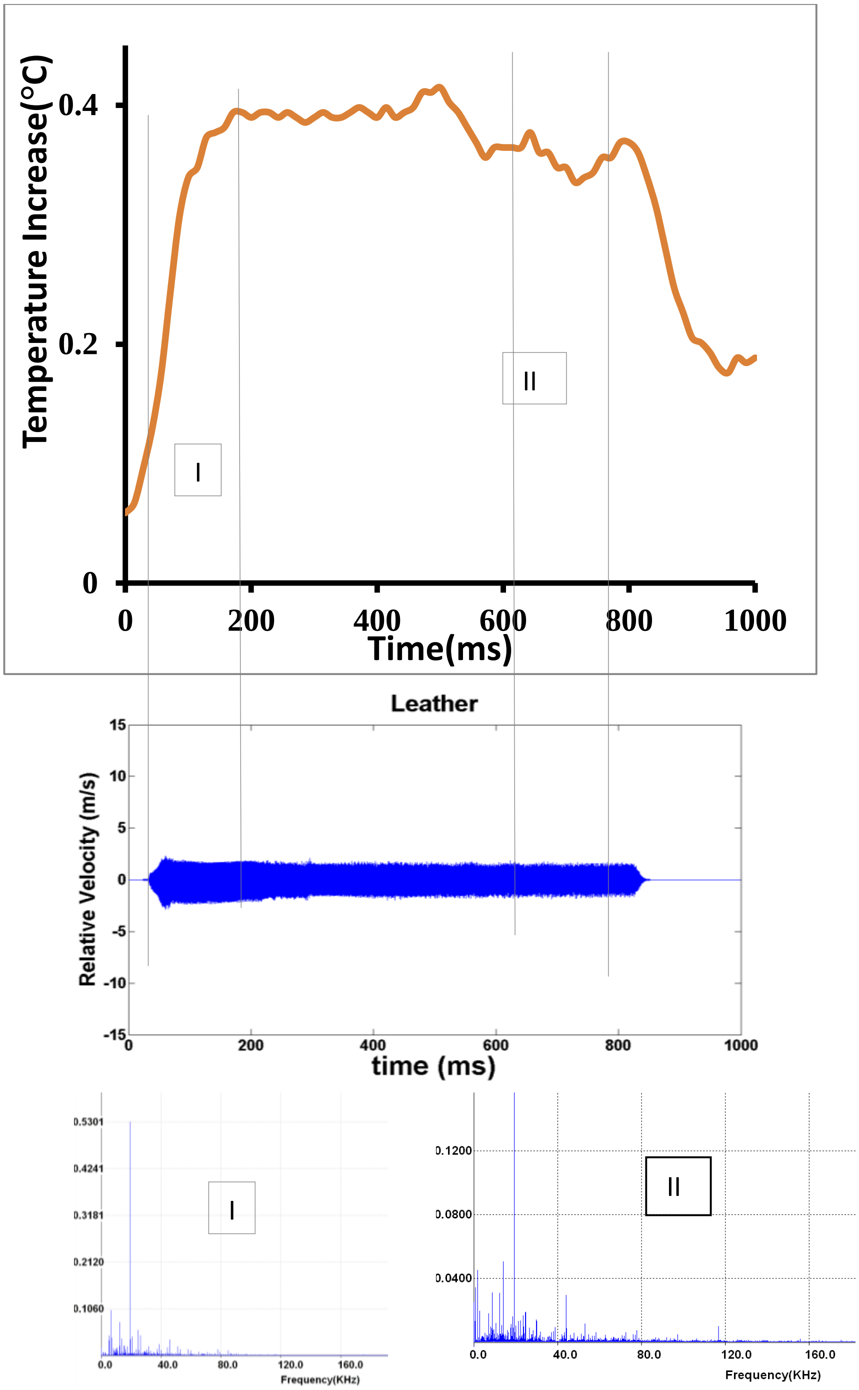

Fig.3.15 Correlating crack vibration and crack heating via waveforms/spectra and temperature -time plot in the case of Leather as a coupling material

Fig.3.5 shows the thermal energy levels calculated from crack heating using expression (1) at the same point of interest in all the images resulted from the six coupling materials respectively. It is shown that the thermal energy levels have the order from the highest to the lowest for the six coupling materials as: 2LayerDT, LamBC, Teflon, NonLamBC, GasketMaterial, and Leather. In Fig.3.6, we present the IR images taken at times when the temperature of the crack reaches its highest value for these six corresponding coupling materials. The same contrast was applied to all these images for visual comparison. The corresponding temperature-time (T-t) plots at the crack are shown in Fig.3.7. In Fig.3.8, the maximum temperature increase at the crack shows the same trend as the thermal energy levels calculated for these six coupling materials.

Fig.3.9 shows the ratio of thermal energy to acoustic energy for these coupling materials calculated from expression (3). We can see that a higher thermal to acoustic energy ratio is representative of a more efficient coupling material. From this calculation, it turns out that LamBC has a bit higher efficiency than 2LayerDT, and NonLamBC has slightly higher efficiency than Teflon. But the overall trend is about the same as in Figure 3.6 and Figure3.7. Figs.3.10-3.15 shows the alignment of timelines of T-t plots and their corresponding detailed waveforms and spectra for these six coupling materials. One observation is that the T-t plots have different slopes for different periods during the excitation pulse. In the case of 2LayerDT as coupling material, the slope of T-t curve in phase I is higher than that in phase II. The waveform is also divided into the same time periods as phase I and phase II. The spectra for both phases were calculated as shown in the figure. The phase II spectrum shows a few dominated frequencies around which groups of frequencies are formed. However, the phase I spectrum is more or less distributed. The same approach was carried out for LamBC & Teflon, and others. The trend for their spectra of the two phases are the same as for 2LayerDT.

3.2.2 Effect of loading force

In this section, we focus on the effect of loading force on SonicIR system, here we use one coupling material only, and also only one frequency system(20KHz), the settings are similar as section one as shown in Fig.3.16. The difference is that we use different loading force on the coupling material, rather than one force from previous section. The experimental data are shown in below, and they are also interpreted in these aspects: the dependence of acoustic energy on coupling materials; the dependence of thermal energy on coupling materials; the correlation between the acoustic energy and thermal energy in the crack.

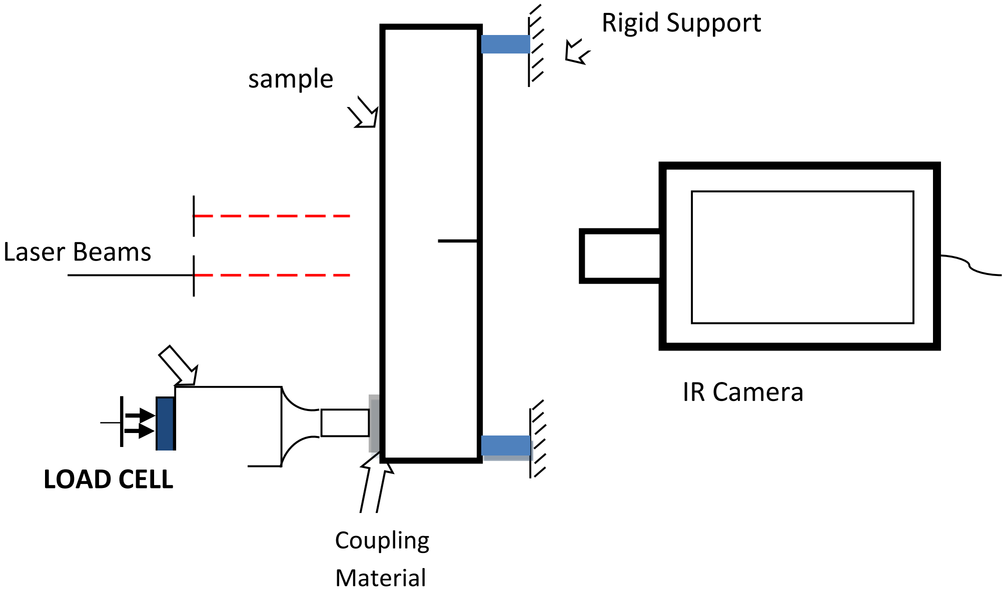

Fig.3.16 Experimental setting in this part

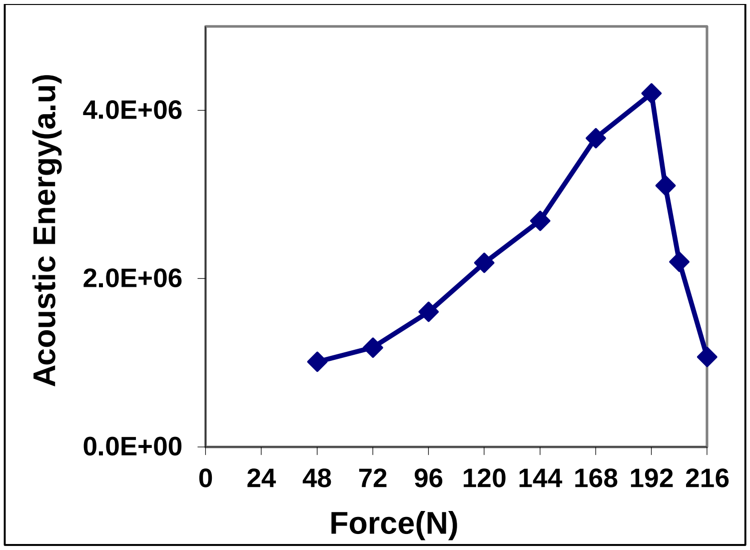

Fig.3.17 Acoustic energy calculated at one spot of the crack for 2layerDT as coupling material with 20kHz system at different loading force

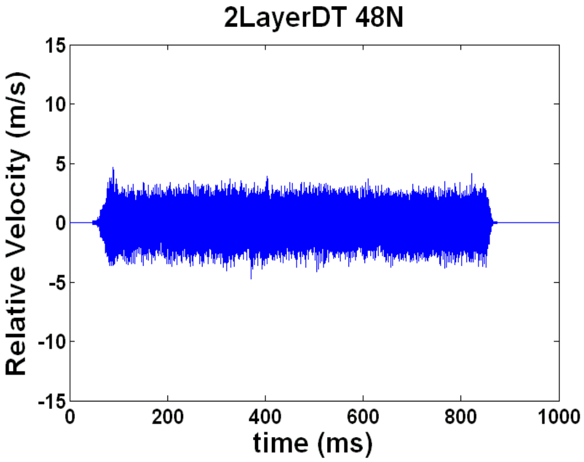

Fig.3.18a Relative vibration waveform with 2layerDT as a coupling material at loading force 48N

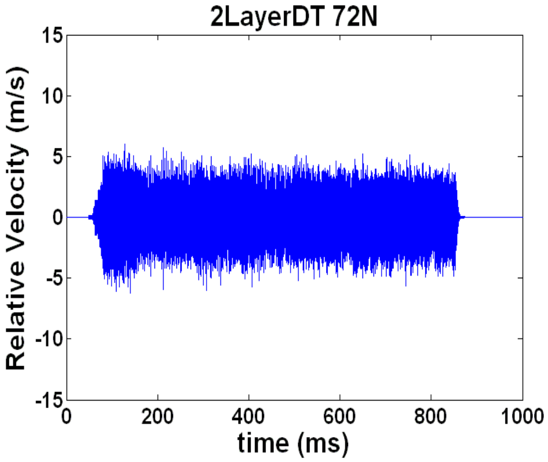

Fig. 3.18b Relative vibration waveform with 2layerDT as a coupling material at loading force 72N

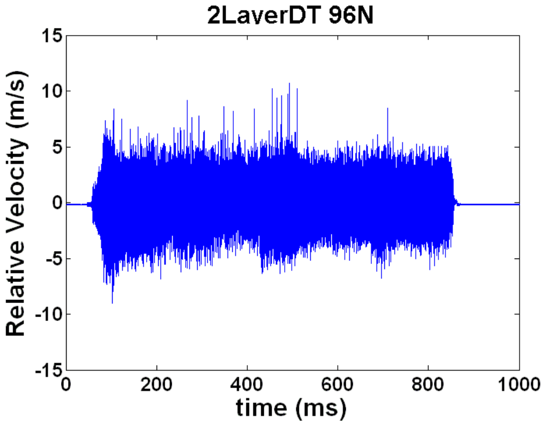

Fig. 3.18c Relative vibration waveform with 2layerDT as a coupling material at loading force 96N

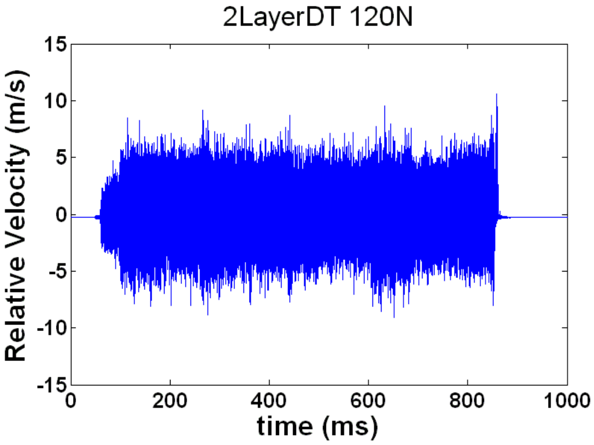

Fig. 3.18d Relative vibration waveform with 2layerDT as a coupling material at loading force 120N

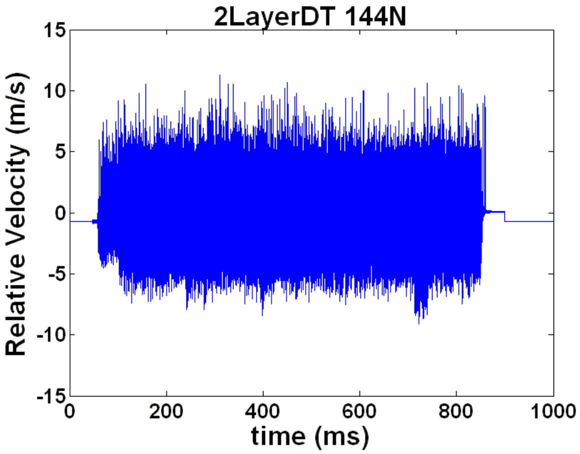

Fig. 3.18e Relative vibration waveform with 2layerDT as a coupling material at loading force 144N

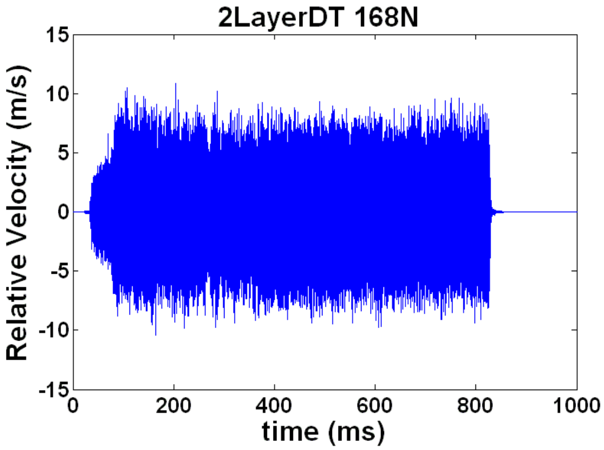

Fig. 3.18f Relative vibration waveform with 2layerDT as a coupling material at loading force 168N

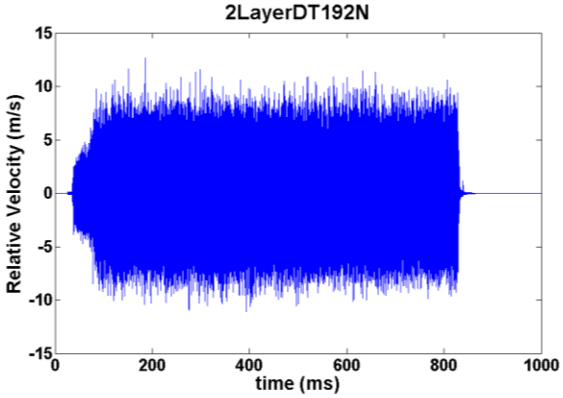

Fig.3.18g Relative vibration waveform with 2LayerDT as a coupling material at loading force 192N

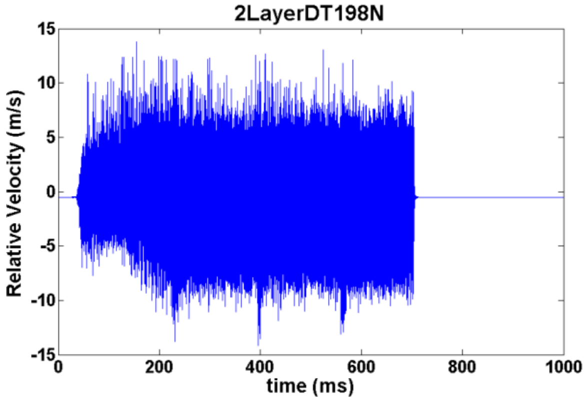

Fig.3.18h Relative vibration waveform with 2LayerDT as a coupling material at loading force 198N

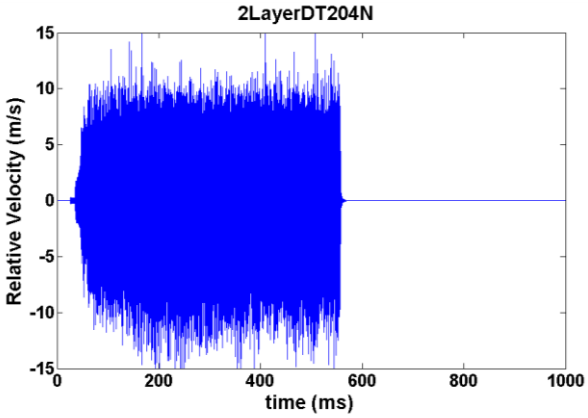

Fig.3.18i Relative vibration waveform with 2LayerDT as a coupling material at loading force 204N

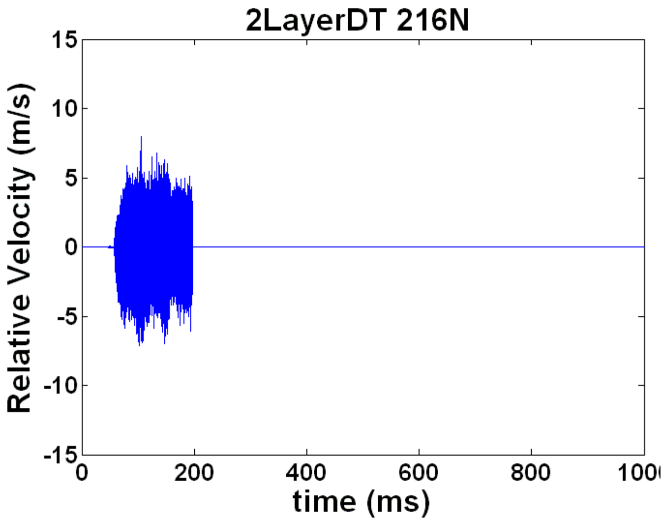

Fig. 3.18j Relative vibration waveform with 2layerDT as a coupling material at loading force 216N

Fig. 3.18 Relative vibration waveform with 2layerDT as a coupling material at different loading force

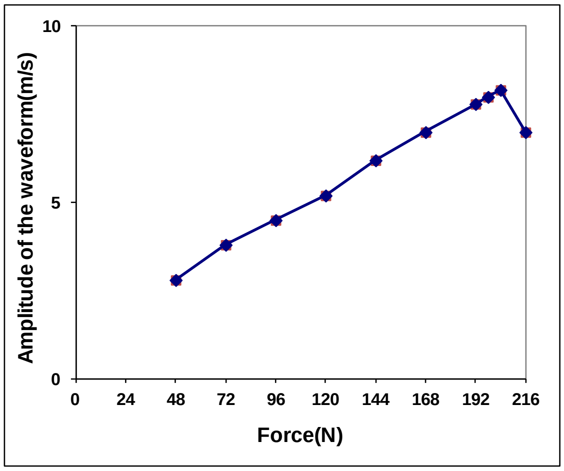

Fig.3.19 Relationship between the amplitude of the waveforms and the loading force

Fig.3.17 shows the result of acoustic energy at one spot of the crack with 2LayerDT as coupling material at loading forces of 48N, 72N, 96N, 120N, 144N, 168N, 192N, 198N, 204N and 216N. From this figure, we can see that the acoustic energy from the crack increase as the loading force increase, except when it is overloaded which happens at 198N.

From Fig.3.18 and Fig.3.19, the amplitude of the vibration waveform has the same trend as the acoustic energy from lowest to the highest, except the overloading when pushing transducer harder to the coupling material. From the data, one can see that when the loading force increases, the relative motion between the cracks faces increases as well before overloading occurs. In these situations, the ultrasound pulse length was not full length of 800ms. Therefore, with the much shortened ultrasound pulse, the acoustic energy calculated at the crack spot, plotted in Figure 3.17, has a sharp drop from 192N to 198N

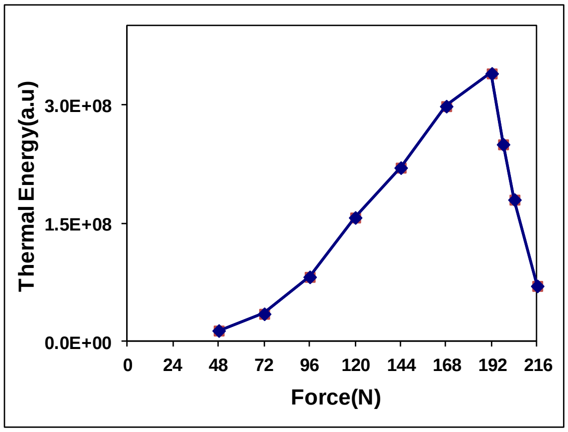

Fig.3.20 Thermal Energy calculated at one spot of the crack for 2LayerDT as coupling material with 20 kHz system at different loading forces

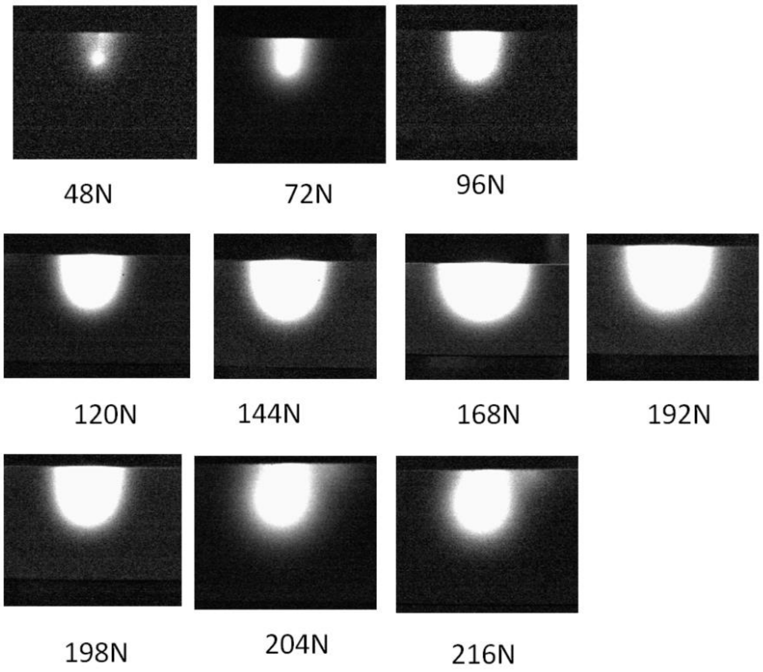

48N 72N 96N

120N 144N 168N 192N

198N 204N 216N

Fig.3.21IR Images of the crack taken with the different loading force for 2layerDT as coupling material respectively

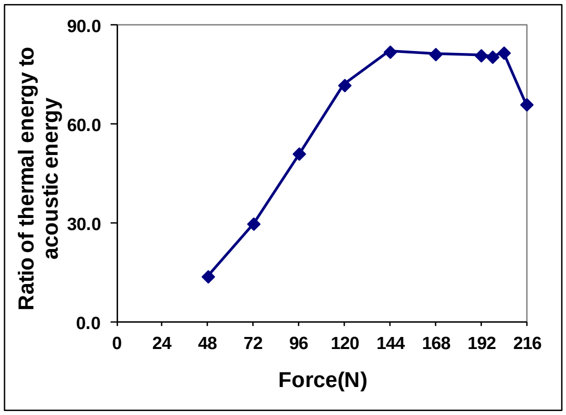

Fig. 3.22 Ratio of thermal energy to acoustic energy on different loading forces

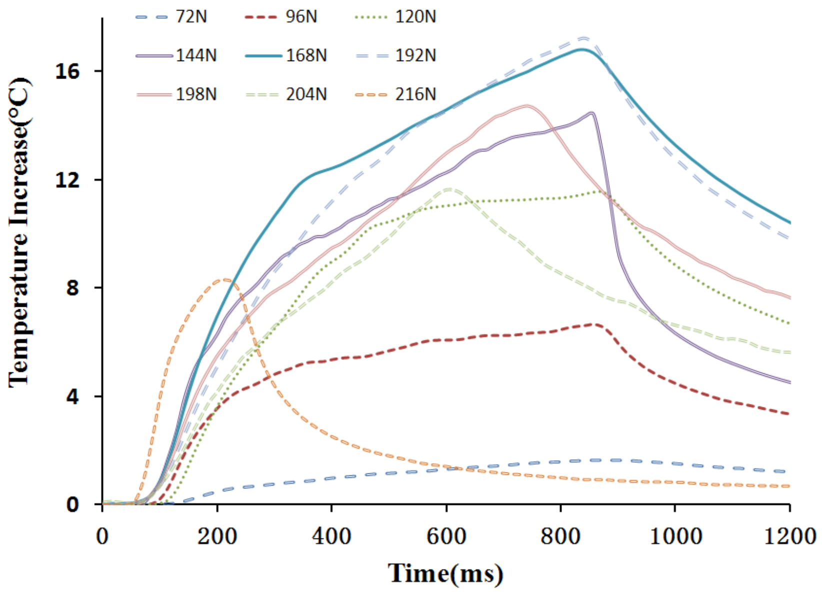

Fig.3.23 Temperature - time plots of the crack with the six coupling materials at 168N for the 20kHz system

Fig.3.20 shows the calculated thermal energy using the pixel values of IR images at different loading forces. It is clear that this curve has the same trend as the acoustic energy curve in Fig.3.17. The thermal energy increases when the loading force increases, until when overloading happens at 198N. Fig.3.20 shows the corresponding IR images taken at times when the temperature of the crack reaches its highest point for each of these loading forces. All of these images were applied with the same contrast for display and visual comparison. When the loading force is 198N, overloading happens to the system, where the pulse input to the sample is not full length of the pulse setting as it is shown in vibration in Fig.3.18h. Correspondingly, this short period of vibration only generate a small amount of the heat on the crack area comparing to the full length of vibration process. Therefore, its IR signal level is lower compare to the other situations. Fig.3.23 shows the temperature-time (T-t) plots at the crack with different loading forces. The temperature increases at different rate for these loading forces which also show the same trend as the acoustic energy. Ratio of thermal energy to acoustic energy is shown in Fig.22. The ratio curve is not flat which means the thermal energy is not proportional to the acoustic energy. In other words, the thermal energy does not increase with the same rate as the acoustic energy when loading force increases.

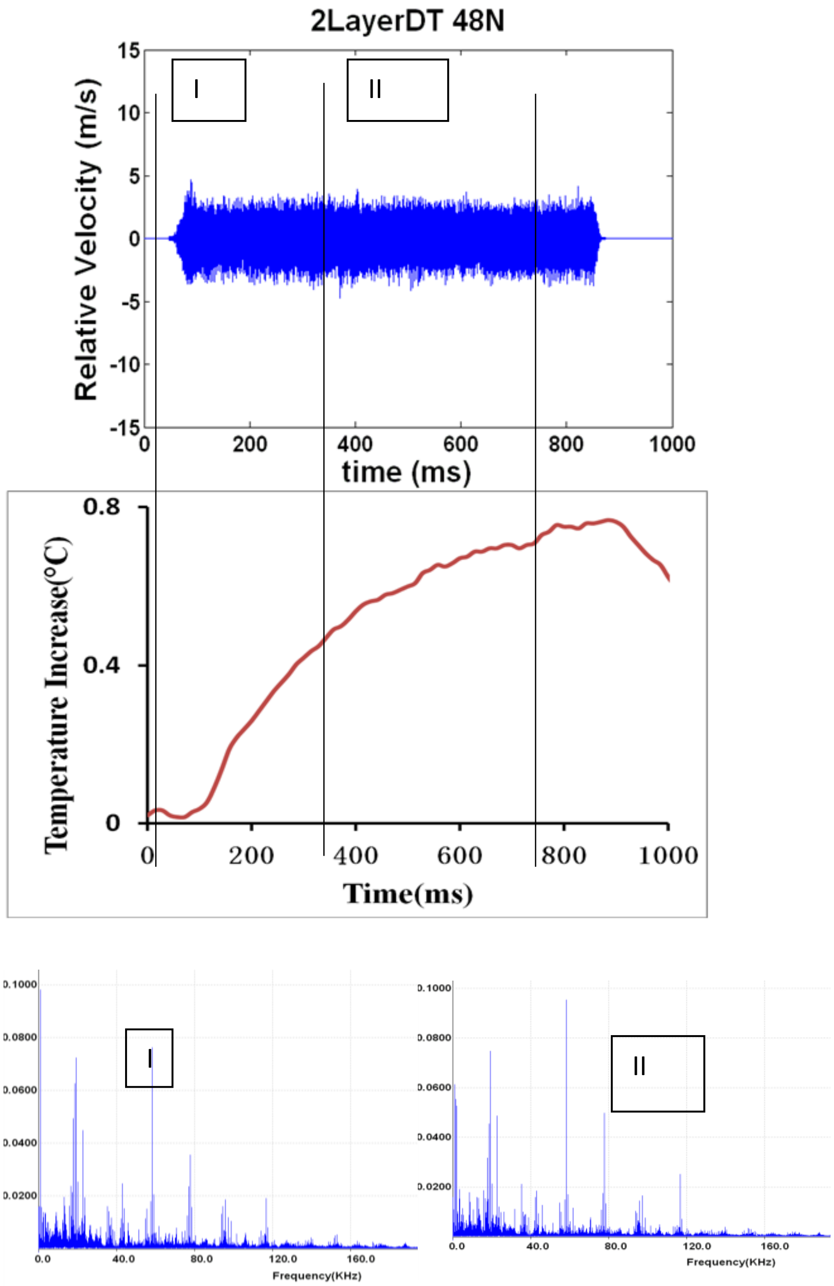

Fig.3.24 Correlating crack vibration and crack heating via waveforms/spectra and temperature -time plot in the case of 2layerDT as a coupling material at 48N

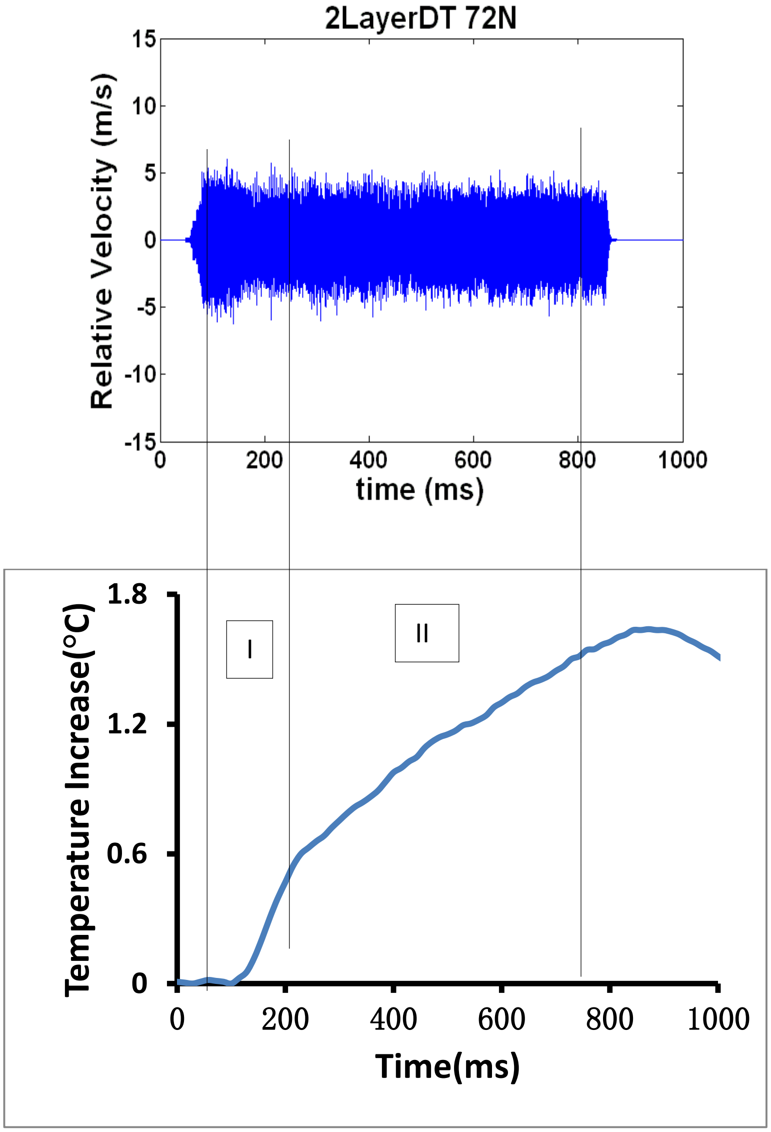

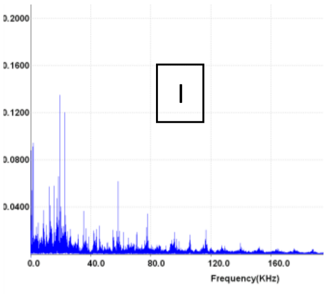

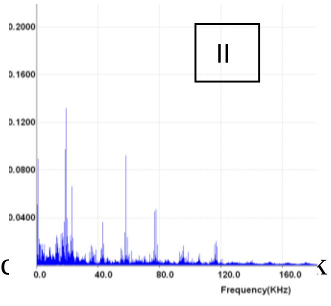

crac k heating via waveforms/spectra and temperature -time plot in the case of 2layerDT as a coupling material at 72N

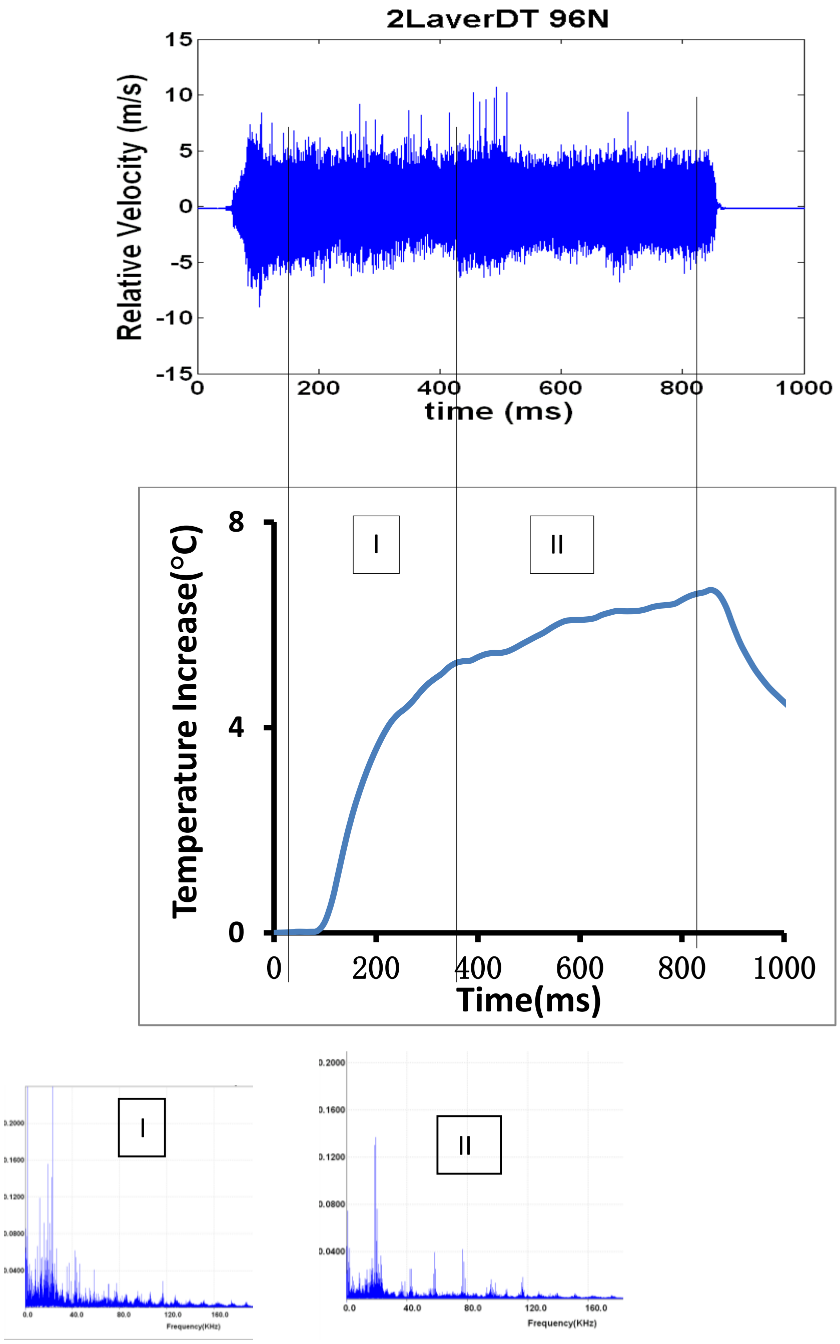

Fig.3.26 Correlating crack vibration and crack heating via waveforms/spectra and temperature -time plot in the case of 2layerDT as a coupling material at 96N

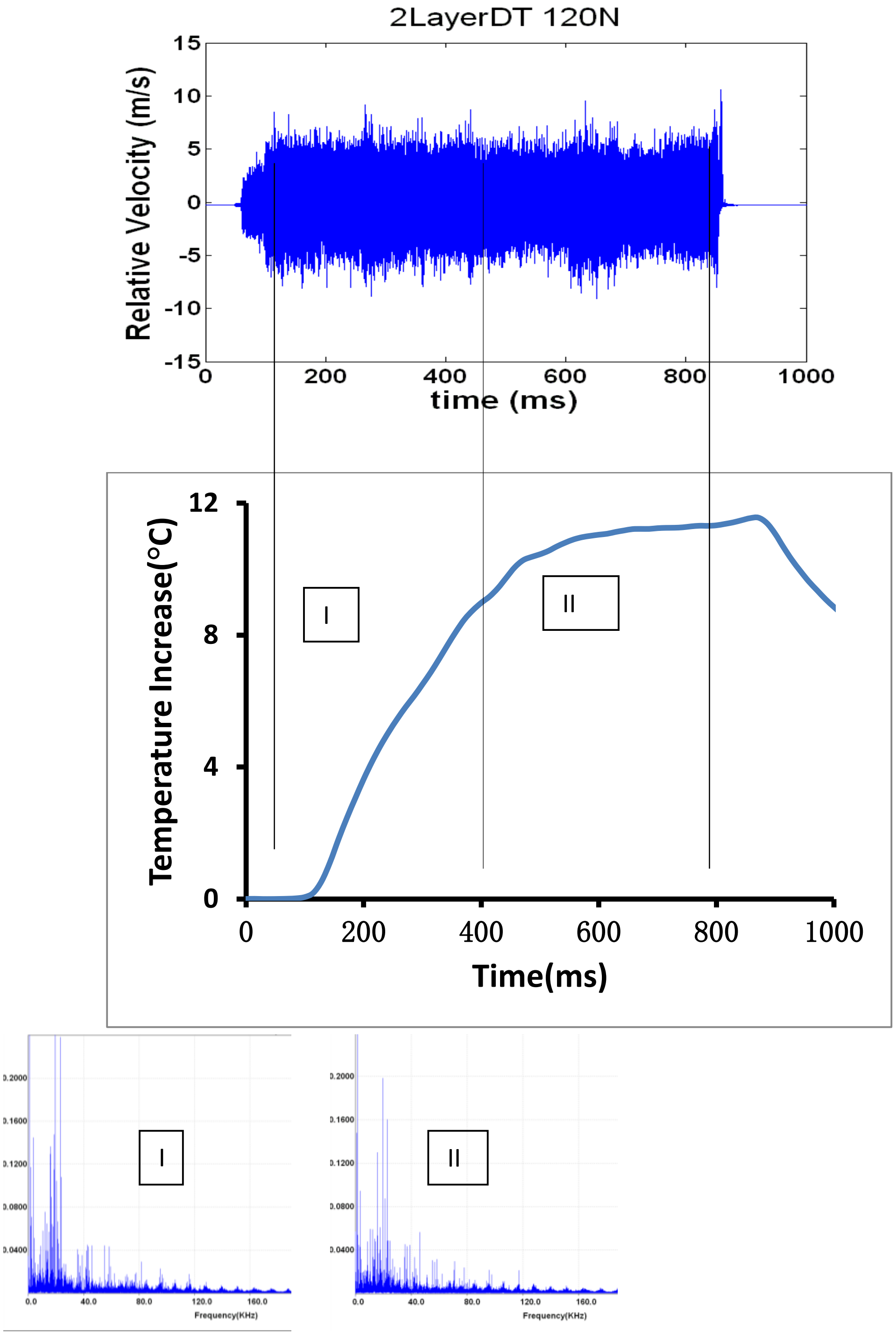

Fig.3.27 Correlating crack vibration and crack heating via waveforms/spectra and temperature -time plot in the case of 2layerDT as a coupling material at 120N

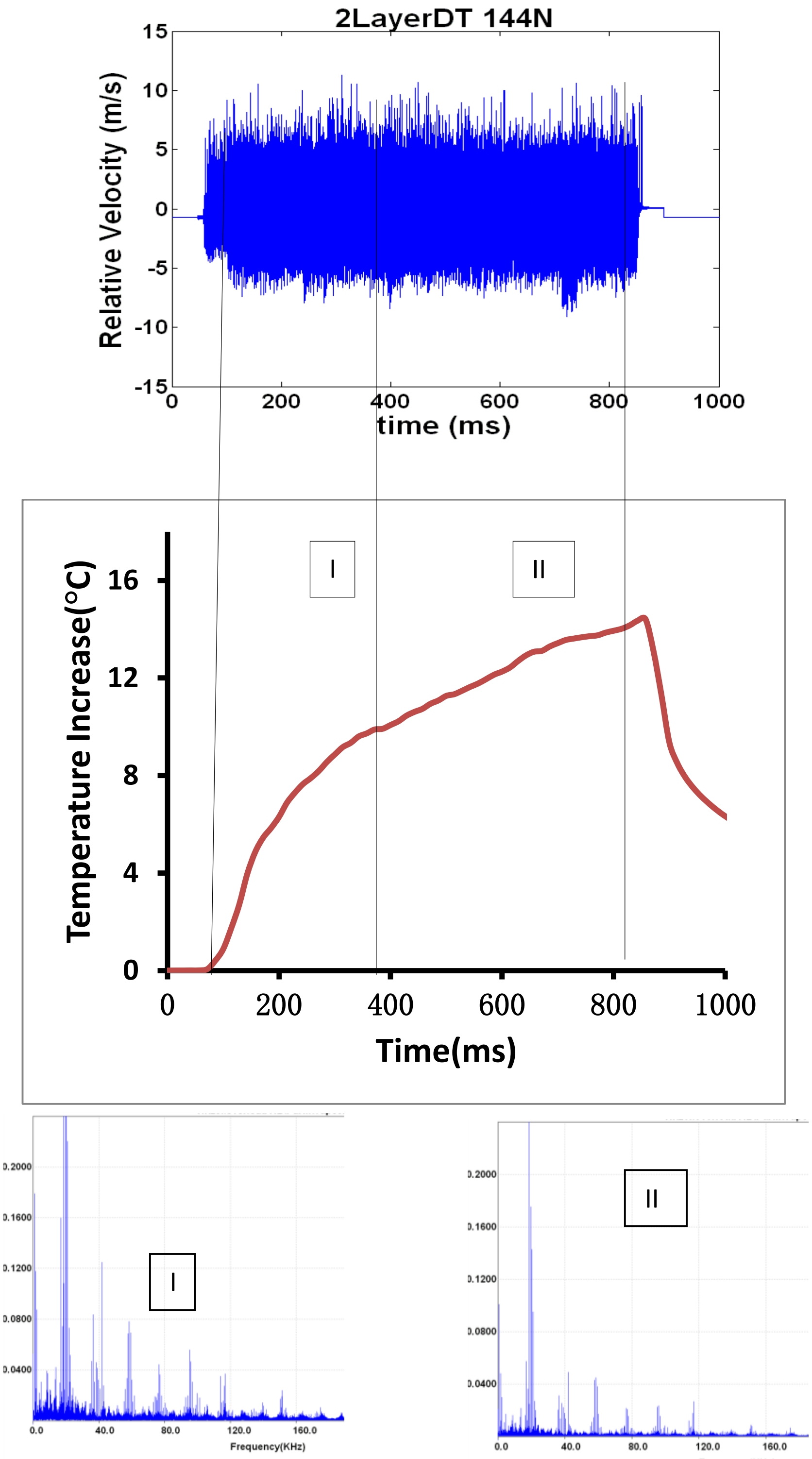

Fig.3.28 Correlating crack vibration and crack heating via waveforms/spectra and temperature -time plot in the case of 2layerDT as a coupling material at 144N

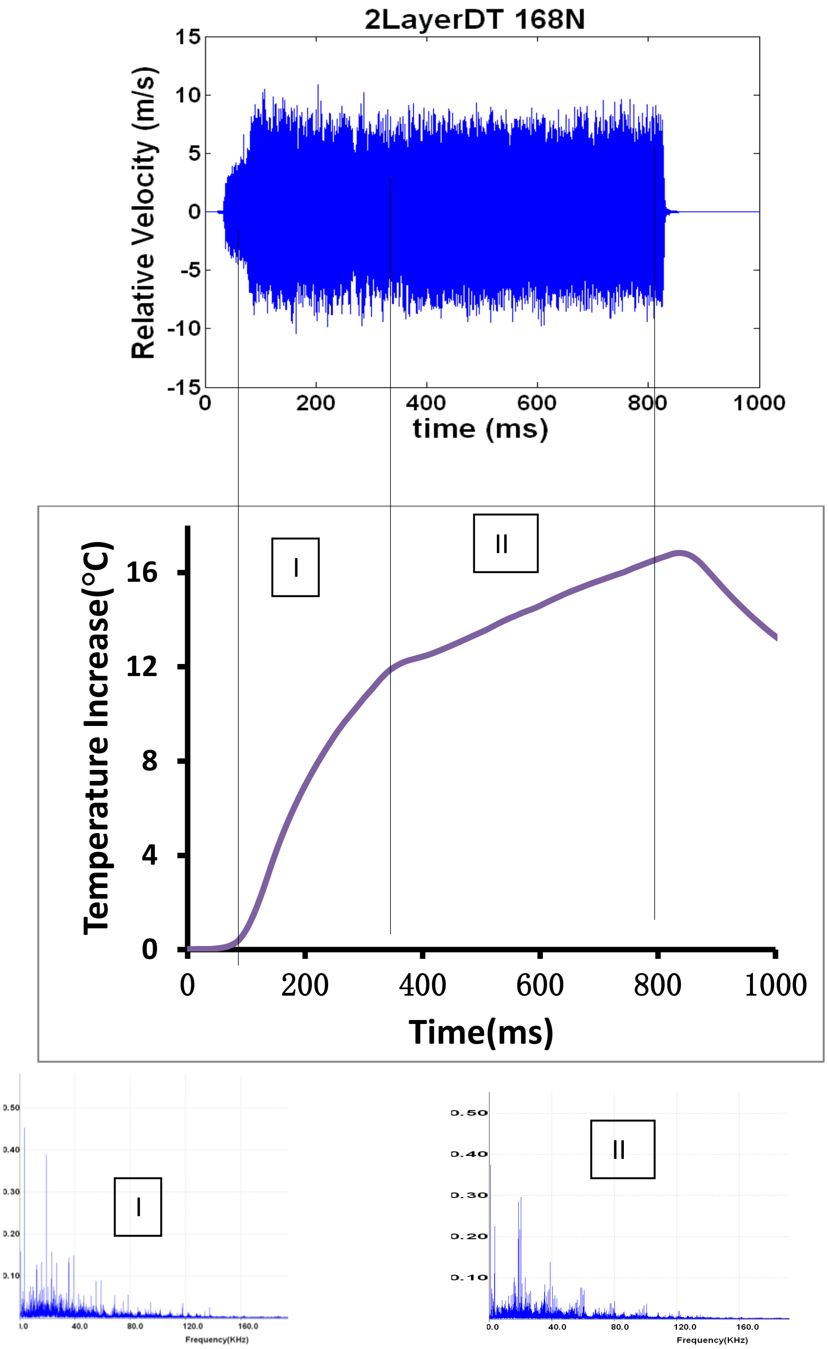

Fig.3.29 Correlating crack vibration and crack heating via waveforms/spectra and temperature -time plot in the case of 2layerDT as a coupling material at 168N

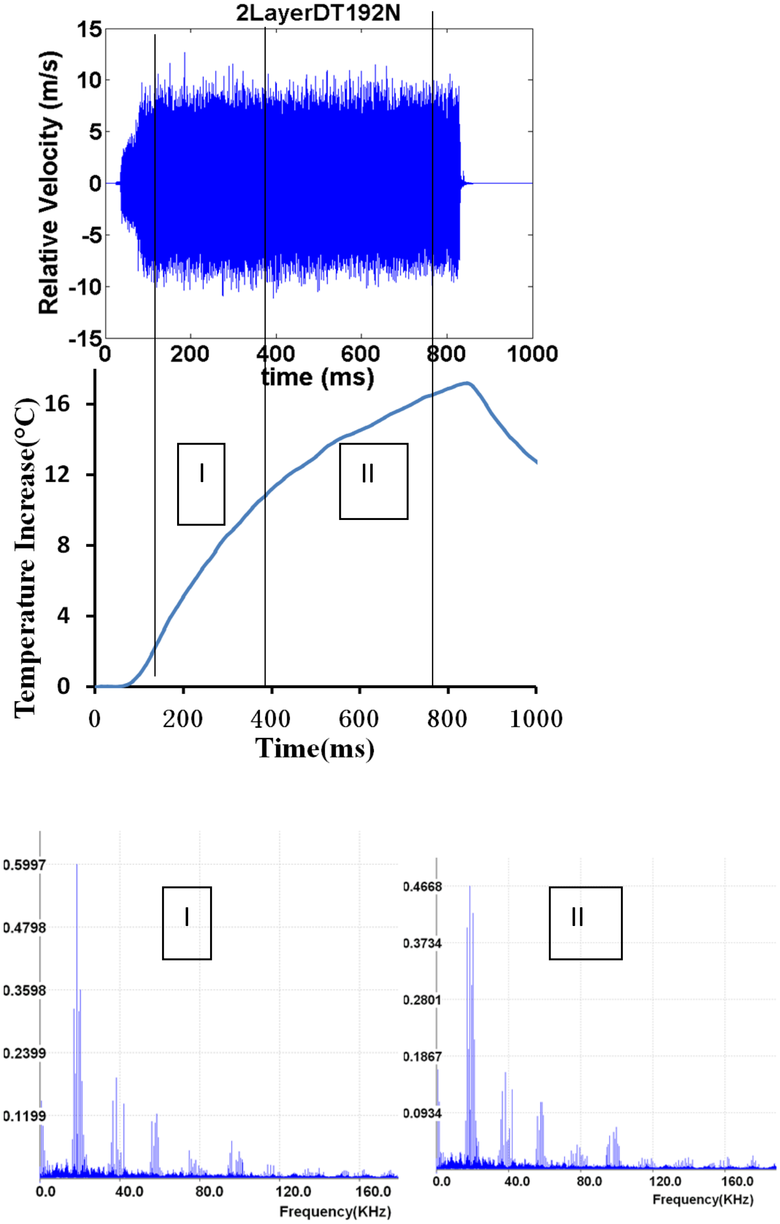

Fig.3.30 Correlating crack vibration and crack heating via waveforms/spectra and temperature -time plot in the case of 2LayerDT as a coupling material at 192N

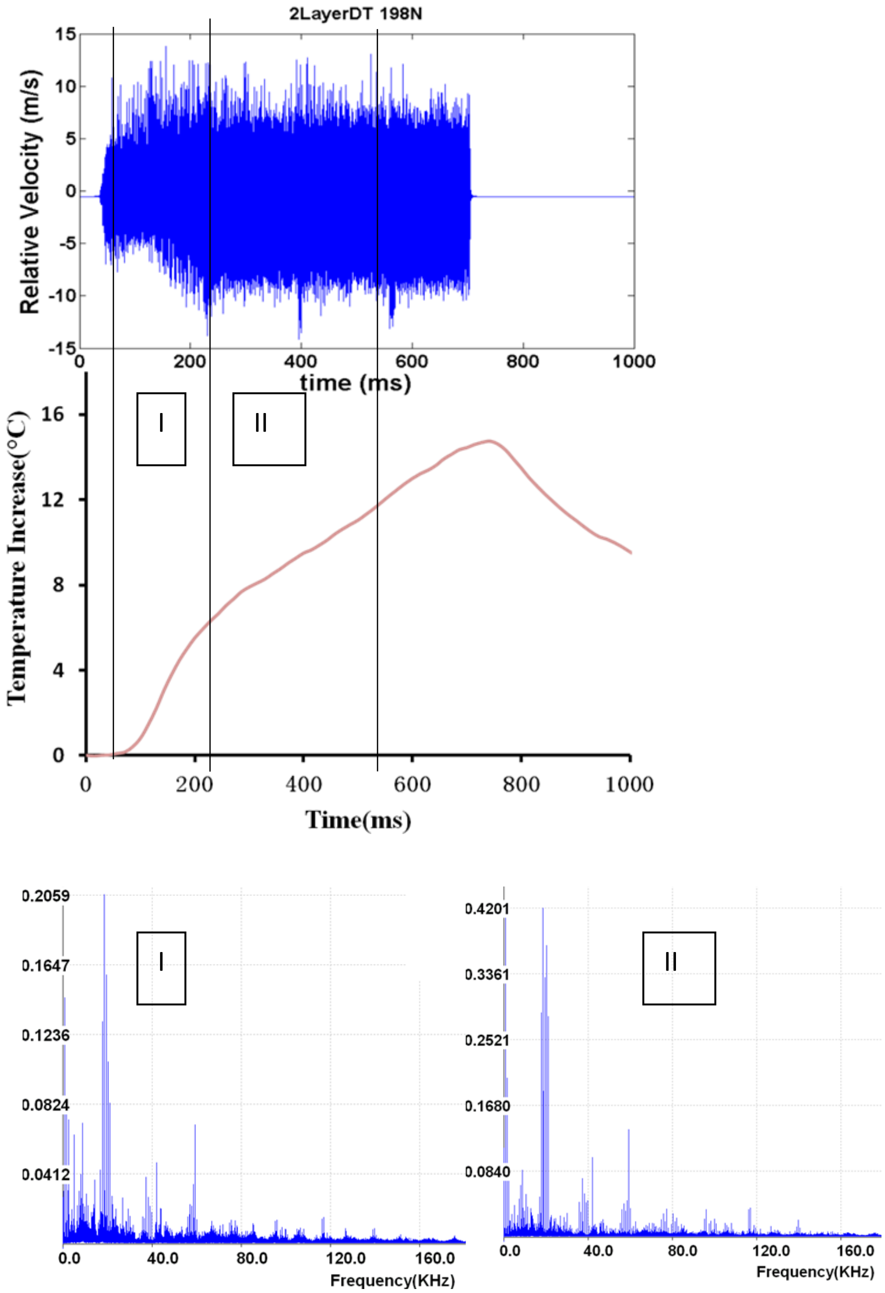

Fig.3.31 Correlating crack vibration and crack heating via waveforms/spectra and temperature -time plot in the case of 2LayerDT as a coupling material at 198N

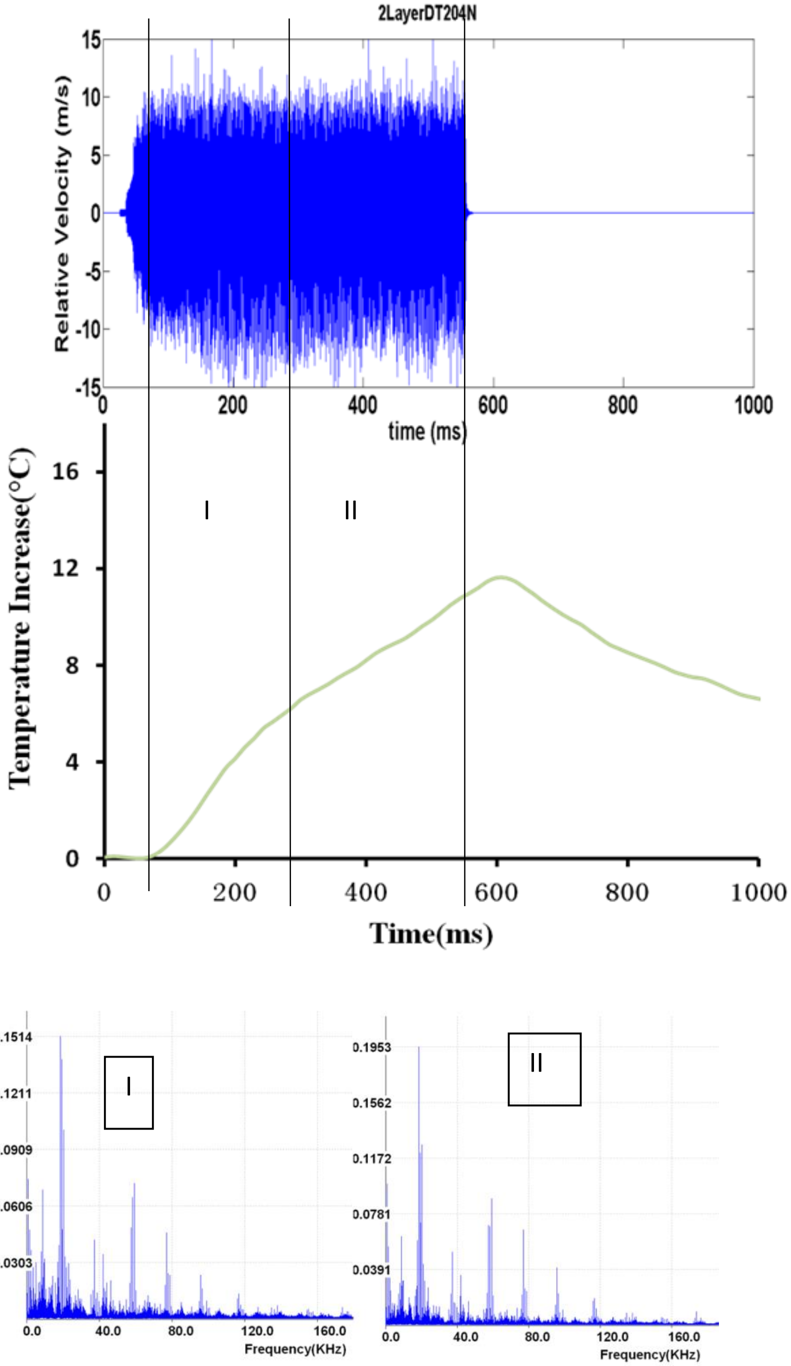

Fig.3.32 Correlating crack vibration and crack heating via waveforms/spectra and temperature -time plot in the case of 2LayerDT as a coupling material at 204N

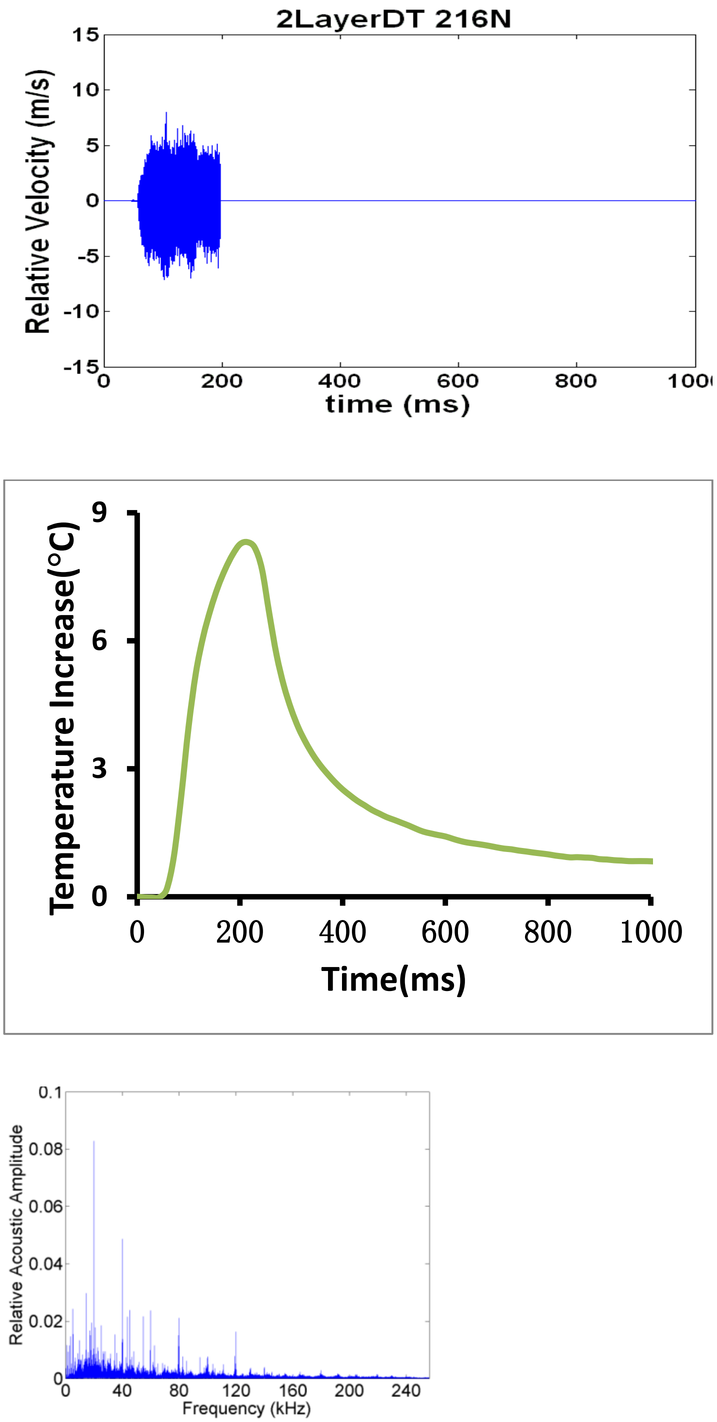

Fig.3.33 Correlating crack vibration and crack heating via waveforms/spectra and temperature -time plot in the case of 2layerDT as a coupling material at 216N

Fig.3.24 shows the T-t plot and the corresponding detailed waveform and its spectrum in the case of 2LayerDT as coupling material at force level 48N. The slope of T-t curve in phase I is barely higher than that in phase II. From the perspective view of waveform, we can also divide the waveform in corresponding time period such as phase I and phase II. Fig.3.25 shows the T-t plot and the detailed waveform and its spectrum in two phases in the case of loading force at 72N. We can also see the difference from phase I to phase II either in T-t plot and its corresponding spectrum and waveform. For phase I, the slope is higher than that of phase II in T-t plot; Fig.3.26 shows the same comparison in the case of loading force at 96N, from the T-t plot we can see phase I has higher slope than phase II, at the same time, from the spectrum we can see phase II shows a few dominated frequencies around which groups of frequencies are formed, However, the phase I spectrum is more or less distributed. The same approach is used for the analysis of the T-t plot and waveform for loading force from 120N to 192N. Fig. 3.27 to Fig. 3.33 show similar comparison between waveform and T-t plot when overloading happens. One observation is that once overloading happens, increase additional force will further reduce the pulse length output from the vibrometer.

3.2.3 Effect of driving frequency

In this section, we focus on the effect of driving frequency on SonicIR system, the experiment setting is similar as the previous section, except we used three different frequency system 20KHz, 30KHz and 40KHz as shown in Fig.3.34. The comparison between three frequency systems is conducted in all six coupling materials, with the loading force at one predefined load.

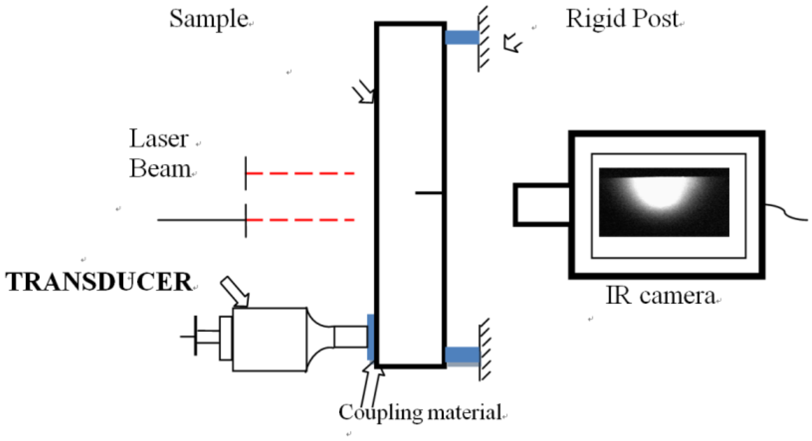

Fig.3.34a Overview of the experiment settings

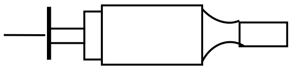

40 kHz Transducer

30 kHz Transducer

20 kHz Transducer

Fig.3.34b Different driving frequency system

Fig.3.34 20 kHz, 30 kHz and 40 kHz transducer systems used in this part

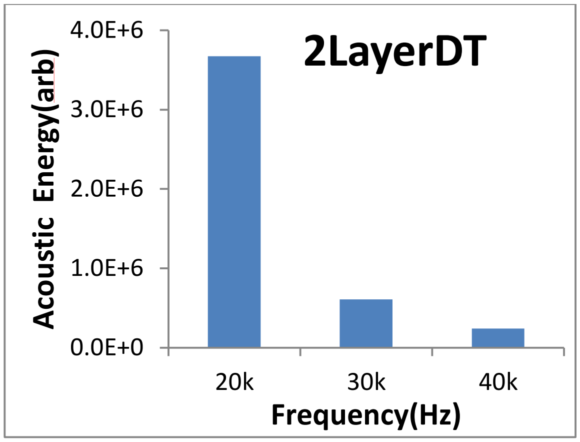

Fig.3. 35 Acoustic energy calculated at one spot of the crack for 2layerDT as coupling material for different frequency system

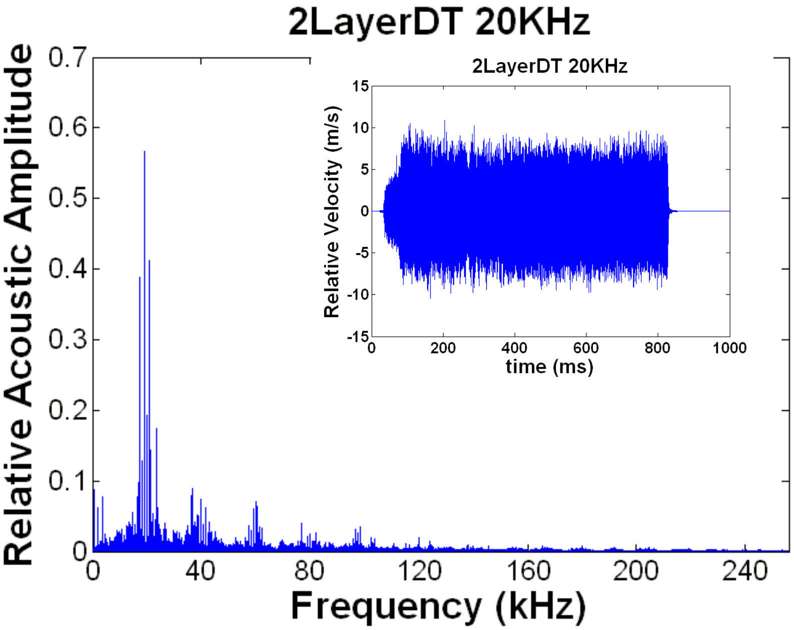

Fig. 3.36 Relative vibration waveform and its spectrum with 2layerDT as a coupling material at loading force 168N for 20 kHz frequency system

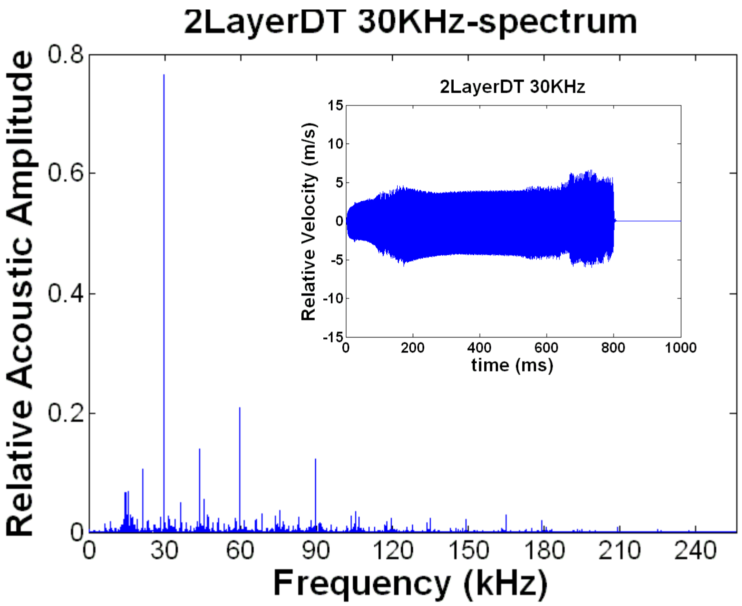

Fig.3.37 Relative vibration waveform and its spectrum with 2layerDT as a coupling material at loading force 168N for 30 kHz frequency system

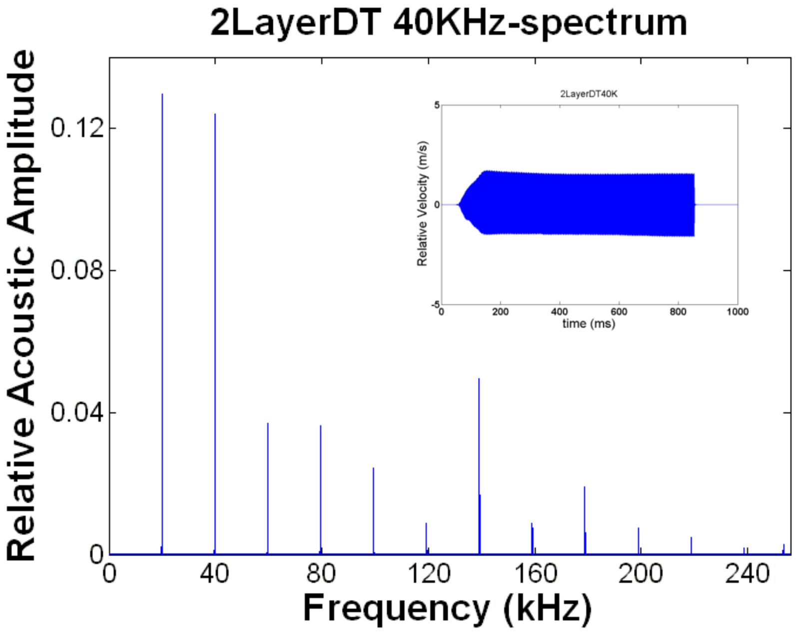

Fig.3.38 Relative vibration waveform and its spectrum with 2layerDT as a coupling material at loading force 168N for 40 kHz frequency system

Fig.3.35 to Fig.3.38 show the acoustic energy comparison for different frequency system for 2LayerDT as coupling material, we can see that 20KHz has highest acoustic energy, while 40KHz has lowest acoustic energy, from the waveform in Fig.3.38 we can see the obvious difference between the waveform of these three frequency systems. One thing we should mention on the frequency spectrum is that the 20KHz has multiple chaos frequency, while the other two are harmonic frequency. This is the reason for the difference of the thermal energy and T-t plot shown in below.

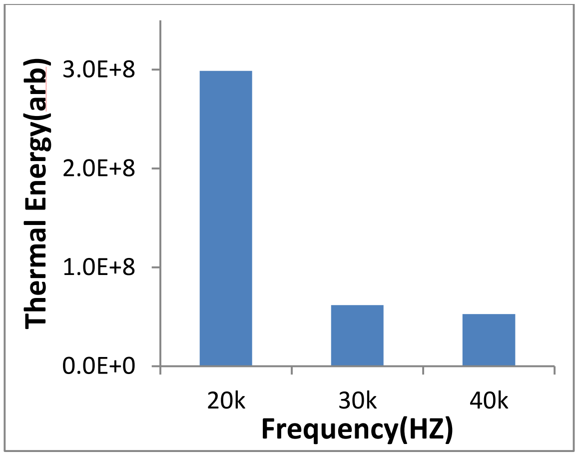

Fig.3.39 Thermal Energy calculated at one spot of the crack for 2layerDT as coupling material with different frequency system

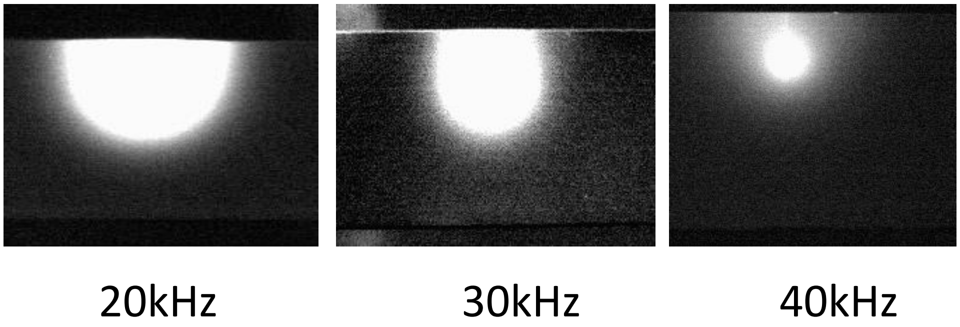

Fig.3.40 IR Images of the crack taken with the different frequency system at 168N for 2layerDT as coupling material

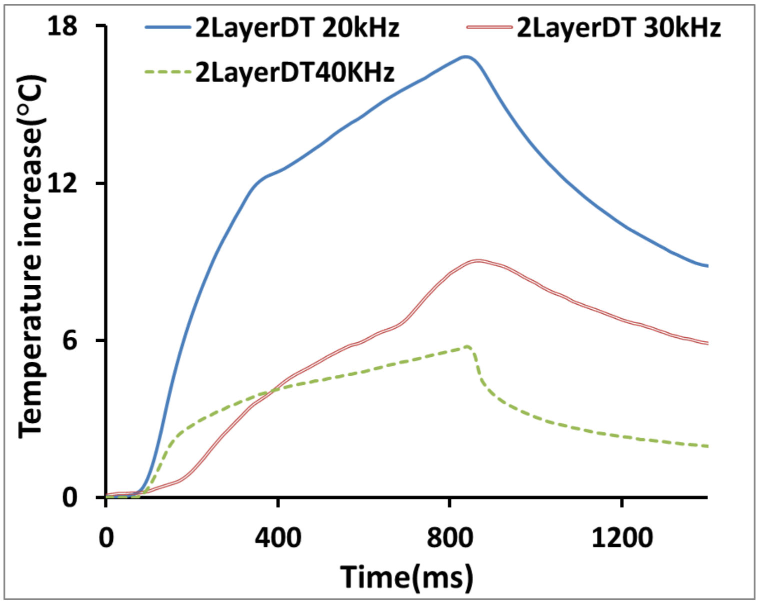

Fig.3.41 Temperature - time plots of the crack for different frequency system at168N as 2layerDT as coupling material

Fig.3.39 shows the thermal energy calculated for 2LayerDT as coupling materials for these three frequency systems, while Fig. 3.40 shows the IR image of the sample for 2LayerDT as coupling material for these three, the same contrast is applied in the images. Fig.3.41 shows the corresponding temperautere- time plot for these three frequency system. We can see the same trend as acoustic energy. From here, we can get clear image that 20KHz system is the best among these threee for 2LayerDT as coupling material.

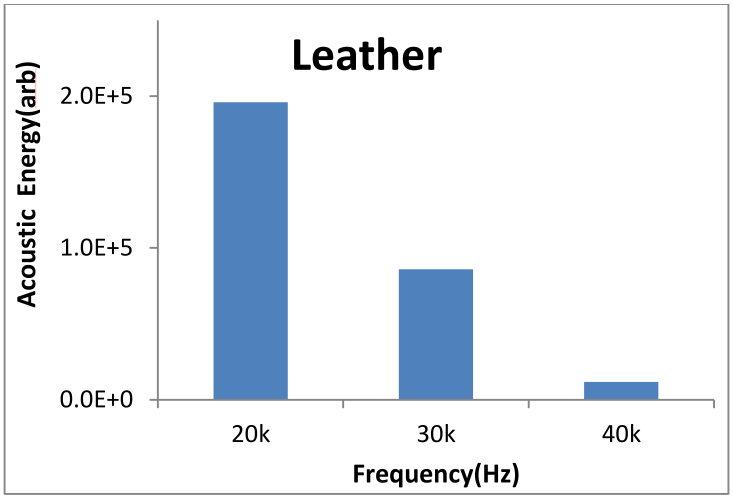

Fig.3.42 Acoustic energy calculated at one spot of the crack for Leather as coupling material for different frequency system

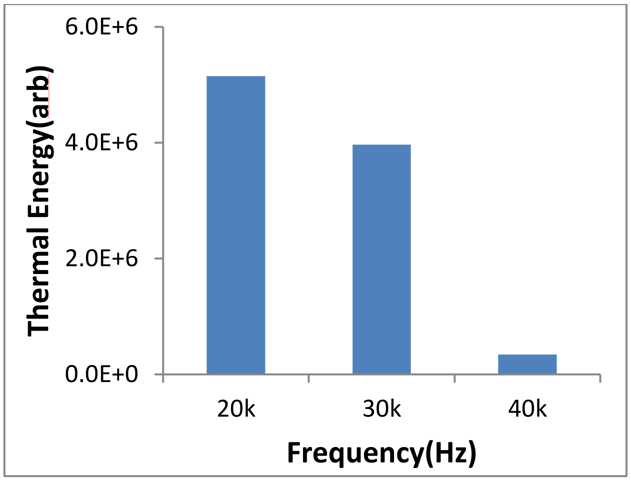

Fig.3.43 Thermal energy calculated at one spot of the crack for Leather as coupling material for different frequency system

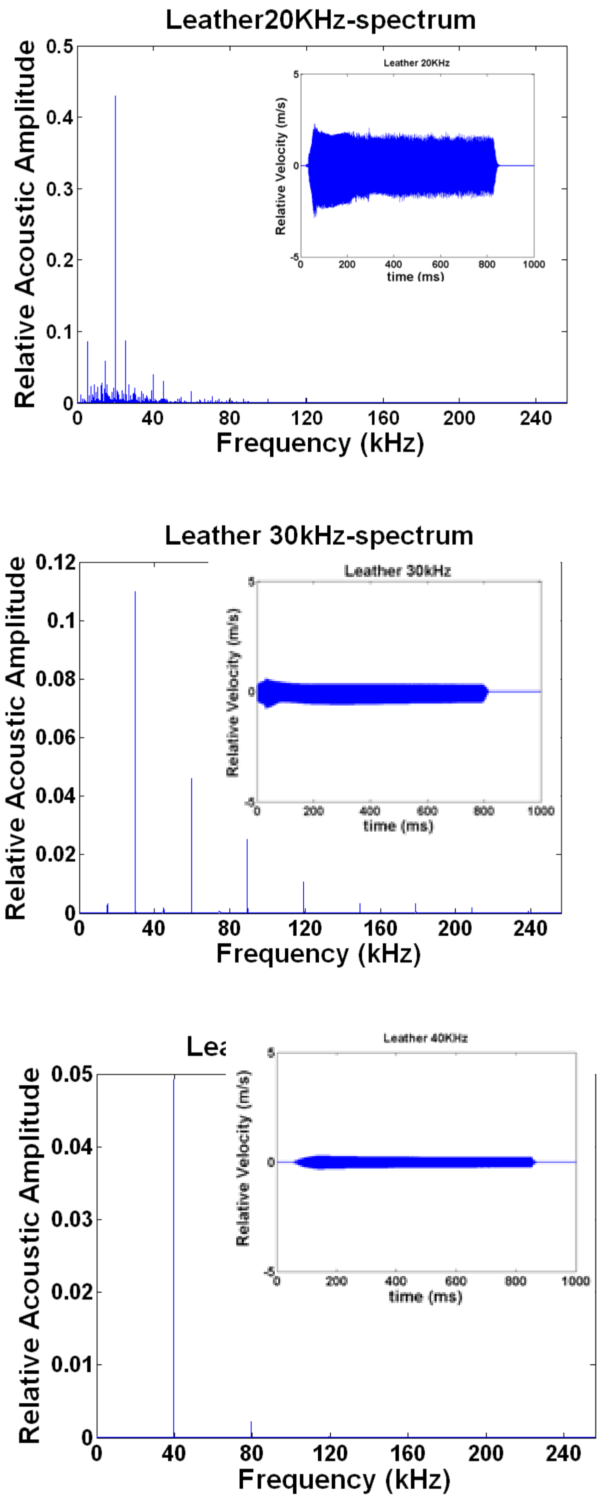

Fig.3.44 Relative vibration waveform and its spectrum with Leather as a coupling material at loading force 168N for different frequency system

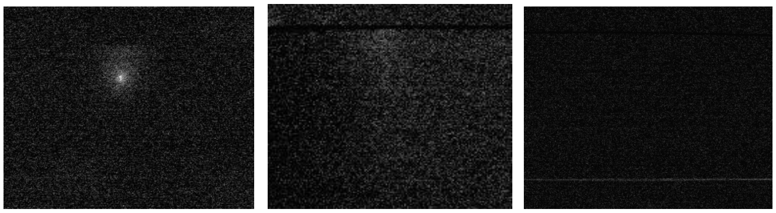

20KHz 30KHz 40KHz

Fig.3.45 IR Images of the crack taken with the different frequency system at 168N for Leather as coupling material

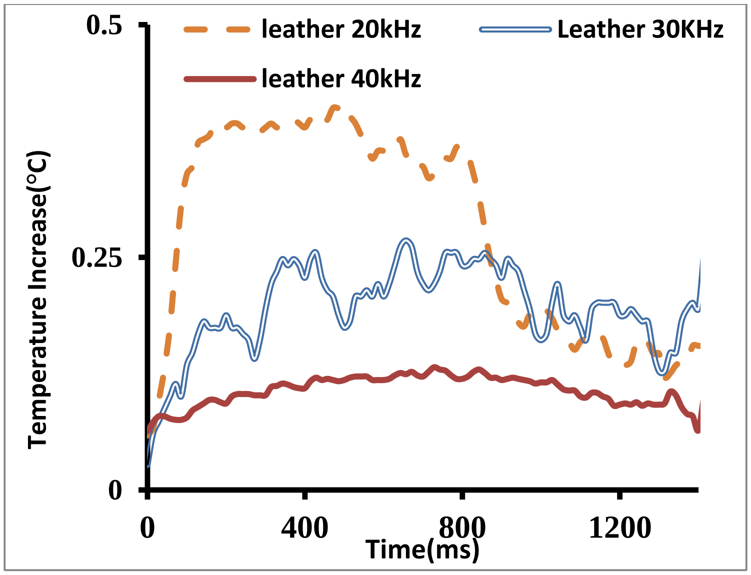

Fig.3.46 Temperature - time plots of the crack for different frequency system at168N as Leather as coupling material

Fig. 3.42 to Fig.3.46 shows the comparison of the thermal energy and acoustic energy for Leather as coupling material. The same approach is used as 2LayerDT as coupling mateiral. We can see clear again chaos will generate more energy to the system.

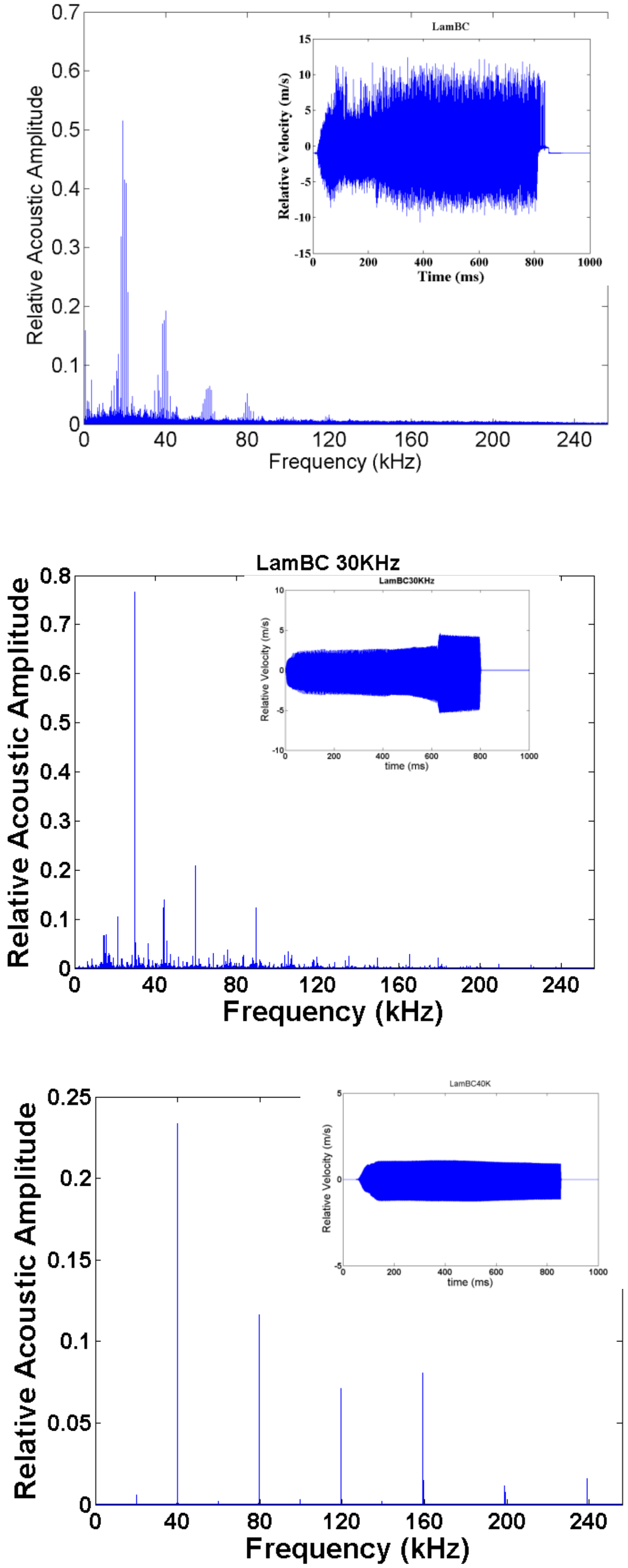

Fig.3.47 Relative vibration waveform and its spectrum with LamBC as a coupling material

at loading force 168N for different frequency system

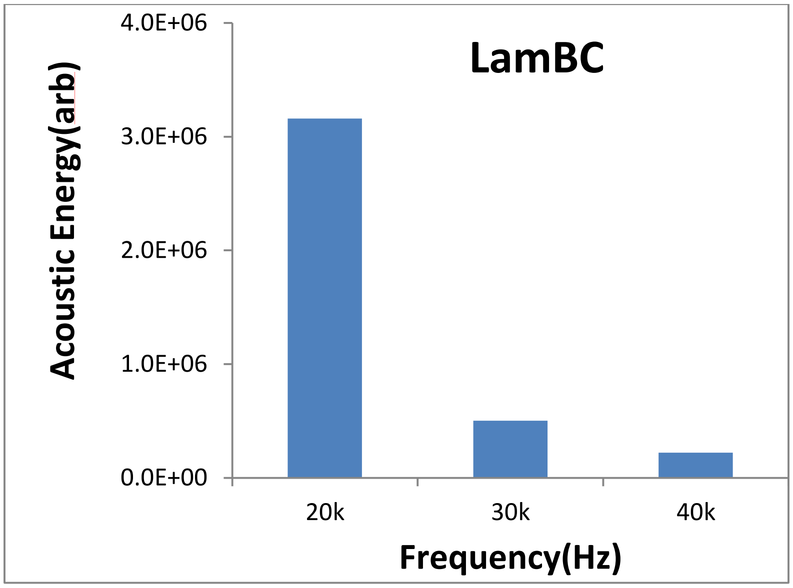

Fig.3.48 Acoustic Energy comparison for LamBC as coupling material in different frequency system

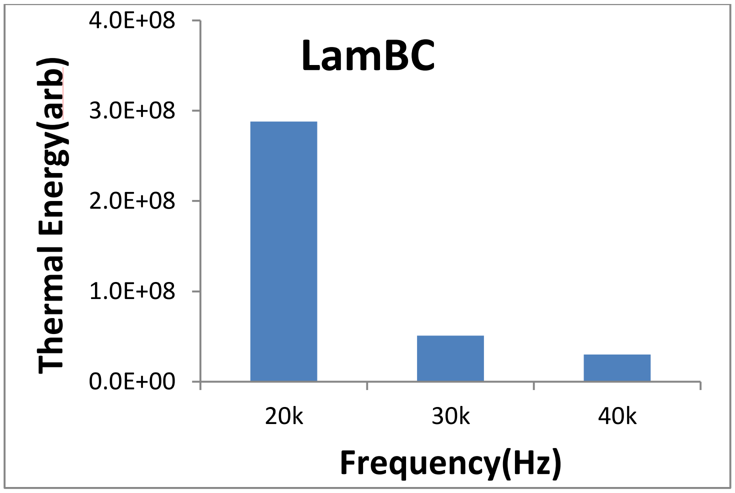

Fig.3.49 Thermal Energy comparison for LamBC as coupling material in different frequency system

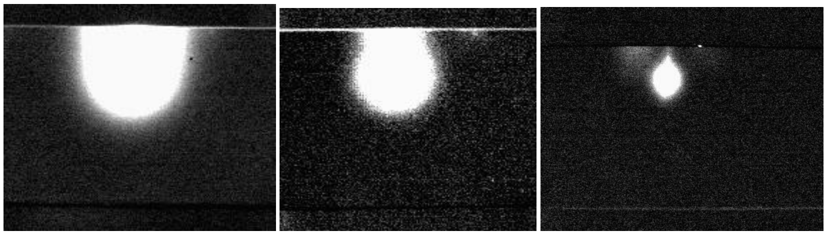

20KHz 30KHz 40KHz

Fig.3.50 IR Images of the crack taken with the different frequency system at 168N for LamBC as coupling material

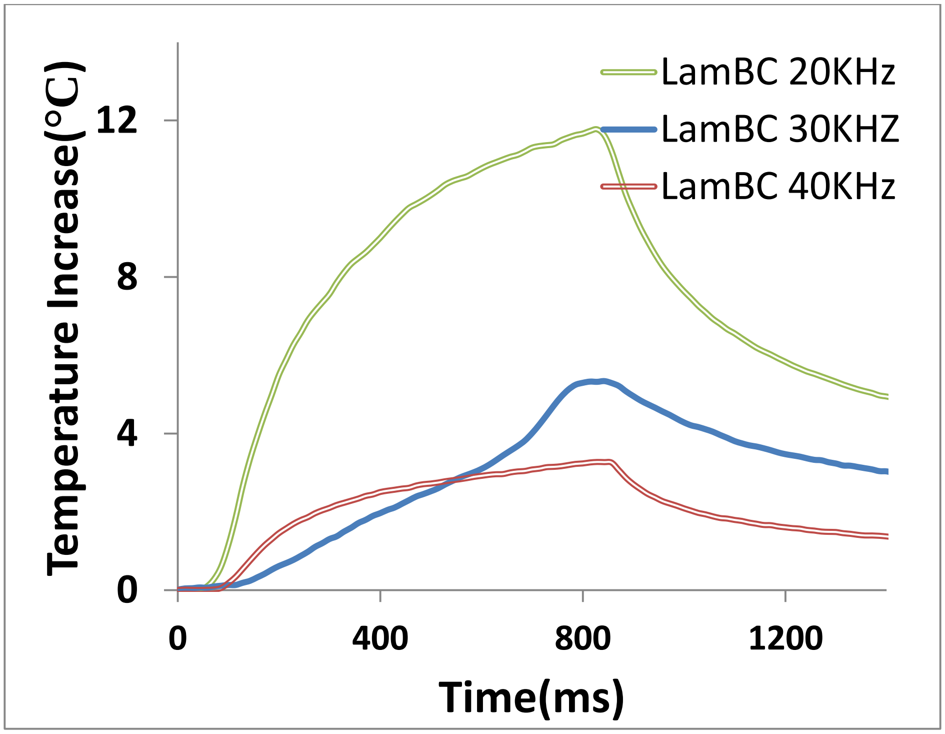

Fig.3.51 Temperature - time plots of the crack for different frequency system at168N as LamBC as coupling material

Fig. 3.47 to Fig.3.51 shows the comparison of the thermal energy and acoustic energy for LamBC as coupling material. The same approach is used as 2LayerDT as coupling mateiral.Again, we can see 20KHz is the best among these three system.

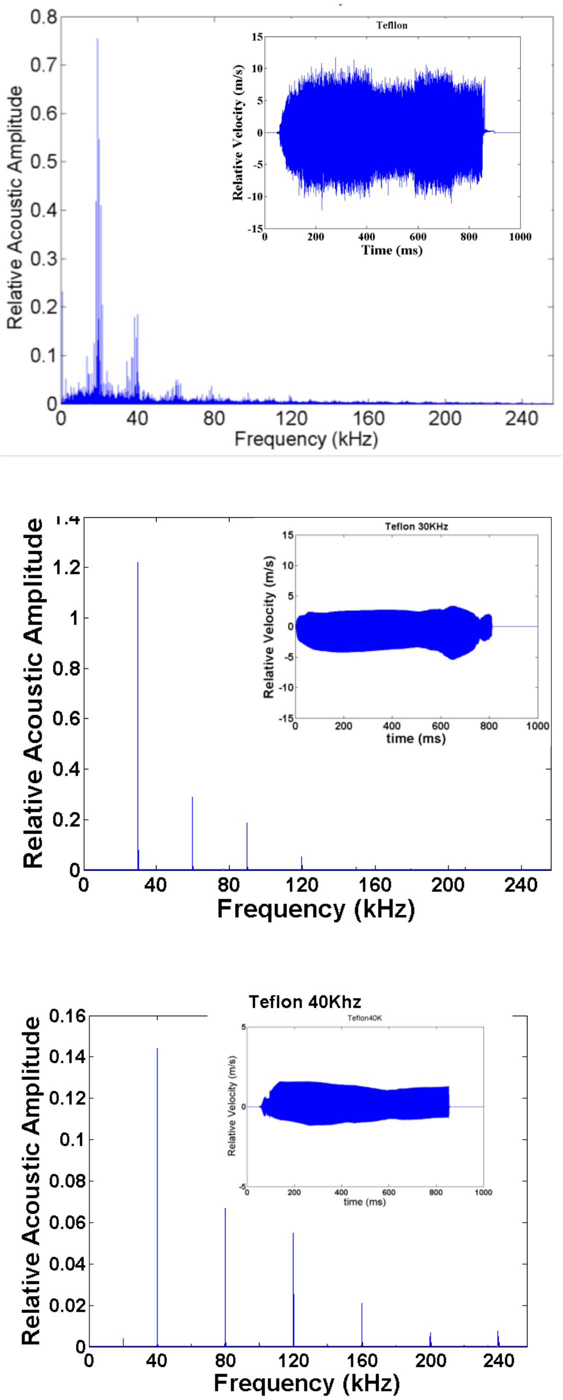

Fig.3.52 Relative vibration waveform and its spectrum with Teflon as a coupling material at loading force 168N for different frequency system

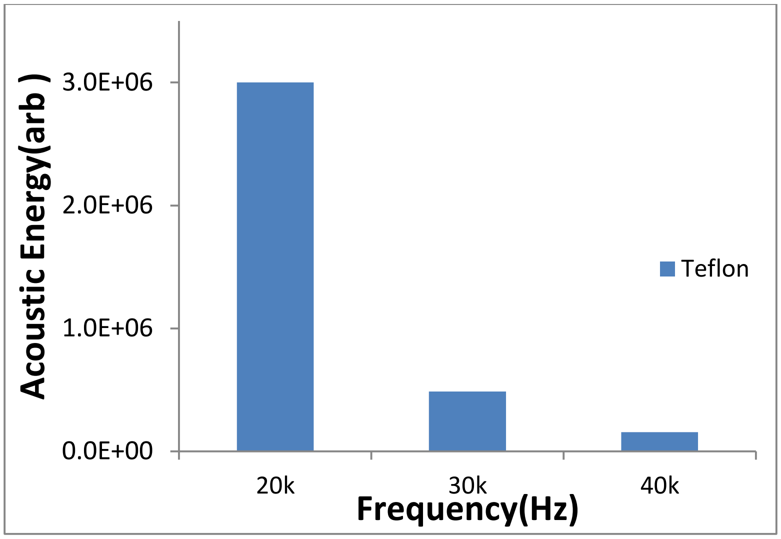

Fig.3.53 Acoustic Energy comparison for Teflon as coupling material in different frequency system

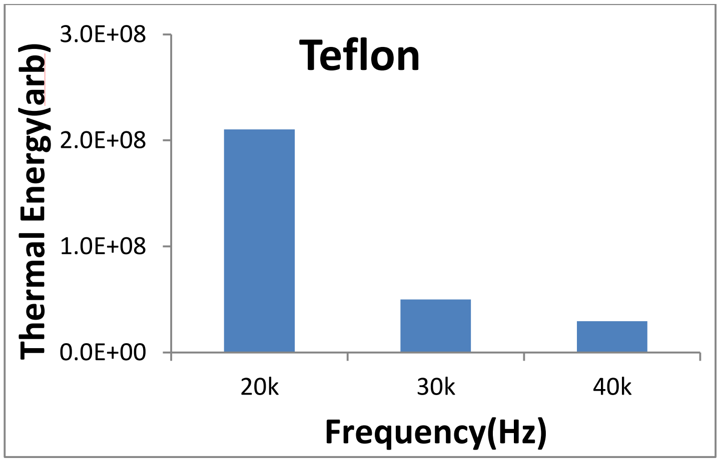

Fig.3.54 Thermal Energy comparison for Teflon as coupling material in different frequency system

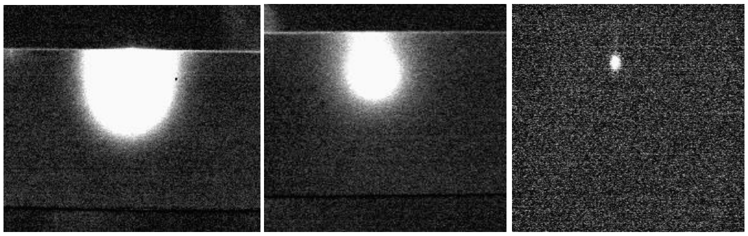

20KHz 30KHz 40KHz

Fig.3.55 IR Images of the crack taken with the different frequency system at 168N for Teflon as coupling material frequency system

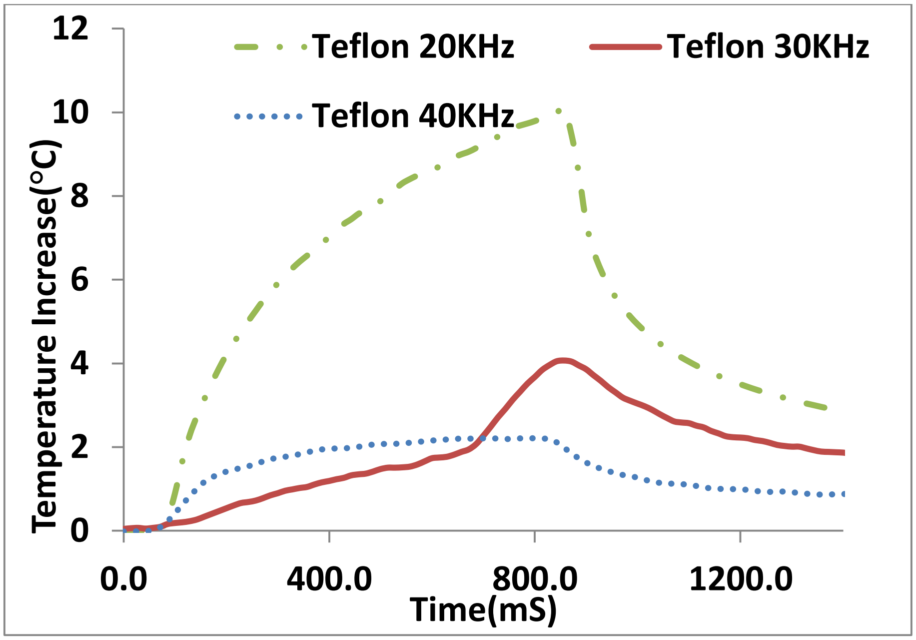

Fig.3.56 Temperature - time plots of the crack for different frequency system at168N as Teflon as coupling material

Fig. 3.52 to Fig.3.57 show the comparison of the thermal energy and acoustic energy for Teflon as coupling material. The same approach is used as 2LayerDT as coupling mateiral.Again, we can see 20KHz is the best among these three system.

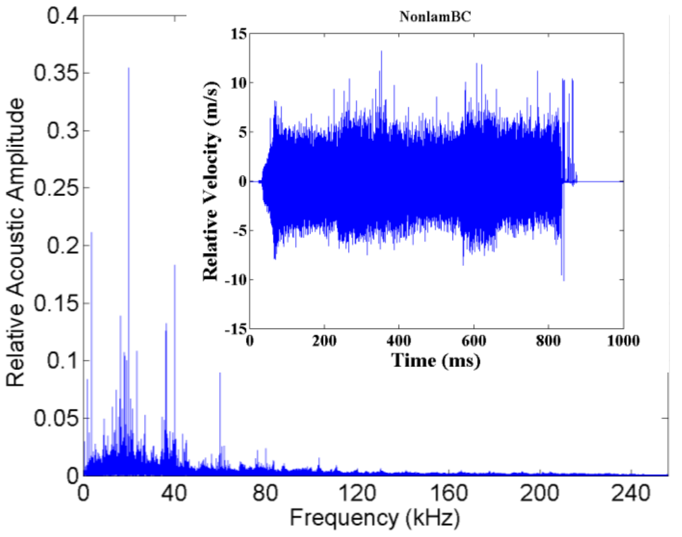
Relative Acoustic Amplitude
0.4
0.35
0.3
0.25
0.2
0.15
0.1
0.05
0
0
40
80
120
160
200
240
Frequency (kHz)
NonlamBC
Relative Velocity (m/s)
15
10
5
0
-5
-10
-15
0
200
400
600
800
1000
Time (ms)

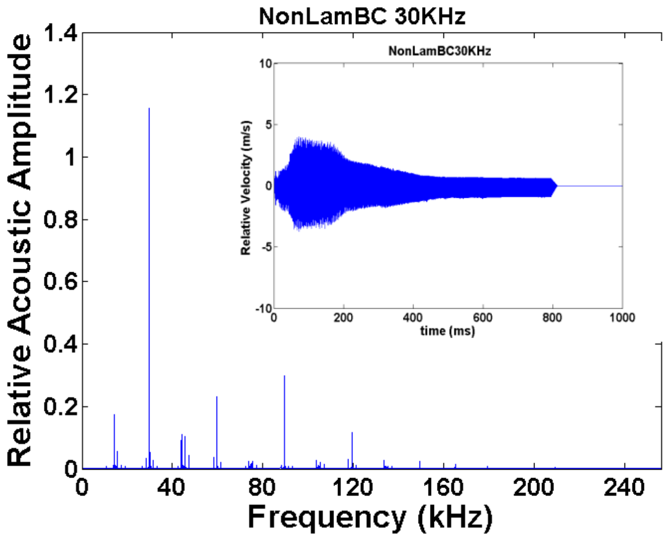
NonLamBC 30KHz
Relative Acoustic Amplitude
1.4
1.2
1
0.8
0.6
0.4
0.2
0
0
40
80
120
160
200
240
Frequency (kHz)
NonLamBC30KHz
Relative Velocity (m/s)
10
5
0
-5
-10
0
200
400
600
800
1000
time (ms)

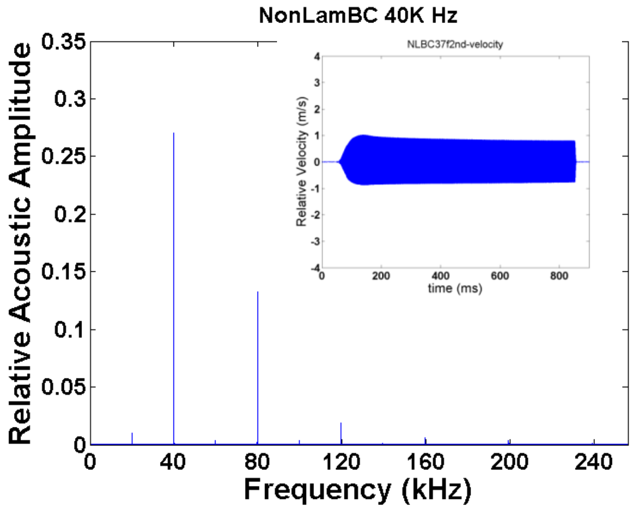
NonLamBC 40K Hz
Relative Acoustic Amplitude
0.35
0.3
0.25
0.2
0.15
0.1
0.05
0
0
40
80
120
160
200
240
Frequency (kHz)
NLBC37f2nd-velocity
Relative Velocity (m/s)
4
3
2
1
0
-1
-2
-3
-4
0
200
400
600
800
time (ms)

Fig.3.57 Relative vibration waveform and its spectrum with NonLamBC as a coupling material at loading force 168N for different frequency system

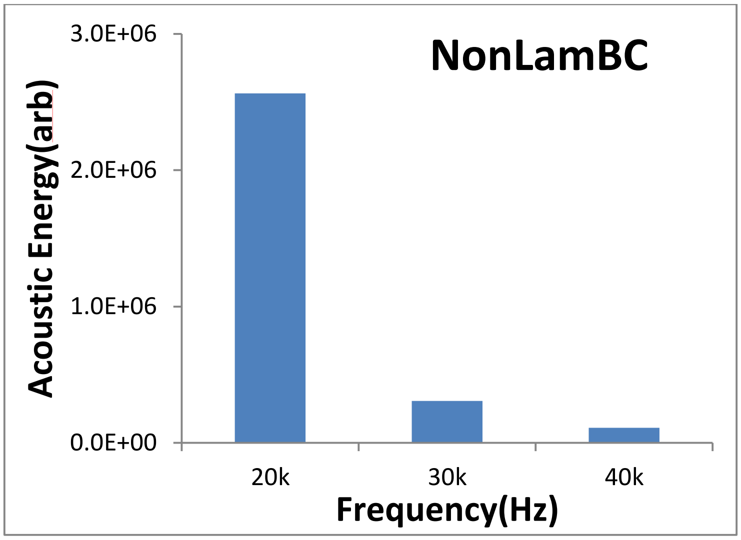

Fig.3.58 Acoustic Energy comparison for NonLamBC as coupling material in different frequency system

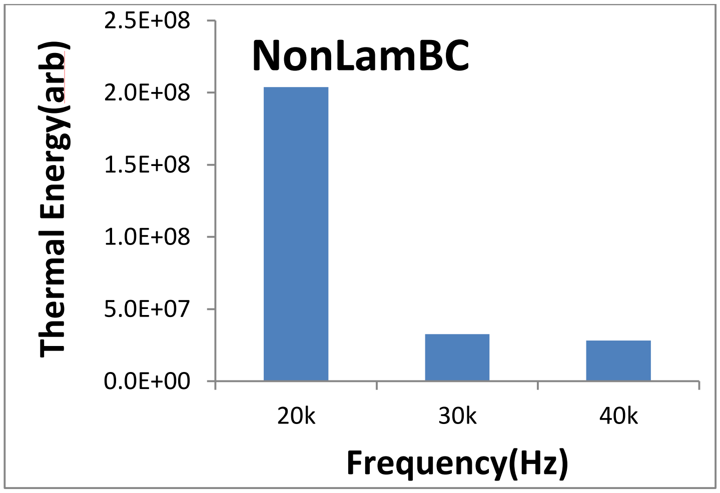

Fig.3.59 Thermal Energy comparison for NonLamBC as coupling material in different frequency system

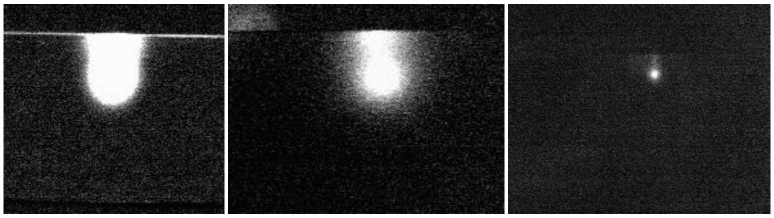

Fig.3.60 IR Images of the crack taken with the different frequency system at 168N for NonLamBC as coupling material

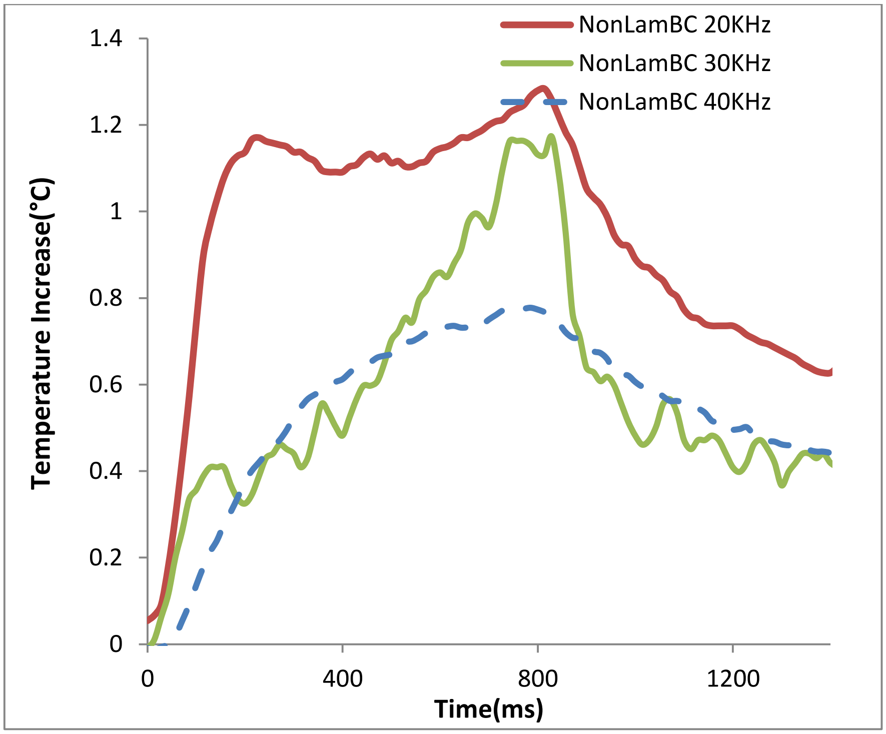

Fig.3.61 Temperature - time plots of the crack for different frequency system at168N as NonLamBC as coupling material

Fig. 3.57 to Fig.3.61 shows the comparison of the thermal energy and acoustic energy for NonLamBC as coupling material. The same approach is used as 2LayerDT as coupling mateiral.Again, we can see 20KHz is the best among these three system.

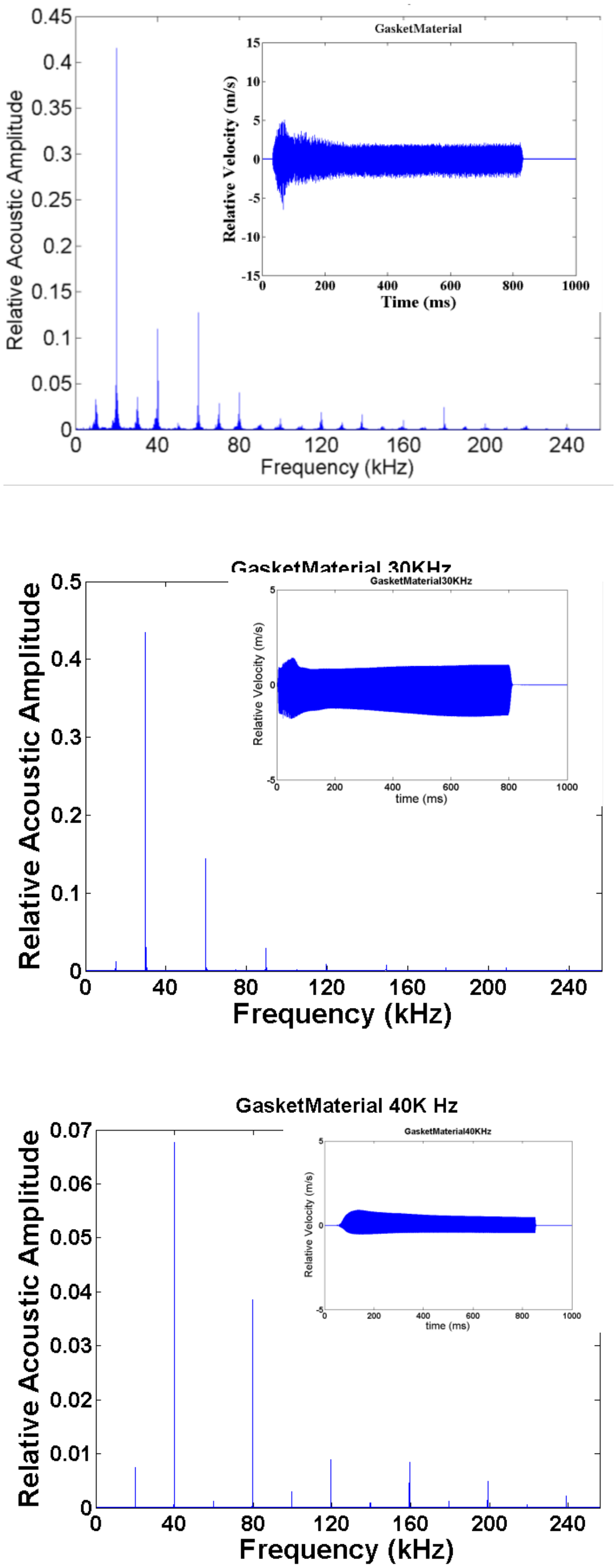

Fig.3.62 Relative vibration waveform and its spectrum with GasketMaterial as a coupling

material at loading force 168N for different frequency system

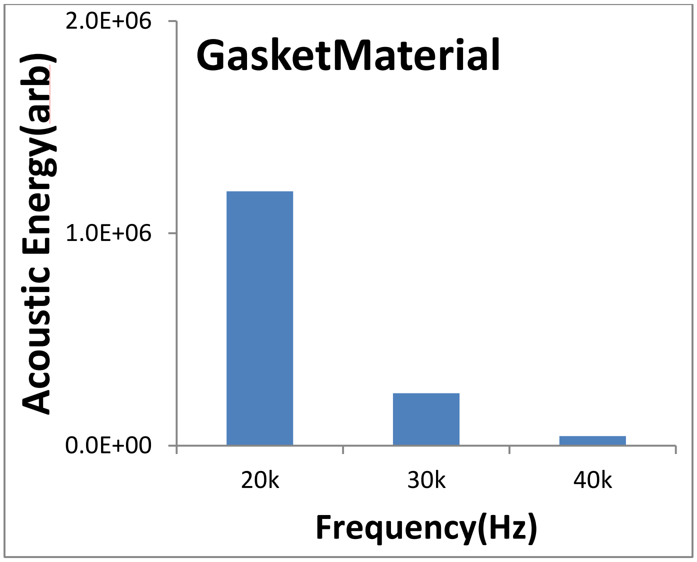

Fig.3.63 Acoustic Energy comparison for GasketMaterial as coupling material in different frequency system

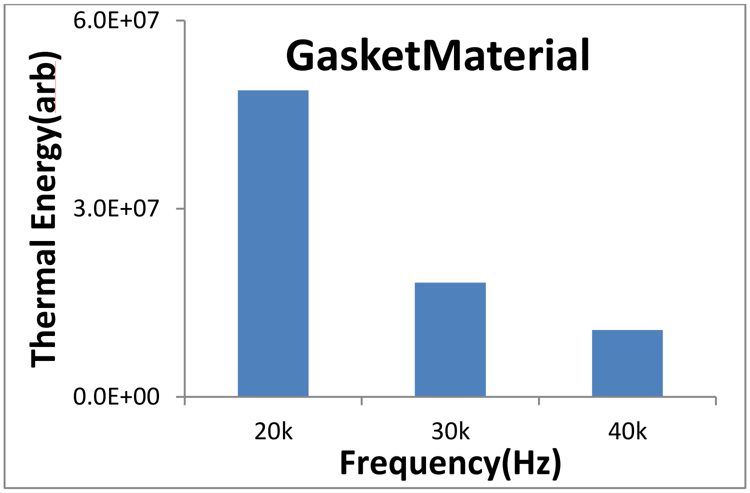

Fig.3.64 Thermal Energy comparison for GasketMaterial as coupling material in different frequency system

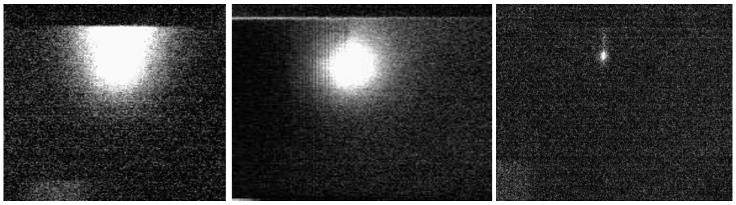

Fig.3.65 IR Images of the crack taken with the different frequency system at 168N for GasketMaterial as coupling material

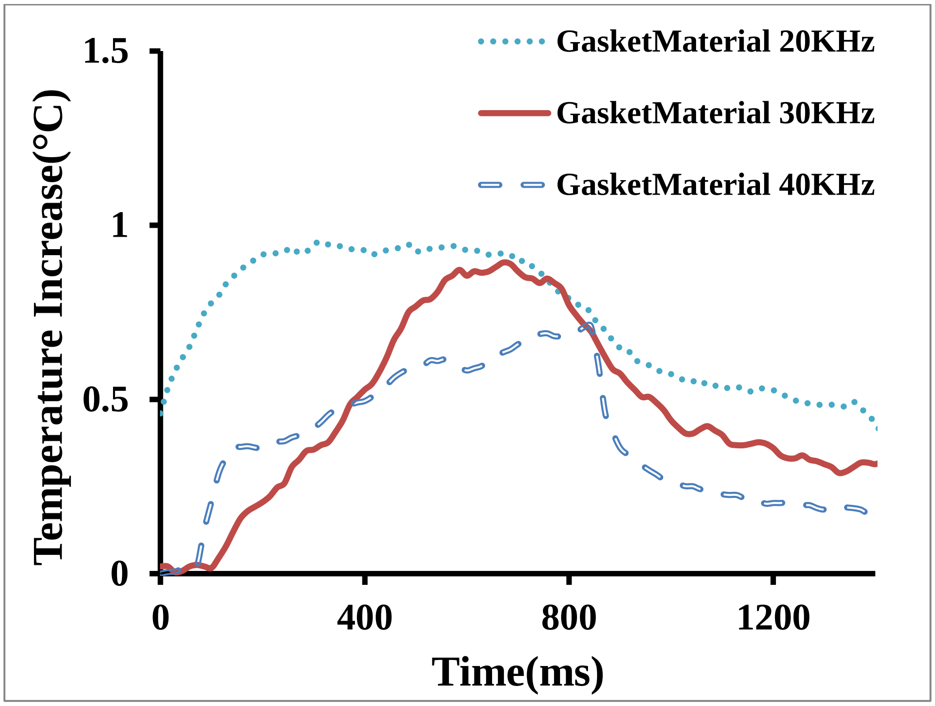

Fig.3.66 Temperature - time plots of the crack for different frequency system at168N as GasketMaterial as coupling material

Fig. 3.62 to Fig.3.66 show the comparison of the thermal energy and acoustic energy for GasketMaterial as coupling material. The same approach is used as 2LayerDT as coupling mateiral.Again, we can see 20KHz is the best among these three system.

3.3 Non-Linear effect of coupling materials on SonicIR at Al wheel disk structure

From previous comparison of the different frequency system on different coupling materials, we characterized the coupling materils used in three frequency system quantitatively, and all the results show that 20KHz system is the best among these three system. But we can not get definite conclusion on this compariosn. In order to have more structure part involved, we gave extra test on Al wheel disk sample for further analysis.

Fig. 3.67 shows the expereimant setting for 20KHz for this sample, the image below shows the location of the crack.

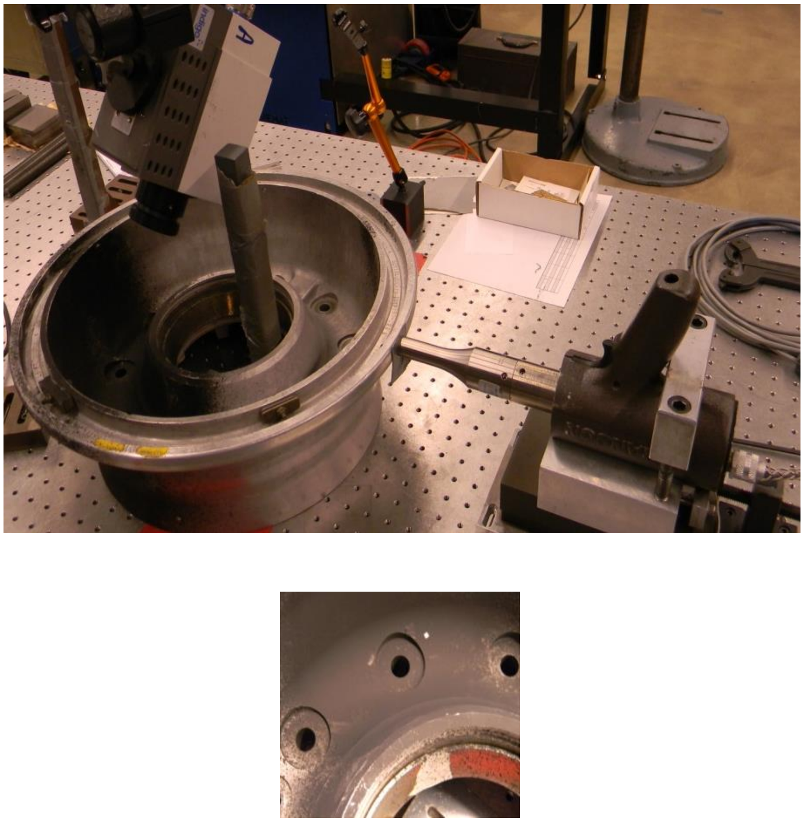

Fig.3. 67Experiment settings and crack location in Al wheel sample for different frequency system

Using the experiment setting as shown above, similarly, we can conduct our experiment on three aspect as shown from Al bar structure:

3.3.1 Effect of coupling materials

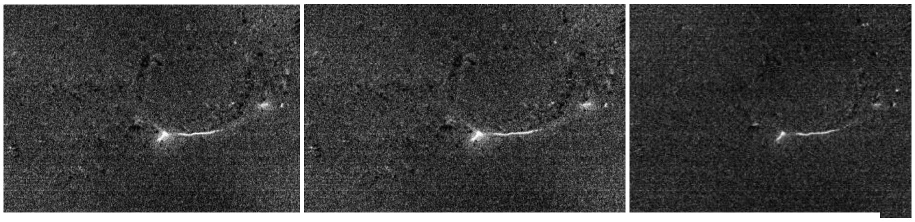

2layerDT LamBC Teflon

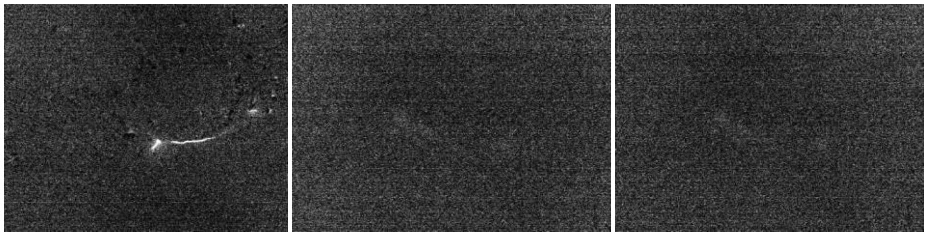

NonLamBC GasketMaterial Leather

Fig.3.68 Thermal image of the crack from 6 coupling materials

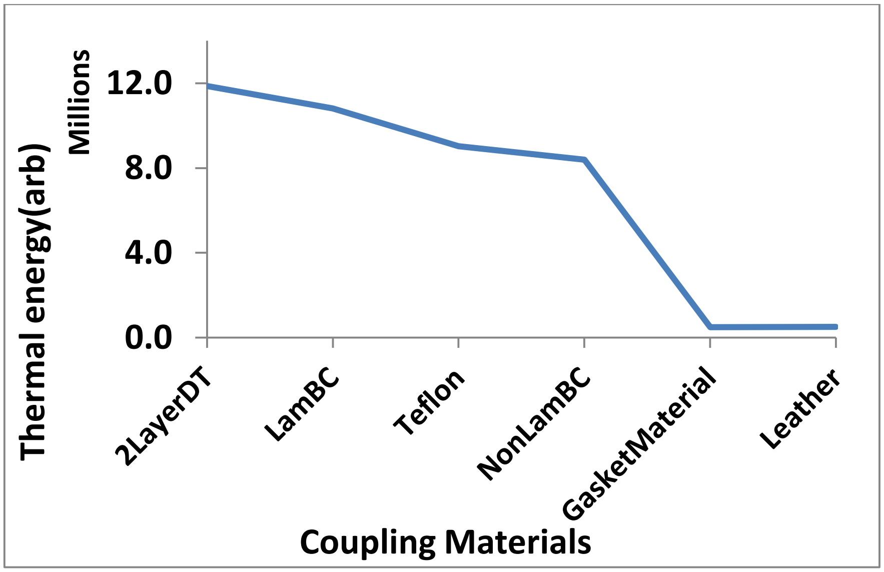

Fig.3.69 Thermal energy of crack area from 6 different coupling materials

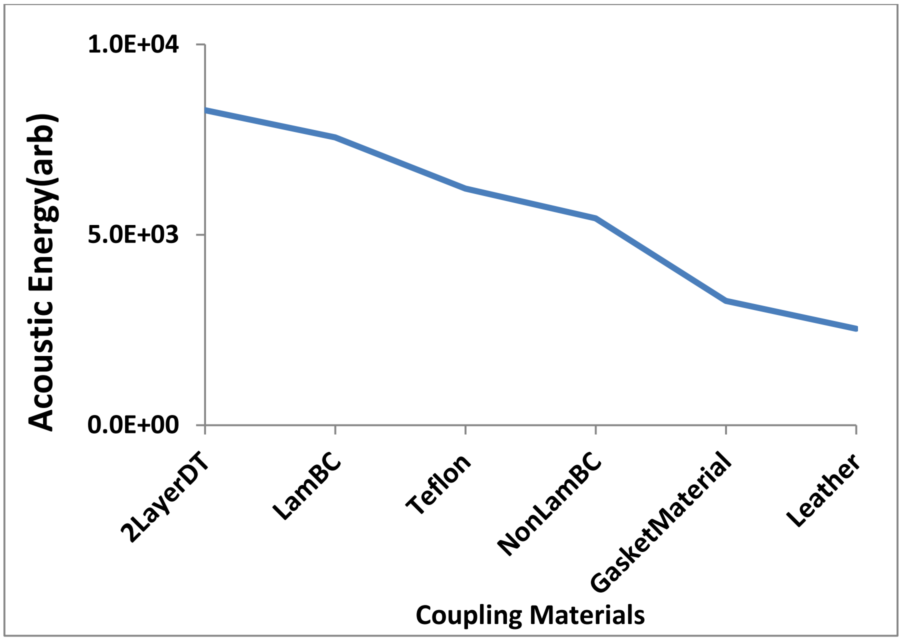

Fig.3.70 Acoustic energy of crack area from 6 different coupling materials

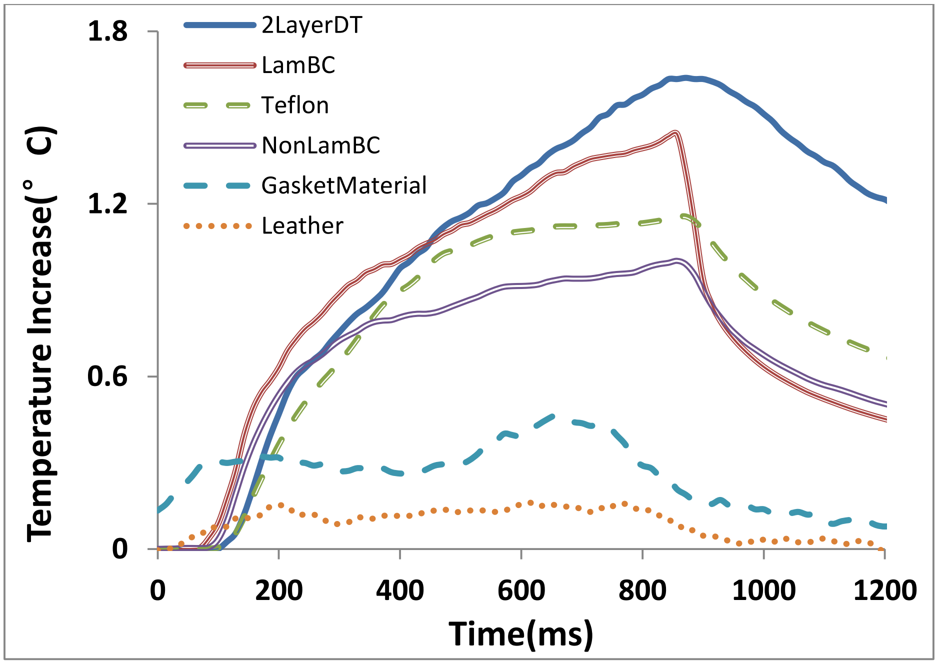

Fig.3.71 Temperature increase from crack from six different coupling materials

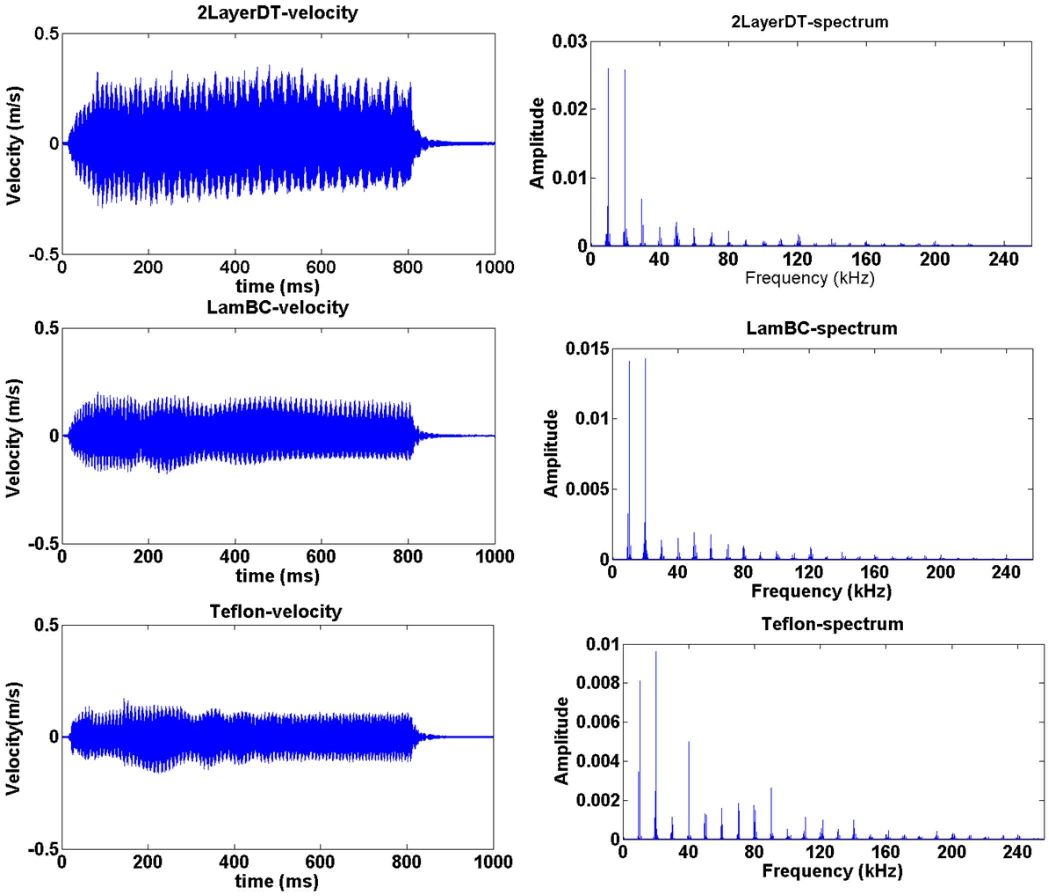
2LayerDT-velocity
Velocity (m/s)
0.5
0
-0.5
0
200
400
600
800
1000
time (ms)
2LayerDT-spectrum
Amplitude
0.03
0.02
0.01
0
0
40
80
120
160
200
240
Frequency (kHz)
LamBC-velocity
Velocity (m/s)
0.5
0
-0.5
0
200
400
600
800
1000
time (ms)
LamBC-spectrum
Amplitude
0.015
0.01
0.005
0
0
40
80
120
160
200
240
Frequency (kHz)
Teflon-velocity
Velocity(m/s)
0.5
0
-0.5
0
200
400
600
800
1000
time (ms)
Teflon-spectrum
Amplitude
0.01
0.008
0.006
0.004
0.002
0
0
40
80
120
160
200
240
Frequency (kHz)

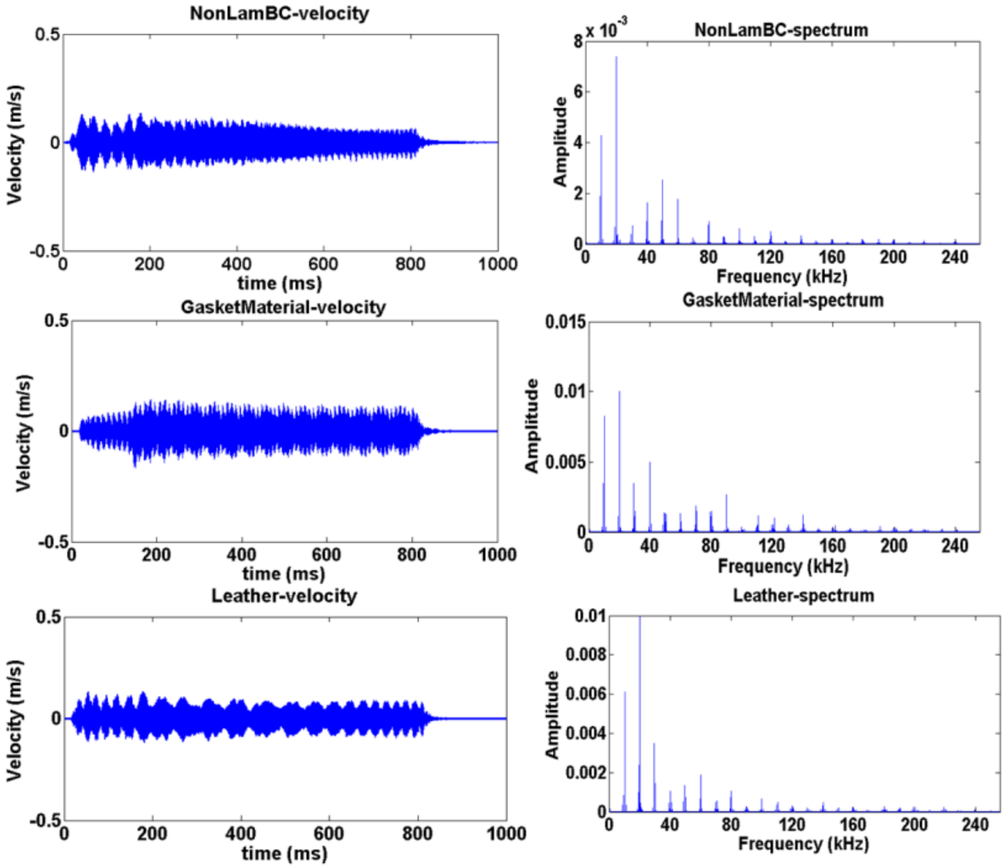

Fig.3.72 comparison of waveform and spectrum for six different coupling materials

Fig.3.68 to Fig.3.72 show the effect of different coupling material to the structure under SonicIR system.

It is shown that the thermal energy levels have the order from the highest to the lowest for the six coupling materials as: 2LayerDT, LamBC, Teflon, NonLamBC, GasketMaterial, and Leather. In Fig.3.68, we present the IR images taken at times when the temperature of the crack reaches its highest value for these six corresponding coupling materials. The same contrast was applied to all these images for visual comparison. The corresponding temperature-time (T-t) plots at the crack are shown in Fig.3.71. In Fig.3.72 and Fig.3.70,the waveform from the crack and its corresponding acoustic energy shows the same trend as the thermal energy levels calculated for these six coupling materials

One phenomena we noticed is that for all these six coupling materials the spectrum from the crack all show non-chaos characterization. Also the amplitude of the waveform is quite smaller compared to that from Al bar structure, partially the reason from the higher mass of the structure.

3.3.2 Effect of loading force

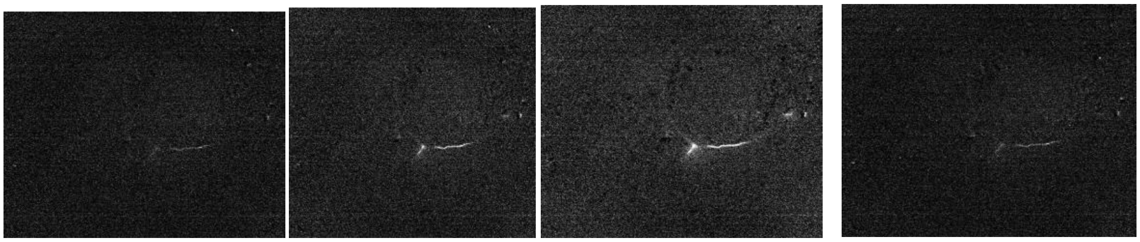

48N 96N 144N 156N

Fig.3.73 Thermal image of crack area for different loading force

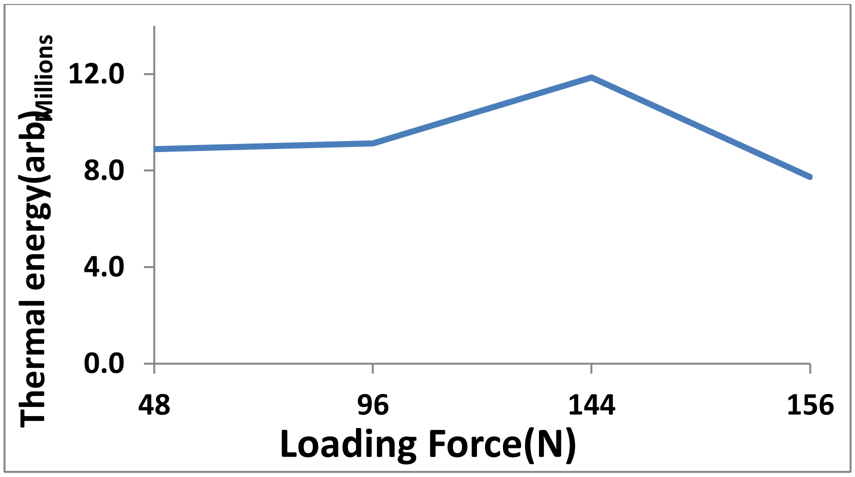

Fig.3.74 Thermal energy of crack area from different loading force

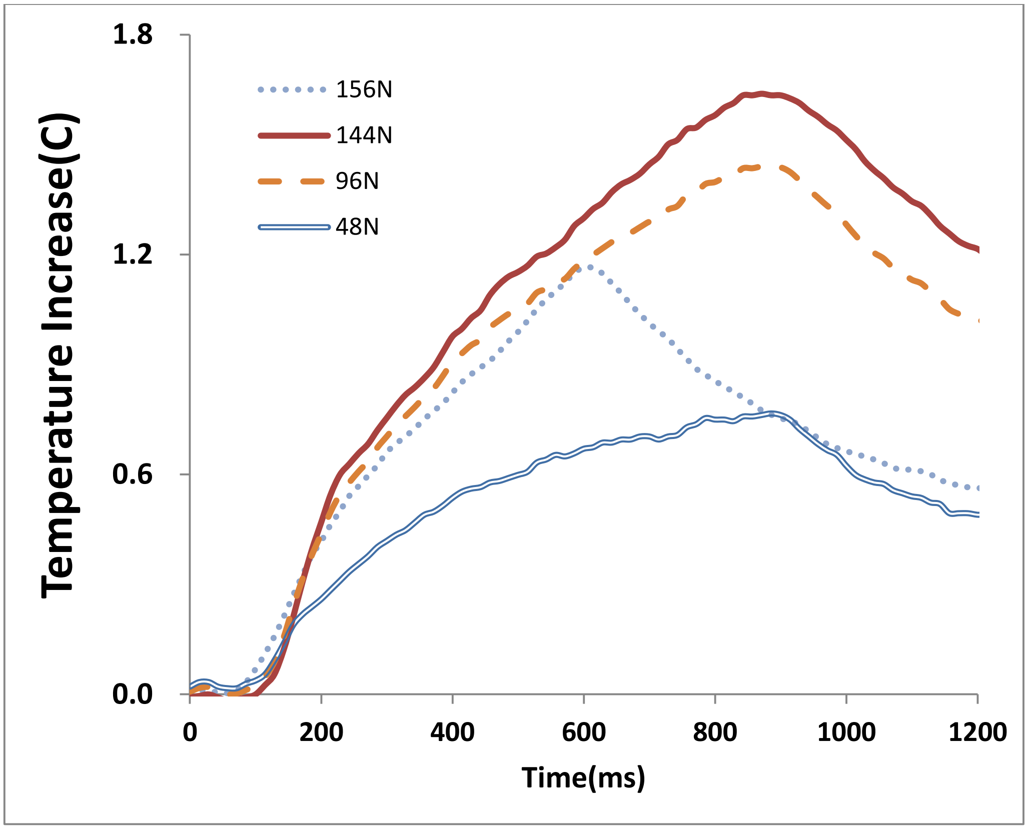

Fig.3.75 Temperature increase from crack from different loading force

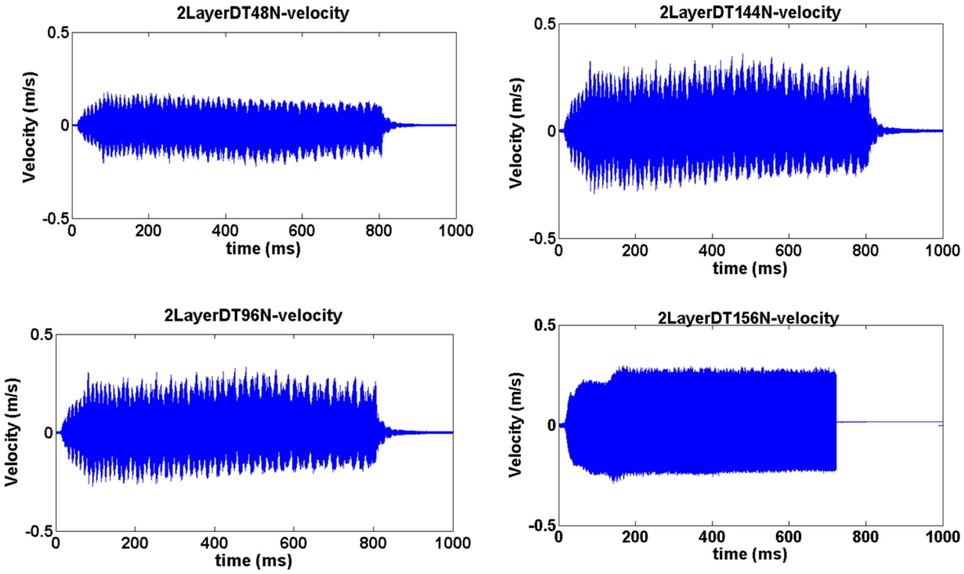

Fig.3.76 comparison of waveform for different loading force

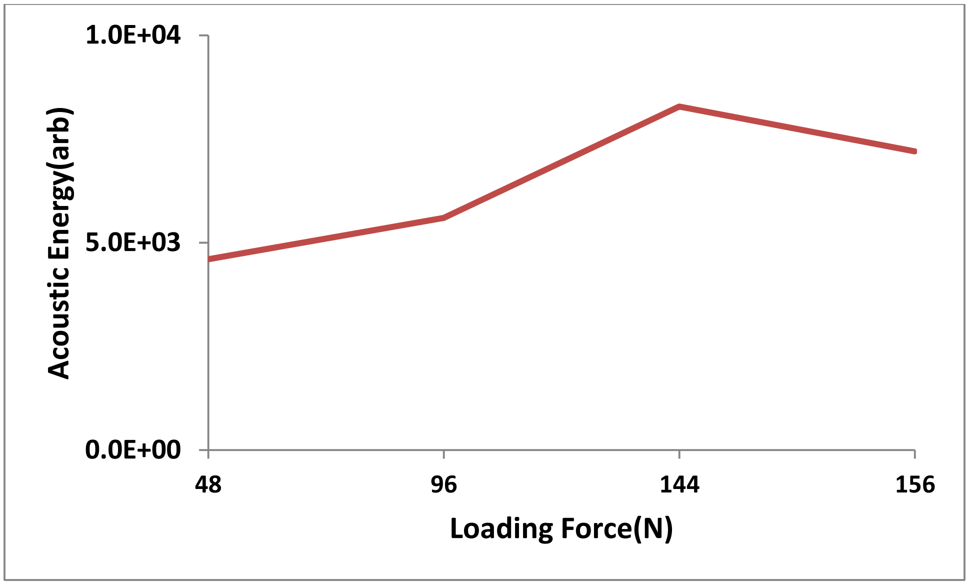

Fig.3.77 Acoustic energy of crack area from different loading force

Fig.3.73 to Fig.3.77 show the effect of loading force to the structure. Similarly to the Al bar structure, we can see the same trend either from acoustic energy or thermal energy, the increase of the loading force will increase the energy output, but there is also limitation for the system, differ from Al bar structure, the over-loading happens earlier, due to the higher mass of the part.

3.3.3 Effect of driving frequency

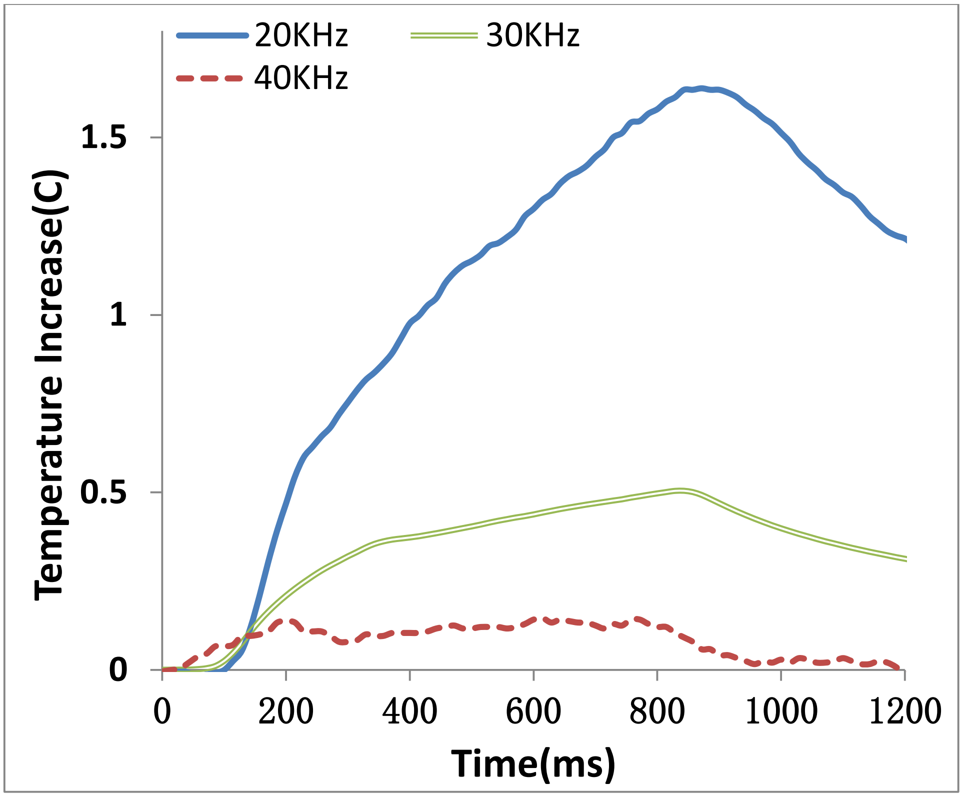

Fig.3.78 Temperature - time plots of the crack on aluminum wheel for different frequency system at 144N as 2LayerDT as coupling material

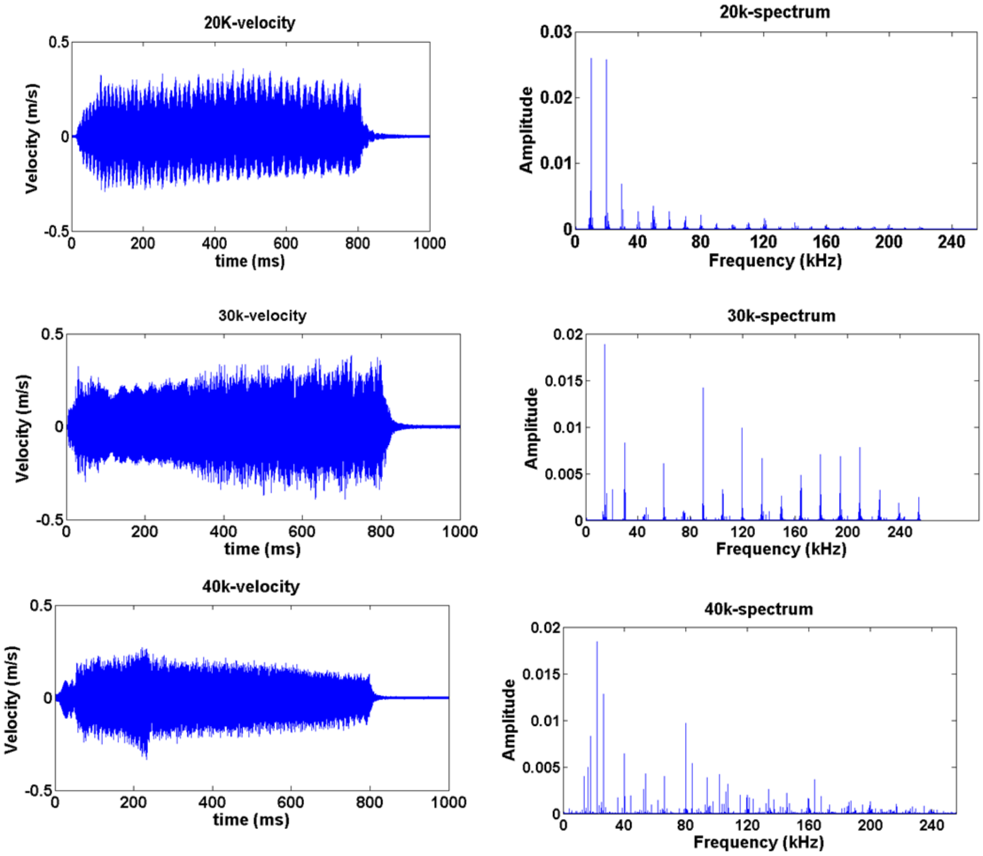

Fig.3.79 Waveform and spectrum from different driving frequency

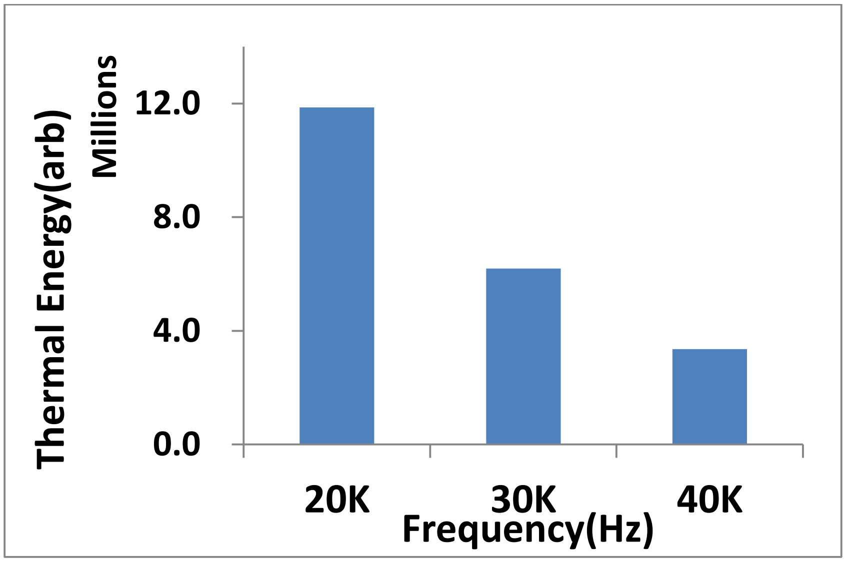

Fig.3.80 Thermal energy of the crack on aluminum wheel for different frequency system at 144N as 2LayerDT as coupling material

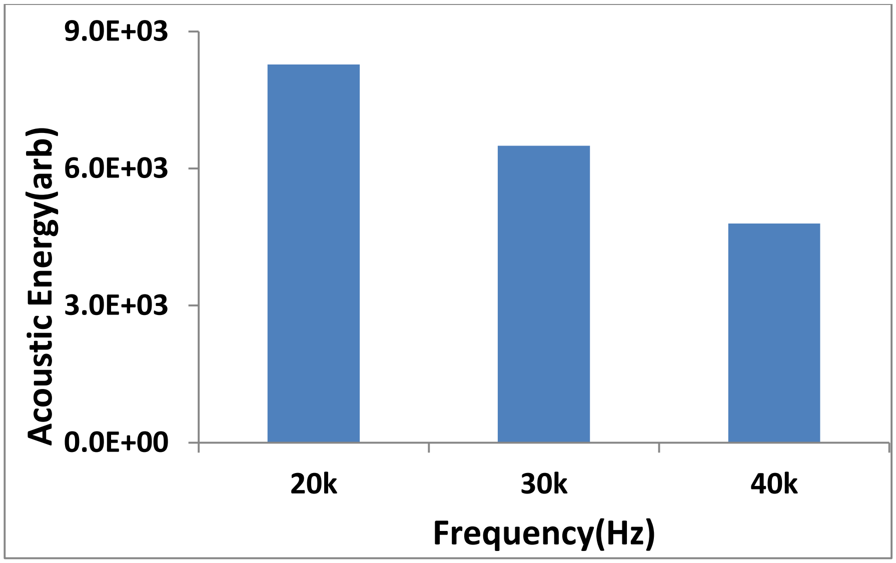

Fig.3.81 Acoustic energy of the crack on aluminum wheel for different frequency system at 144N as 2LayerDT as coupling material

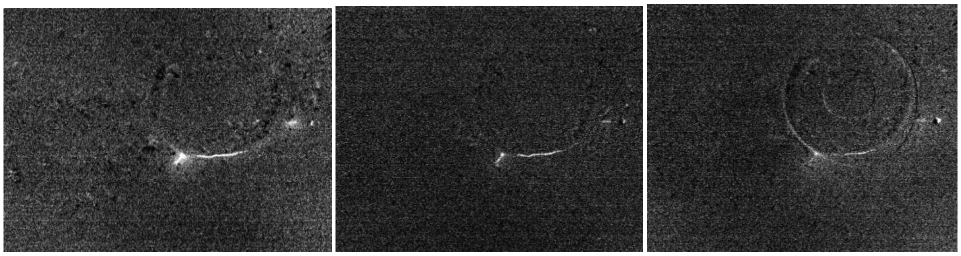
20KHz 30KHz 40KHz

Fig.3.82 Thermal image of the crack on aluminum wheel for different frequency system at 144N as 2LayerDT as coupling material

Fig.3.78 to Fig.3.82 show the effect of the driving frequency to the structure. From Fig.3.78, we can see the 20KHz has highest temperature increase for the crack location, while Fig. 3.82, the thermal image of the part show the same trend as this one.

These comprehensive comparison of the result gave us a clear conclusion on this part, for Aluminum structure, 20KHz frequency system is the best among the three. It is highly recommended that for further research and development, when we have such similar structure , the first priority for the frequency system is 20KHz, then it is 30KHz after that is 40KHz.

CHAPTER FOUR

FINITE ELEMENT ANALYSIS AND SIMULATION RESULTS

4.1 Introduction of Finite Element Analysis:

Finite Element Analysis (FEA) uses a numerical technique to minimize variation calculus and obtain approximate solutions [27]. The target structure is modeled by a set of appropriate finite elements interconnected at points called nodes. The elements have physical properties such as density, Young's modulus, and Poisson's ratio. We performed the simulation work on a simple aluminum sample to analyze the heat transfer mechanism. The finite element software package was used in calculation is LS-DYNA V970 [28, 29]. LS-DYNA is developed at Livermore Software Technology Corporation (LSTC)[37-39]. LS-DYNA is the most advanced general-purpose multiphysics simulation software package. It is originally designed for solving highly nonlinear transient dynamic problems by using explicit time integration and widely used in Automobile, Aerospace, Military, Mechanical, Manufacturing and Bioengineering industry. The calculation results from LS-DYNA are binary files which cannot be read directly. We use Ls-Post as the Post-Processor to display and analysis the results. Usually the FEA simulation is made of these steps:

- Modeling – the first step in FEA is to build up the finite element model and set up boundary conditions. The topology and geometry of the structure is been set up in this step, a variety of elements can be used in either 1D, 2D, or 3D form. The main objective of this step is to realistically reflect the physical conditions and features of the real model.

- Calculation – solution of the finite element model. The second step of the FEA is calculation. The FEM processes a series of calculations based on loads, boundary conditions and material properties which applied to the model. The results such as displacement, stress, strain and temperature are collected in this step.
- Post-processing – display the results. The results collected in step two can be viewed by using post-processing tools which embedded in FEM. Results of specified location can be displayed graphically.

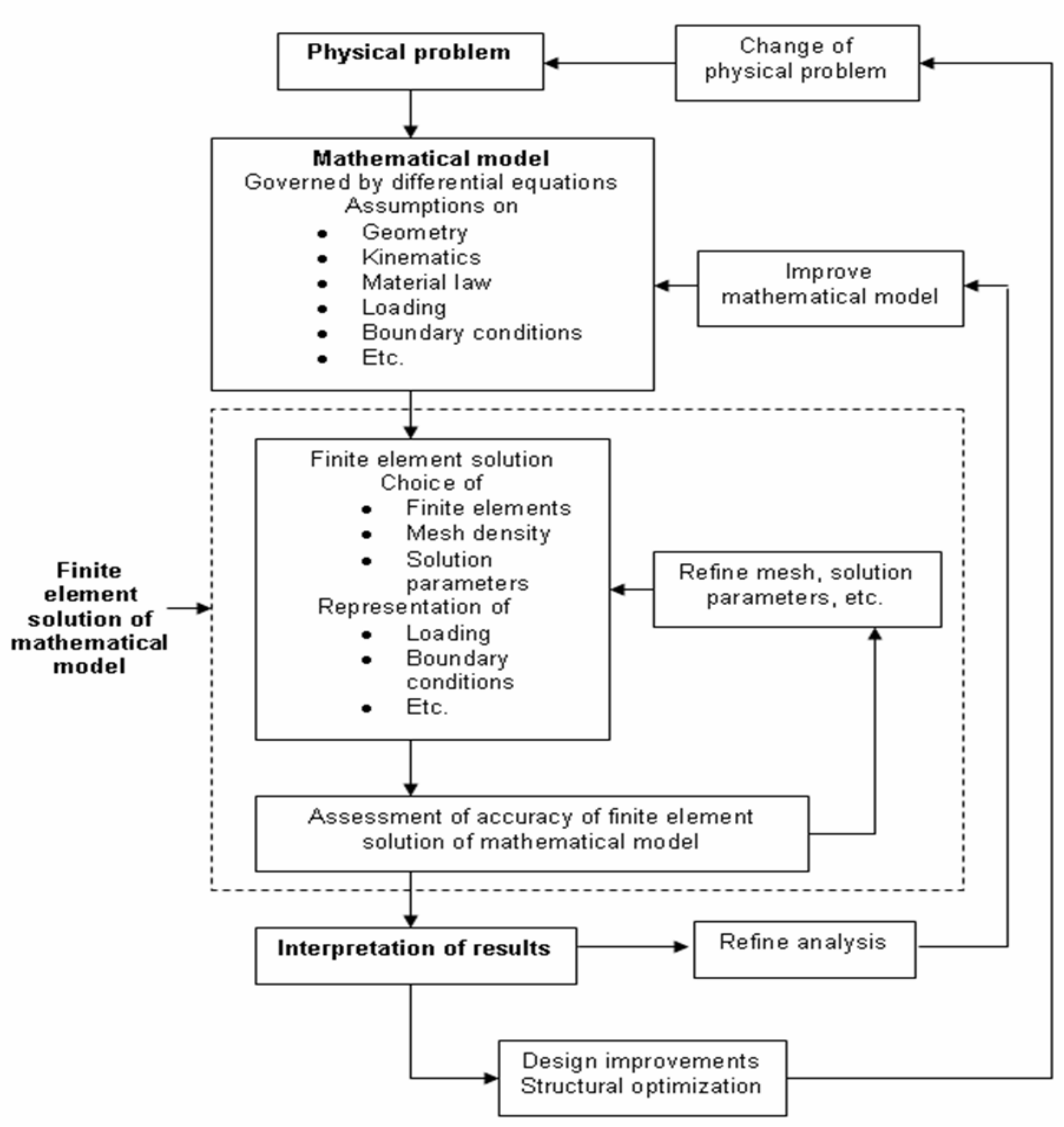

Figure 4.1: The summary of the process of finite element analysis [12]

4.2 Dynamic Nonlinear Process in Finite Element Analysis [38]:

The solution of the nonlinear dynamic response of a finite element system is obtained by using the procedures like the incremental formulations, the iterative solution procedures and the time integration algorithms. The explicit central difference method is used in LS-DYNA to integrate the equations of movement [38].

At time t, the semi-discrete equation of motion is:

$$ma^n = P^n - F^n + H^n \quad \text{.................................} (4.1)$$

Where P^n is external and body force, H^n is hourglass resistance, F^n is stress divergence vector m is diagonal mass matrix. To advance to time t^{n+1} the central difference time integration shows below:

$$a^n = m^{-1}\left(P^n - F^n + H^n\right)$$

$$v^{n+1/2} = v^{n-1/2} + a^n \Delta t^n \quad \text{.................................} (4.2)$$

$$u^{n+1} = u^n + v^{n+\frac{1}{2}} \Delta t^{n+\frac{1}{2}}$$

$$\Delta t^{n+1/2} = \frac{\left(\Delta t^n + \Delta t^{n+1/2}\right)}{2} \quad \text{.................................} (4.3)$$

Where v is the global nodal velocity and u is displacement vectors. By adding the displacement increments to the initial condition, the geometry is updated using following equation[13].

$$x^{n+1} = x^0 + u^{n+1} \quad \text{..} (4.4)$$

4.3 Equations of Frictional Force

Friction in LS-DYNA is based on a Coulomb formulation. The frictional algorithm uses the equivalent of an elastic plastic spring following these steps [13]:

1. Compute F_y:

$$F_y = \mu \left| f_n \right| \quad \text{................................} (4.5)$$

2. Incremental movement of slave node computation:

$$\Delta e = \mathrm{r}^{n+1}\left(\xi_c^{n+1}, \eta_c^{n+1}\right) \quad - \mathrm{r}^{n+1}\left(\xi_c^{n}, \eta_c^{n}\right)$$ …………….. (4.6)

3. Interface force update:

$$f^* = f^n - k\Delta e$$ ……………………… (4.7)

4. Yield condition check:

$$f^{n+1} = f^* \qquad \qquad if\ \left|f^*\right| \le F_y$$ …. ……… (4.8)

5. Trial force scale if possible:

$$f^{n+1} = \frac{F_y f^*}{\left|f^*\right|} \quad \text{if } \left|f^*\right| > F_y$$ ……… (4.9)

An exponential interpolation function is used to flat the transform between the static, μ_s and dynamic coefficient of friction μ_d:

$$\mu = \mu_d + \left(\mu_s - \mu_d\right) \quad e^{-c|v|}$$ ……… (4.10)

Where

$$v = \frac{\Delta e}{\Delta t}$$ ……… (4.11)

c is decay constant

Δt is time step size.

The interface shear stress that develops as a result of Coulomb friction can be very large and in some cases may exceed the ability of the material to carry such a stress, we therefore allow another limit to be placed on the value of the tangential force:

$$f^{n+1} = \min\left(f^{n+1}_{Coulomb}, \kappa A_{master} \right) \qquad \text{......... (4.12)}$$

Where A_{master} is the area of the master segment and k is the viscous coefficient. Since more than one node may contribute to shear stress of a segment, we recognize that the stress may still in some case exceed the limit k.

4.3 Energy Dissipation and Heat Transfer

Steady state or transient temperature field on three-dimensional geometries can be solved using LS-DYNA. Temperature dependent material properties can be used. It can also be either isotropic or orthotropic. The implementation of heat conduction into LS-DYNA is based on the work of Shapiro[1985].[39]

The differential equations of conduction of heat in a three-dimensional continuum is given by:

$$\rho c_p \frac{\partial \theta}{\partial t} = \left(k_{ij} \theta_{,j} \right)_{,i} + Q, \qquad \text{......... (4.13)}$$

Subject to the boundary conditions

$$\begin{aligned} \theta &= \theta_s && \text{on } \Gamma_1 \\ k_{ij}\theta_{,j} n_i + \beta\theta &= \gamma && \text{on } \Gamma_2 \end{aligned} \qquad \text{......... (4.14)}$$

And initial conditions at t_0:

$$\theta_\Gamma = \theta_0(x_i) \ \textbf{at} \ t{=}t_0 \, .$$

Where

$\theta = \theta\left(x_i, t\right)$ ……………… temperature

$x_i = x_i(t)$ ………………. coordinates as function time

$\rho = \rho(x_i)$ ………………. density

$c_p = c_p(x_i, \theta)$ ……………. specific heat

$Q = Q(x_i, \theta)$ …… internal heat generation rate per unit Ω

$k_{ij} = k_{ij}(x_i, \theta)$ ………..…..... Thermal conductivity

θ_Γ ……………….prescribed temperature on Γ_1

n_i ....normal vector to Γ_2

These equations above represent the strong form of a boundary value problem to be solved for the temperature field within the solid.

The finite element method provides the following equations for the numerical solutions of equations

$$\left[\frac{C_{n+\alpha}}{\Delta t} + \alpha H_{n+\alpha}\right]\left\{\theta_{n+1} - \theta_n\right\} = \left\{F_{n+\alpha} - H_{n+\alpha}\theta_n\right\} \qquad \text{…… (4.15)}$$

Where

$$\left[C\right] = \sum_e \left[C_{ij}^e\right] = \sum_e \int_{\Omega^e} N_i \ \rho c \ N_j d\Omega \qquad \text{…… (4.16)}$$

$$\left[H\right] = \sum_e \left[H_{ij}^e\right] = \sum_e \left[\int_{\Omega^e} \nabla^T N_i K \nabla N_j d\Omega + \int_{\Gamma^e} N_i \beta N_j d\Gamma\right] \qquad \text{…… (4.17)}$$

$$[F]=\sum_{e}\left[F_i^e\right]=\sum_{e}\left[\int_{\Omega^e} N_i q_g \, d\Omega+\int_{\Gamma^e} N_i \gamma \, d\Gamma\right] \qquad \text{...... (4.18)}$$

The parameter α is taken to be in the interval [0,1]. Some well know members of this α -family are [13]:

α	<u>method</u>
0	forward difference; forward Euler
1/2	midpoint rule; Crank-Nicolson
2/3	Galerkin
1	backward difference, fully implicit

Analytically, we use the following expression in order to calculate heat generation; this is a formula in LS-DYNA theoretical manual to calculate the heat generation on the crack sides, which matches the physical process well in our experimental settings. Thermal energy around the crack areas are the accumulative results from this heat generation.

$$Q\,(t)=\sum_{j=0}^{t/\delta t}\ \sum_{i=1}^{N}\{\mu_d+(\mu_s-\mu_d)\ e^{-c\left|V_i(t_j)\right|}\}\ F_i(t_j)\ V_i(t_j)\ \delta A_i \qquad \text{.................................. (4.19)}$$

where,

Q (t) = heat generated in ith element.

μ_d = coefficient of dynamic friction=0.4

μ_s = coefficient of static friction=0.35

$V_i(t_j)$ =Relative velocity between corresponding nodes

C= exponential decay coefficient (10 s/m).

$F_i(t_j)$ = Average normal force.

Ai = area of the ith element.

4.4 FEA analysis on Al bar and coupling materials in the Al bar system

The model is made of 3-dimensional solid elements, shown as green for the component number 1. The cylindrical object, shown as gray, is the rigid ultrasonic transducer (number 3), it provides a sinusoidal 20kHz vibration with amplitude 0.016mm, the direction of this sinusoidal motion is normal to the sample. The light blue rectangular object is the rigid post behind the sample, and the right part of sample is constrained of 6-degree freedom (u, v, w, θ_x, θ_y & θ_z) to represent experimental conditions where that part of the sample are fixed by a clamp and a support. The model is meshed and preprocessed in Hypermesh.[35-36]. The sample material in this model is isotropic elastic material (the material #1 in LS-DYNA software package). The properties of this material such as density, elastic modulus, thermal conductivity, etc are applied according to the Aluminum alloy 2024-T351. The material type of the cylinder and the support are rigid material (the material #20 in LS-DYNA software package, as shown in Table4.2

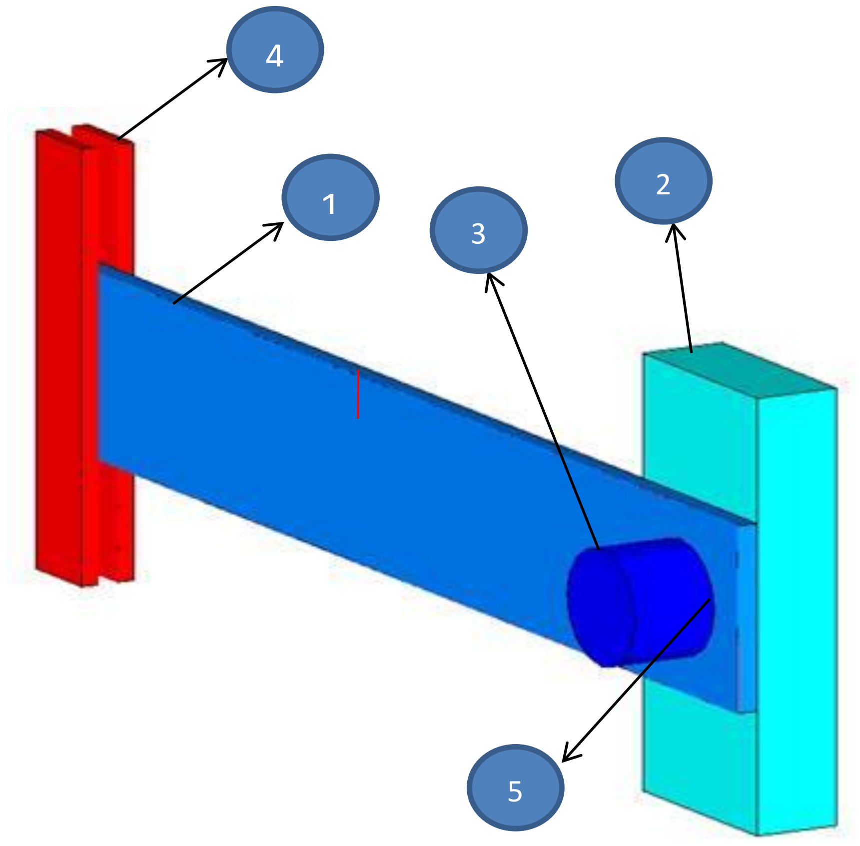

number	Description
1	150mm*24mm*2.5mm
2	Right side backed by rigid post
3	Rigid Transducer of L=10mm Φ=15mm
4	Left Hand side constrained 6-degree freedom
5	Input vibration at 20kHz,Amplitude=16μm Equilibrium separation between bar and cylinder=14 μm

Figure 4.2 Description of the components in the model

Material	**2024-T351 aluminum alloys**
Density	**2780 kg/m3**
Modulus	**73.1 GPa**
Poisson ratio	**0.33**
Dynamic coefficient of friction	**0.35**
Static coefficient of friction	**0.4**
Thermal conductivity	**121 w/m-k**
Specific heat	**875 J/Kg.C**

Table4.1 Material properties used in the model

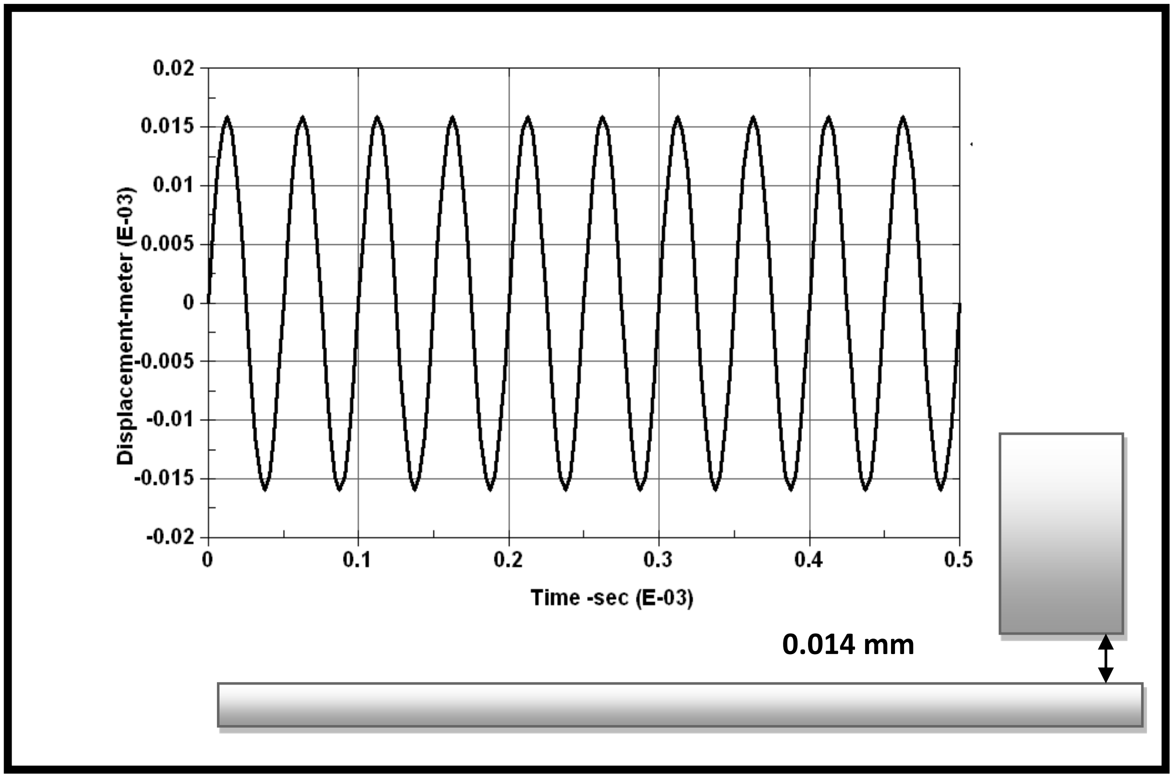

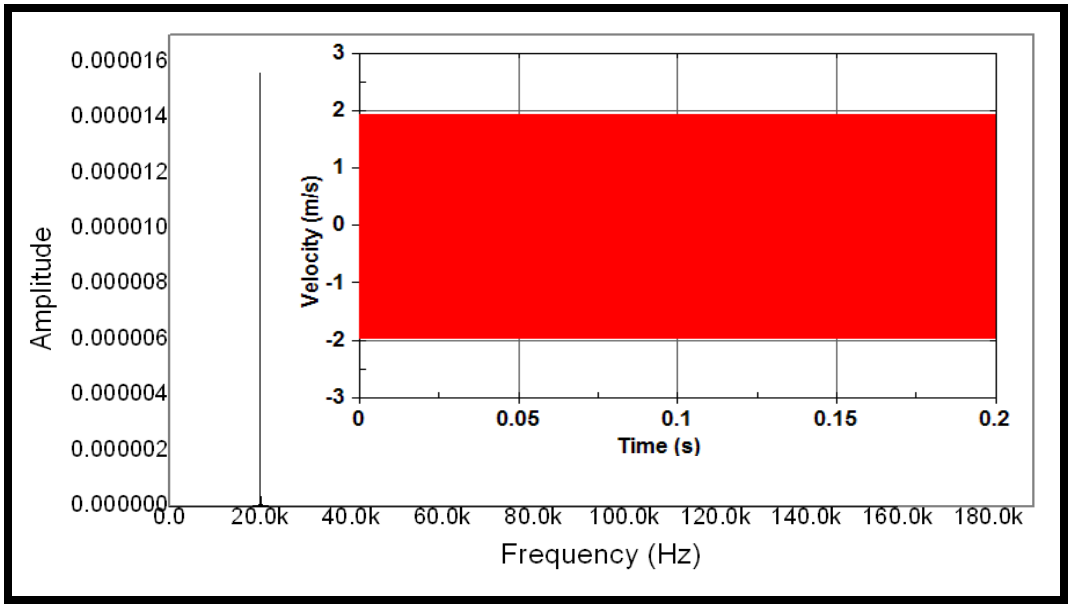

Fig.4.3 vibration Input in the model

4.4.1 Plastic deformation check

Before the simulation, we can do a simple mathematic analysis for the sample using the basic physical concept to dig out whether the initial condition follows the basic physical rules. More important thing is, we need to know under the simulation boundary condition, there is no plastic deformation in the sample, which is a destructive evaluation to the sample. In our experiment, there also is no plastic deformation in the sample.

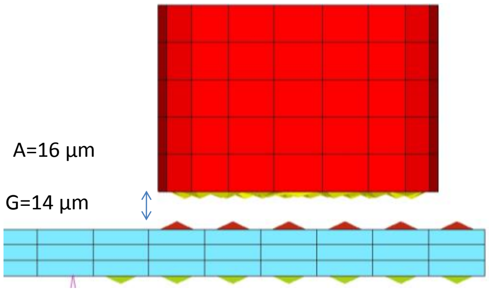

Fig.4.4 illustration of the initial contact condition of the gun and the sample

$$x = A \cdot \sin(\omega t + \alpha)$$ ……………………gun displacement

$$v = A\omega \cdot \cos(\omega t + \alpha)$$ ……………..gun velocity

$$a = -A\omega^2 \cdot \sin(\omega t + \alpha)$$ …………..acceleration of the gun

F=ma…………………………gun force added to the sample………..(4.20)

Fig.4.4 shows the information about the initial condition of the sample and the gun, here A=16 µm, means the amplitude of the gun is 16 µm, while G=14 µm means the initial gap between sample and gun is 14 µm .Using the formula above, we can input A=16µm, ω=2*pi*20000.

Then we get some initial analytical results as shown from Fig.4.5 to Fig.4.7:

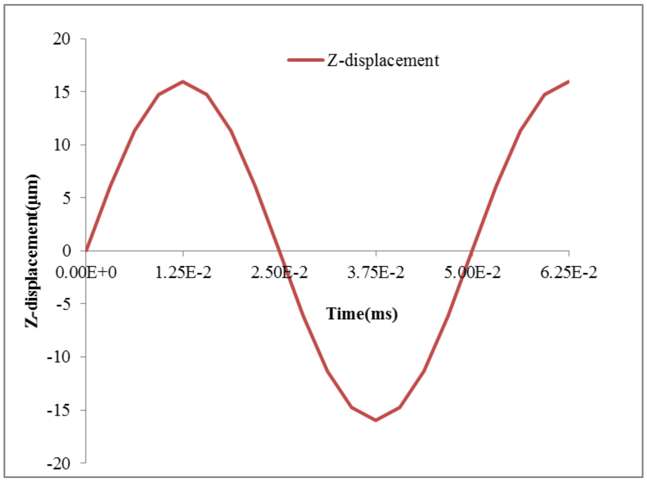

Fig.4.5 gun displacement input in the anlysis

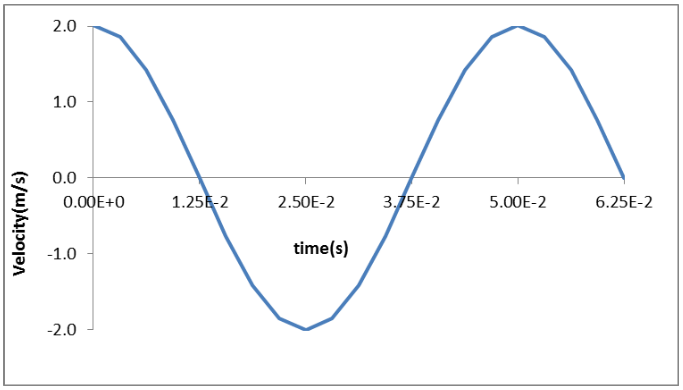

Fig.4.6 gun velocity analytically calculated from formula 4.2

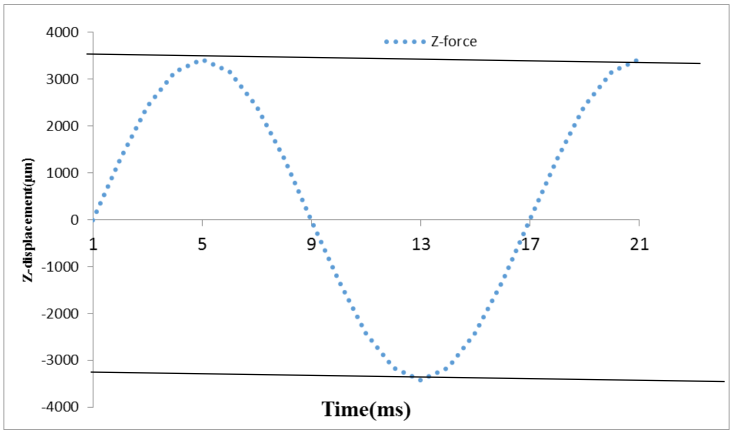

Fig.4.7 gun force calculated analytically

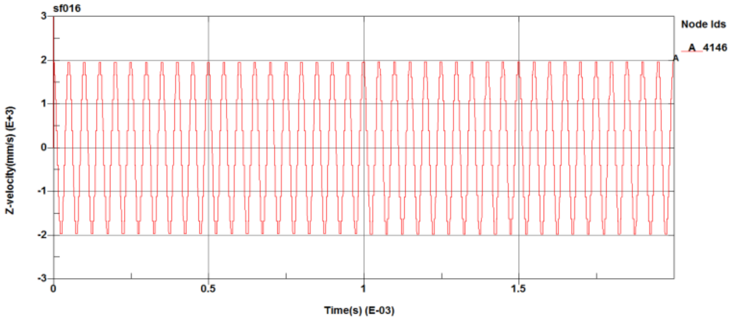

Fig.4.8 gun velocity output from FEA

Fig.4.5 shows the analytic results calculated using the formula 4.20, we can see the maximum the maximum z-displacement is 16um; while Fig.4.6 shows the maximum gun velocity is 2m/s, Fig. 4.7 shows the maximum force is about 3500N. At the same condition, we double checked our model by using LS-DYNA. By using the same gun displacement as input for boundary condition, we can get the same velocity output from the gun tip as the analytical results. From another point, we can also see that when the gun first touch the sample, it is in the time period of 34.4μs to 40.6μs. At this time period the maximum force added to the sample is about 3426N, if we use the young's module of the sample as 73.1G, using the formula in Fig.4.9, we can get the deformation of the sample is about 0.183 μm,

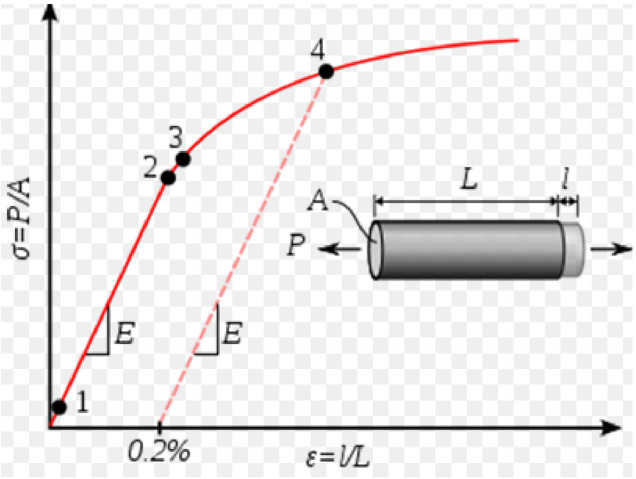

Fig.4.9 mechanical deformation of materials

According to the materials properties, the maximum stress is about 72MPa, which is all the way under the yield stress of the sample at 324Mpa. So we can say it is safe to define the material as elastic material, and it is on the track of NDE technique.

In addition to the analytical deformation check, the maximum vM stress is also checked in the sample, with or without coupling materials. Fig.4.10 shows the v-M stress contour of the bar under vibration, in the time of 0.165s, the maximum v-M stress is about 70MPa, which is all the way below the plastic yield stress, according to industrial standard which is 324MPa.

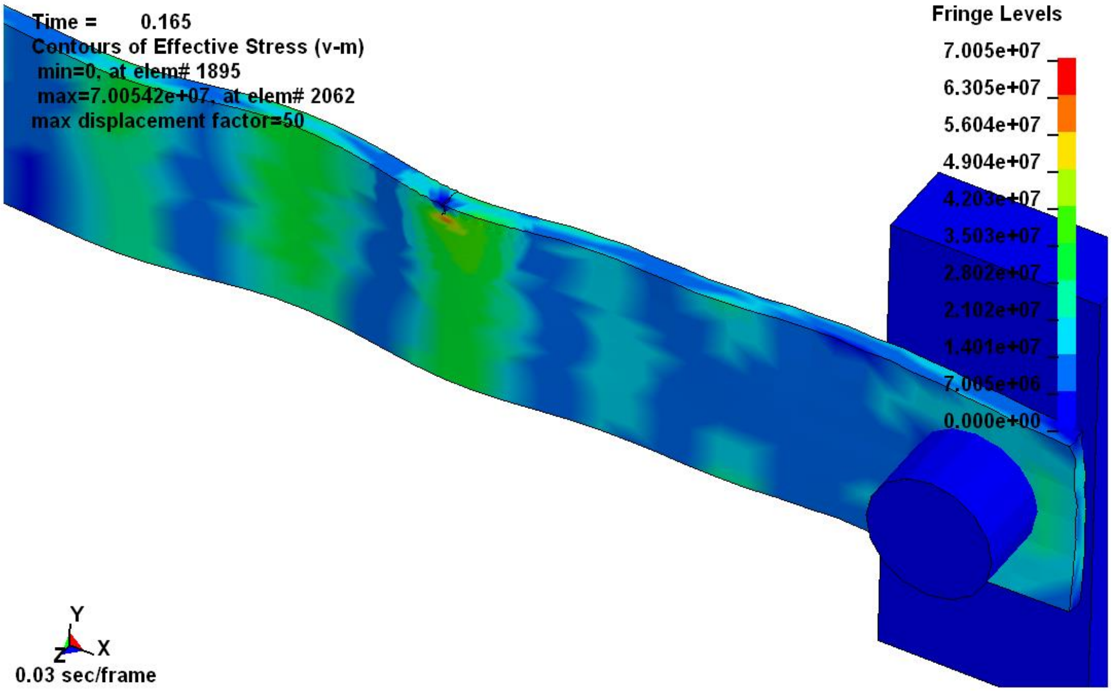

Fig.4. 10 V-M stress contour of the bar

4.1.2 Influence of distance between transducer and sample to the T-t plot

For the initial calculation, we did not put any coupling materials between transducer and sample, only changing the distance of this two, to see how the temperature increase differs. The gap between the transducer and the sample are picked for several variables from 0 to 16μm.

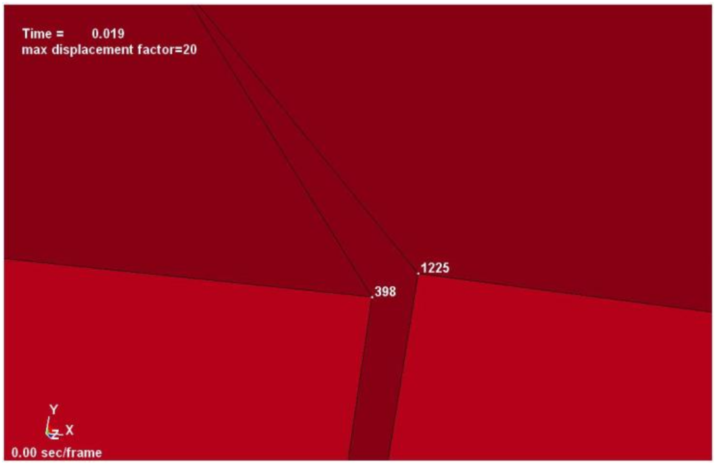

Figure 4.11 Node definitions at the crack

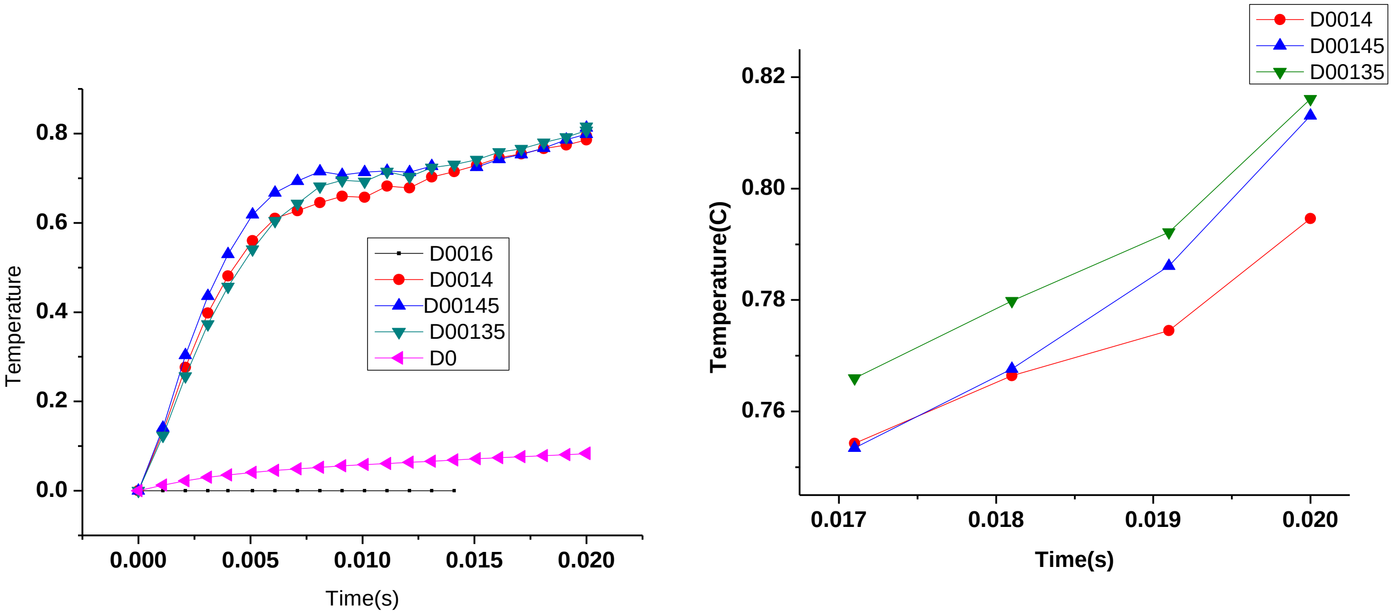

Figure4.12 T-t plot for different distance at node 1225

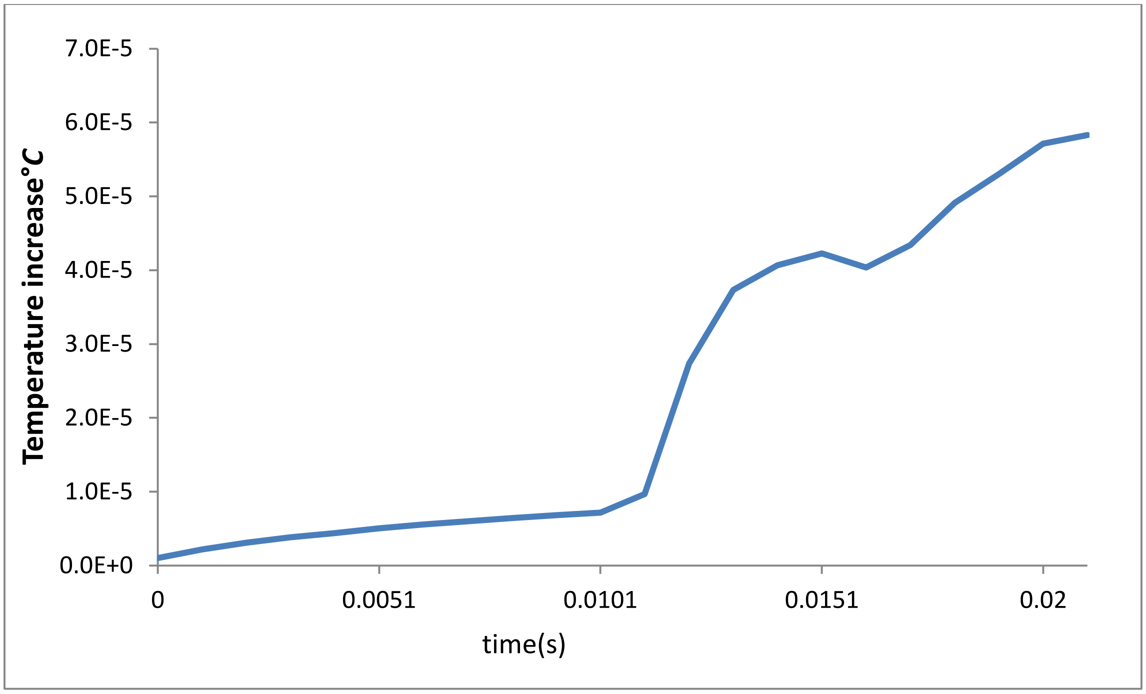

Figure4.13 zoomed in view for T-t plot for distance at node 1225

A (µm)	**D(µm)**	**Temperature increase(°C)**
16	0	0.12
16	13.5	0.81
16	14	0.78
16	14.5	0.805
16	16	6e-5

Table 4.2 Variable distance for D as parameter and the temperature increase

Fig.4.11 and Fig.4.13 show the result of T-t plot curve at node 1225 for different distance varies from 0 to 16μm, From above we can see that when d=13.5μm the temperature increase is the highest, while when d=16μm, when the transducer barely touch the sample, the temperature increase is the lowest, as summarized on Table.4.2.

4.4.2 Chaos and Non-Chaos

In order to see the difference of the chaos and nonchaos in the simulation. Two simulations are done here, one is for the case of chaos, and another case is for nonchaos. For the chaos model, the simulation is divided into two steps: at step one, the time period for the transducer touch the sample is 10ms, the vibration is added on the transducer; at step two, the vibration is removed from the transducer, and the heat diffusion around the crack area is observed. For the non-chaos model, only one step is done, the transducer is removed; while the vibration is added to the other end of the sample, other boundary conditions are the same with chaos model.

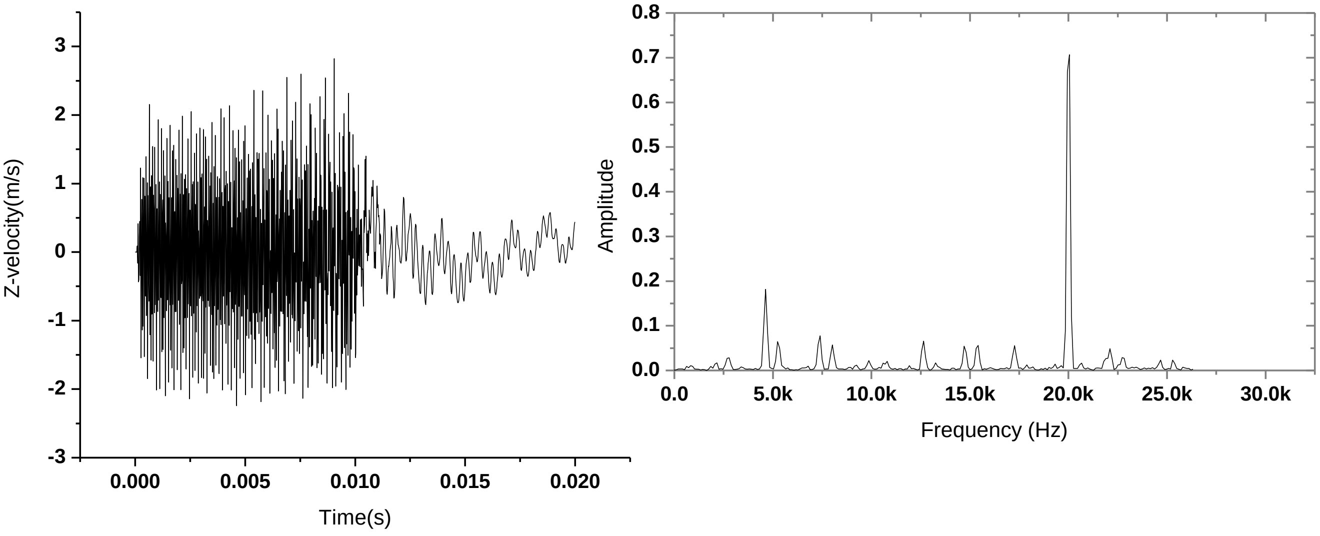

Fig.4.14 velocity and its fft for the node at edge crack node 1225 when D=13. 5μm

Fig.4.14 shows the result of the velocity and its fft for the node at edge crack node 1225 when D=13.5μm. From the FFT curve, we can see that it is chaos.

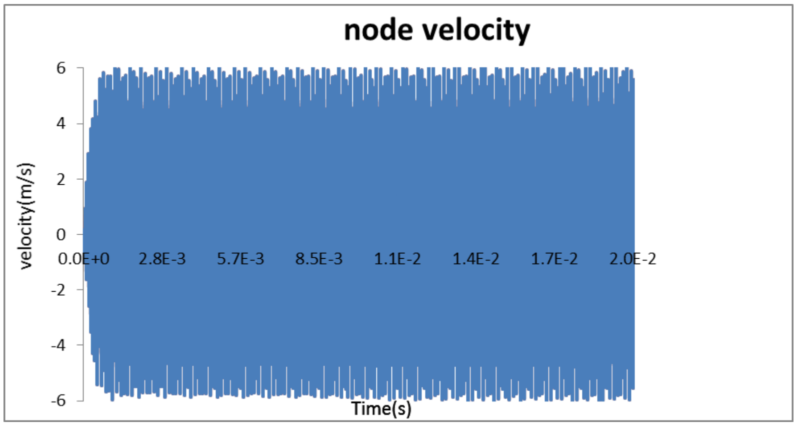

Fig.4.15 velocity curve for the nonchaos case for node 1225 when D=13.5μm

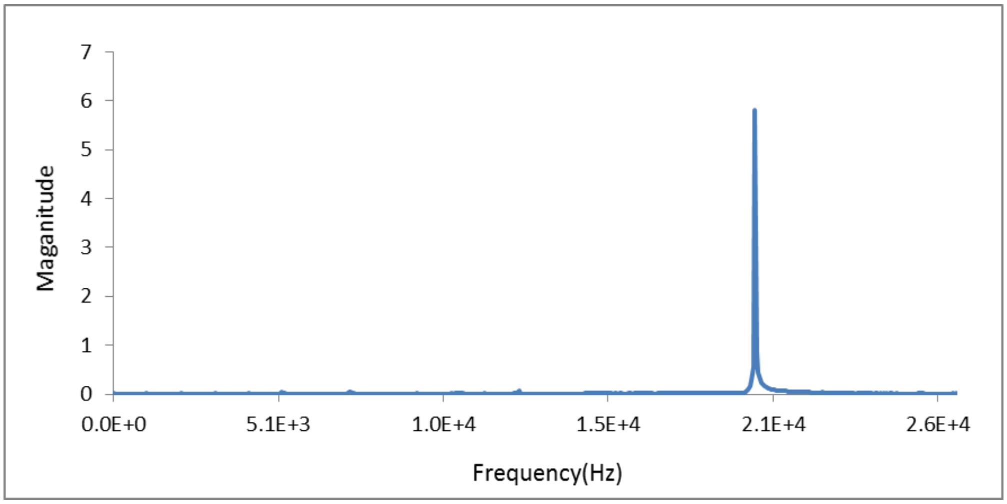

Fig.4.16 FFT of fig. 4.15

Fig.4.15 shows the velocity curve for the nonchaos case for the node 1225, Following is the FFT transform of its velocity. It is pure harmonic. While at the same time, we can compare the T-t curve for the node temperature increase. From Fig.4.17 we can see that the temperature increase is higher at chaos than that of nonchaos model.

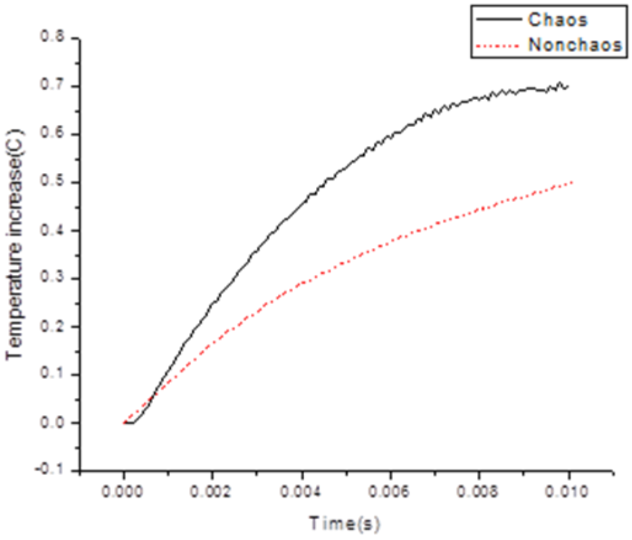

Fig.4.17 temperature curve comparison of chaos and nonchaos

4.4.3 Influence of impulse frequency on the temperature increase

The influence of impulse frequency on the temperature increase is researched by Wei in his PhD thesis, it showed good trend on the temperature increase related with frequency. Four different input frequencies, 20kHz, 30kHz, 40kHz, and 50kHz, were selected for this study. Those frequency components are very common in the spectra obtained from experiments. Four waveforms are displayed in Figure 4.18.

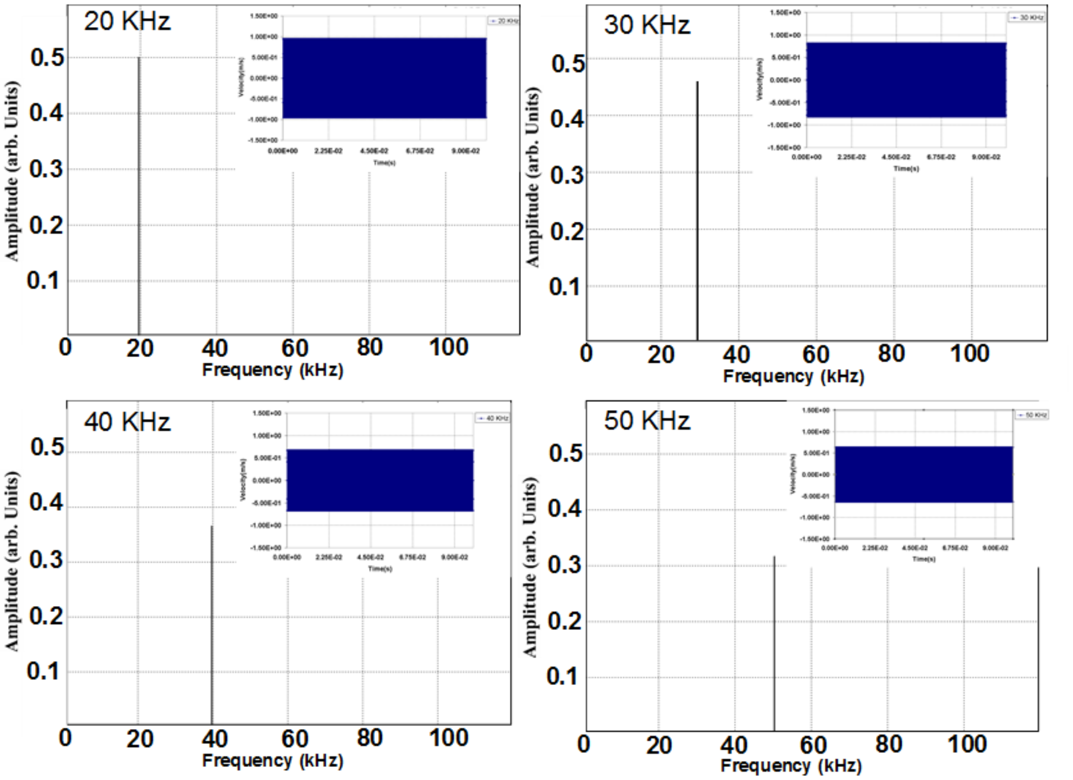

Figure 4.18: Four different input frequencies used in the FEA simulation.

The energy of an input pulse can be expressed as:

$$E = \frac{1}{2} \times A^2 \times 2\pi f \ ,$$

where E is energy, A is the amplitude of an input pulse, f is vibration frequency.

To make the power of the four input pulses the same, the amplitude of 20kHz input is set to be 1, the amplitude of 30 KHz is set to be $\sqrt{2/3} = 0.8165$, the amplitude of 40kHz is set to be $\sqrt{2/4} = 0.707$, and the amplitude of 50kHz is set to be $\sqrt{2/5} = 0.6325$. The amplitudes for the four frequencies are displayed in Figure 4.19. The total duration of calculation is set to be 200 ms in order to display the temperature drop down.

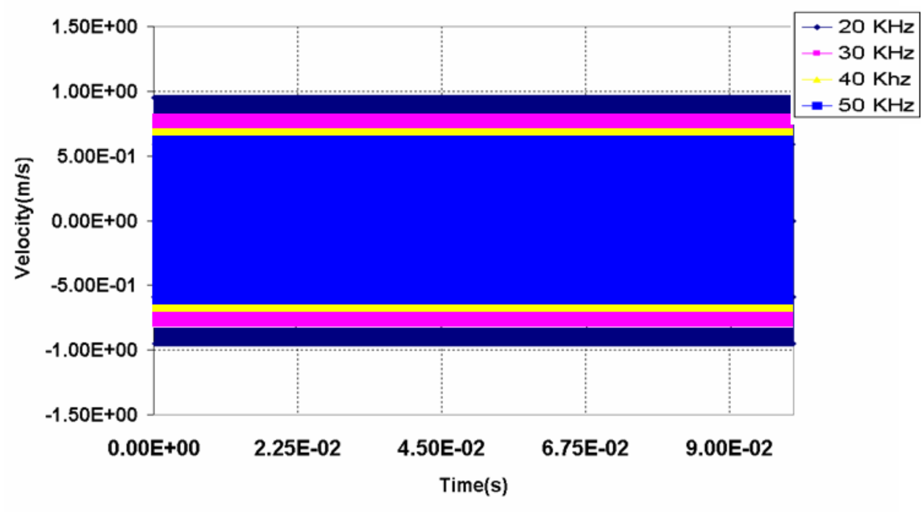

Figure 4.19: Amplitude comparison of the four different input frequencies.

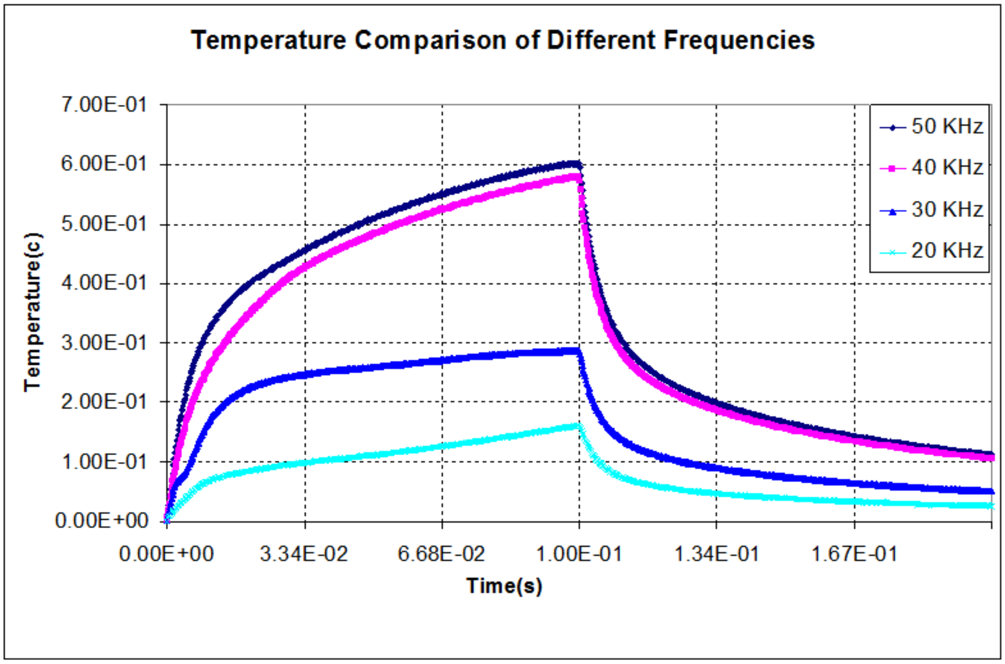

Figure 4.20: Temperature increase of the four different input frequencies [40]

4.4.4 Influence of acoustic impedance of coupling materials on the temperature increase

The difference of acoustic impedance(usually called impedance mismatch) between two sides of the media will has strong effect to the acoustic energy transmitted [23, 24]. The increase of the difference will increase the percentage of energy travelling. The reflection coefficient can be calculated using such formula based on the known impedance of the media in two sides [24].

$$R = \left(\frac{(v1 * d1 - v2 * d2)}{(v1 * d1 + v2 * d2)}\right)^2 \tag{4.21}$$

The transmission coefficient can be obtained by subtracting the reflection coefficient from 1 since the total transmission coefficient and reflection coefficient are equal to one. Here the v1 is the velocity of the sound at media 1, which is a function of young’s modules density of the media 1, and d1 is the density of media 1 (coupling materials); v2 is the velocity of the sound at media 2, which is a function of young’s modules density of the media 2， and d2 is the density of media 2 (Al bar), as shown in Fig.4.21.

Fig.4.21 shows the schematic drawing on travelling of the ultrasound through different material used in our system. The acoustic impedance between coupling material and our Al bar sample are obvious different. When the sound travel through these two media, there must be ultrasound reflection from them, only the transmitted ultrasound will be the effective input to vibrate the Al bar sample. As we all know, that the acoustic impedance is related with the density (d) of the material and the sound speed (v) in it. Using the expression (3), we can get the reflection coefficient of the ultrasound. Correspondingly, we can also get the transmission coefficient of the ultrasound in our system. At Fig.11, the transmission coefficient of different coupling materials used in our system is plotted by using the properties from table 1. It is obvious that the trend of the transmission coefficient of coupling material following the same trend as the “thermal energy” and “acoustic energy” calculated from the crack site, from the highest to the lowest for the six coupling materials as: 2LayerDT, LamBC, Teflon, NonLamBC, GasketMaterial, and Leather. This is the inherent reasons for the difference between these coupling materials.

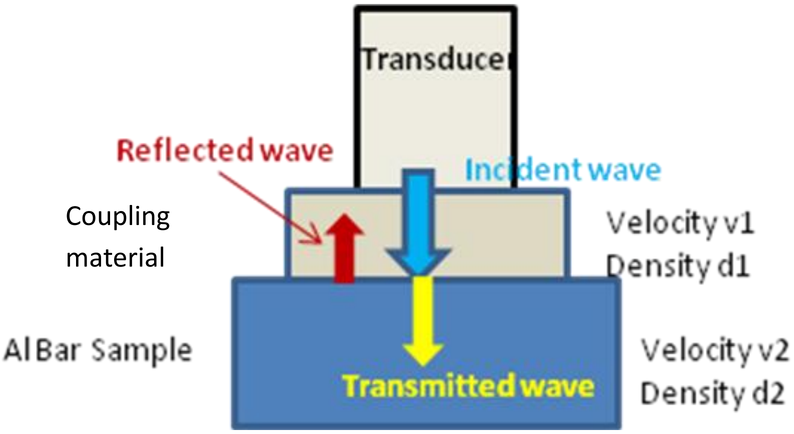

Fig.4.21 Acoustic impedance and refelection coefficient

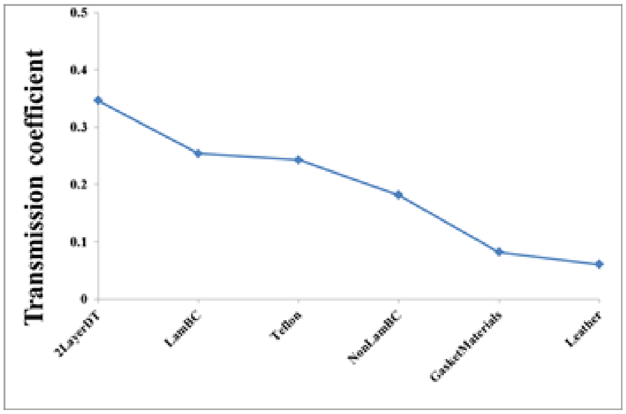

Figure 4.22 Transmission coefficient of each coupling material

	density(g/cm3)	young's modules(MPa)	Transmission coefficient
Al sample	2.7	73000	
2LayerDT	1.1	2000	0.35
LamBC	1.5	700	0.25
Teflon	2.1	450	0.24
NonLamBC	0.7	700	0.18
GasketMaterials	0.9	100	0.08
Leather	0.6	80	0.06

Table 4.3 Transmission coefficient of each coupling material

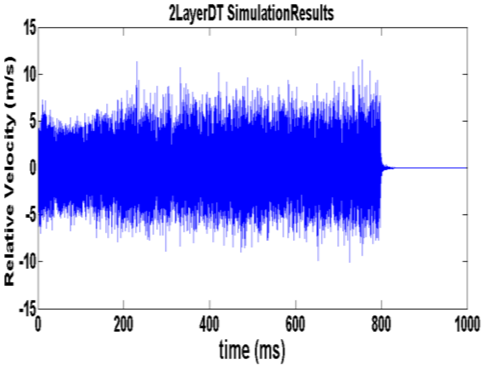

Fig.4.23a Waveforms results from FEA analysis at crack for 2LayerDT as coupling material

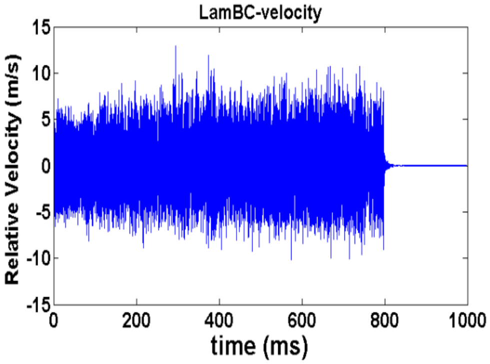

Fig. 4.23b Waveforms results from FEA analysis at crack for LamBC as coupling material

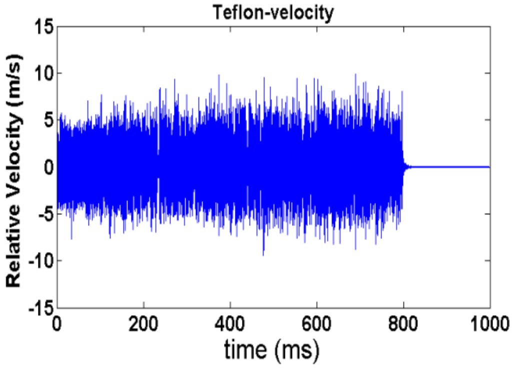

Fig. 4.23c Waveforms results from FEA analysis at crack for Teflon as coupling material

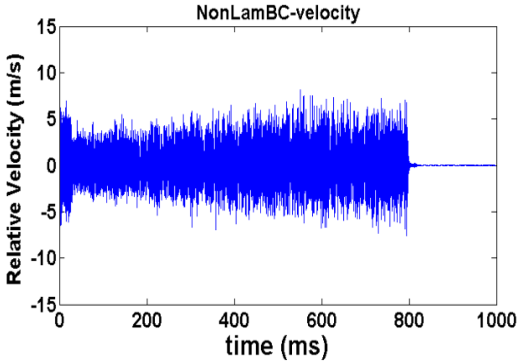

Fig. 4.23d Waveforms results from FEA analysis at crack for NonLamBC as coupling material

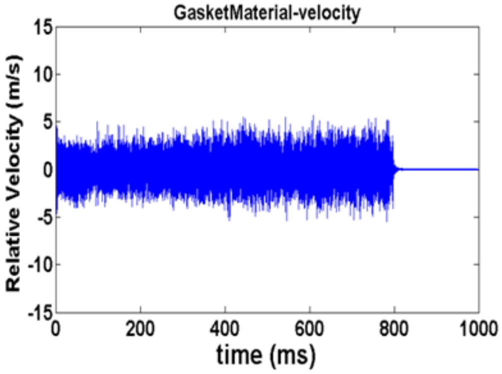

Fig. 4.23e Waveforms results from FEA analysis at crack for GasketMaterial as coupling material

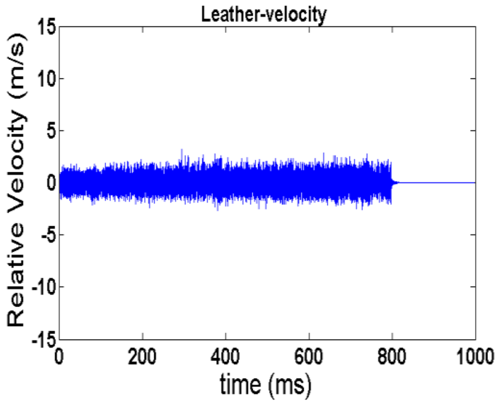

Fig. 4.23f Waveforms results from FEA analysis at crack for Leather as coupling material

Fig. 4.23 Waveforms results from FEA analysis at crack for the six coupling materials: a)2LayerDT, b)LamBC, c)Teflon, d)NonLamBC, e)GasketMaterial, and f) Leather

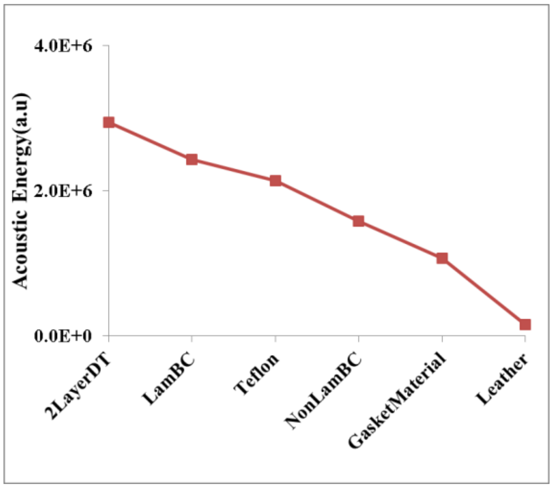

Fig. 4.24 “acoustic energy” calculated at one spot of the crack for the six coupling materials from FEA results

Fig.4.23 shows the velocity waveform get from the FEA analysis in the structural analysis part. The amplitude of the waveform shows the same trend as the test results from the highest to the lowest in the order of 2LayerDT, LamBC, Teflon, NonLamBC, GasketMaterial and Leather correspondingly. On the same time, by using the equation (2), we can get the “acoustic energy” for the crack nodes at the crack tip. According the method used for the calculation in the test part, the relative velocity is used in the calculation again in the model. From Fig.4.24, we can also see the similar trend for the "acoustic energy" on crack tip by variation of these six coupling materials.

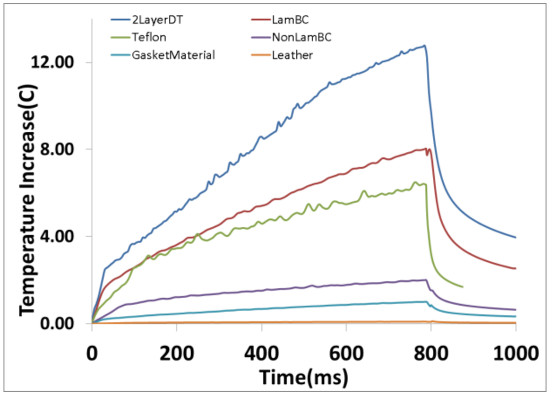

Fig. 4.25 Temperature - time plots at one crack node with the six coupling materials

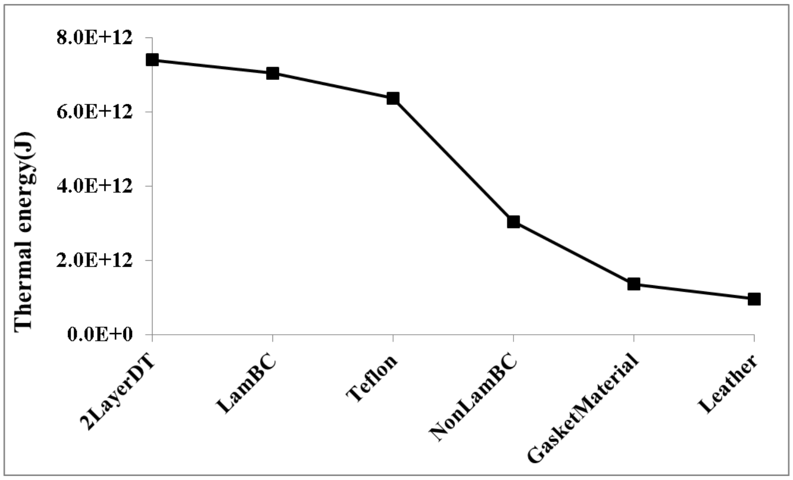

Fig. 4.26 Thermal energy at one crack node

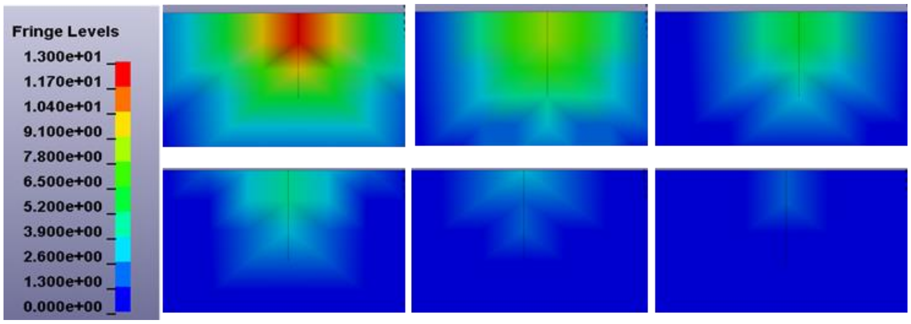

Fig. 4.27 Temperature contour at crack with the six coupling materials

Fig. 4.25 shows the temperature-time plot of the crack tip from the thermal analysis by using six different coupling materials. Here we can also see the same trend as temperature time curve from test from the highest to the lowest in the order of 2LayerDT, LamBC, Teflon, NonLamBC, GasketMaterial and Leather correspondingly. Similarly, from the thermal analysis in the first step, we can get the "thermal energy" calculated by summing up the energy at each step using following equation:

$$E(Q) = \sum_{t=0}^{t/\delta t} Q(t) \tag{4.22}$$

Fig. 4.26 shows the "thermal energy" calculated by using equation(4.22), here we can also get the similar trend as "thermal energy" calculated from the test side. Also, the temperature contour is captured for each of these casesa at the highest temperature increase time from highest temperature increase to lowest temperature increase for these six coupling material as shown in Fig.4.27. This results is highly coninsistant with our test resutls.

CHAPTER FIVE

CONCLUSION AND FUTURE WORK

CONCLUSION

The most important task of my thesis is quantitatively analyzing coupling materials in SonicIR system and the major conclusions are:

- Coupling materials play very important role in the SonicIR system; there is a series of parameter to influence the detectability of the SonicIR technique related to the coupling materials, such as loading force, loading sequence, coupling materials and driving frequency. Different coupling materials ,different force or different driving frequency will give different results on SonicIR system.
- The effect of coupling materials is obvious nonlinear. For the common used coupling materials, the acoustic energy and thermal energy quantitatively calculated has the order from the highest to the lowest in the order of 2LayerDT, LamBC, Teflon, NonLamBC, GasketMaterial and Leather correspondingly. For all these coupling materials in 20KHz system, chaos are the common characteristic on the waveform. Among them, 2LayerDT is the best coupling material, because it has the highest acoustic transmission coefficient to the AL bar sample. The impedance mismatch between coupling material and Al bar sample is the key factor to effect the vibration and thermal image on the sample.

- The effect of loading force is also obvious nonlinear. Increase the loading force to the system, will increase the output of acoustic energy and thermal energy. But there is limitation for the increase, for 2LayerDT as coupling material, overload will happen when the load is 192N, further increase the loading force will reduce the output from the acoustic energy and thermal energy. This limitation is related to the maximum power output the power supply can have.
- The effect of driving frequency is significant. For the common used power supply system in our lab, among 20KHz, 30KHz and 40KHz, 20KHz is better than 30KHz, and 30KHz is better than 40KHz. Also, 20KHz produces chaos to the system, while others are all harmonic. The reason behind the phenomena is the 20KHz power supply has higher power than 30KHz, while the power or 30KHz is higher than 40KHz.
- From simulation results, we can see there are also couples of results interesting. One thing clear is from V-Miss stress calculation, the samples are all in the safe zone, and this technique is real Non-Destructive. From simulation, we verified with experimental results that chaos is better than non-chaos. In order to get chaos we'd better give a tiny gap between gun and sample, the gap also influence the results, from simulation results, we see that the gap of 13.5µm is the best one for the amplitude of 16µm
- By input the different impedance of the coupling materials to the FEA model, the acoustic energy and thermal energy from crack tip output can get close match to the experimental results, which further proves that the impedance mismatch

between coupling materials and al bar sample are the key factor for the nonlinear phenomena.

- These nonlinear phenomena is further proved by change the target AL bar sample to Al fan disk sample, the nonlinear effect of coupling effect including coupling materials, loading force and driving frequency are obviously same with the case study on Al bar sample.

FUTURE WORK

1. Chaos research on experimental

It is validated in simulation that chaos will increase the temperature of the crack area comparing to non-chaos situation. So the goal of the experiment should be to produce chaos for the system. Since chaos are a state of disorder, it is not easy to catch it, but it is very important to the experiment, there should be more research on chaos, how it generated and how to repeat it, and how to improve it in the system. For coupling materials, it should be more data on it, basically make the experimental results more repeatable. One or more coupling method should be follow for better chaos generation, to increase the detectbility of the crack.

2. Coupling materials research on different target structure

The results from the thesis are focused on Al structure only, but if the target structure is different, the nonlinear effect of the coupling material will be different also. For future reference, the research on the effect of coupling materials for different structure such as composite, blades should be conducted. Also, the frequency system should be broader, not only limited on these three driving frequency. If possible, using sweeping frequency system to investigate the difference is another interesting project.

3. Composite Simulation

Due to the heavy usage of composite in aerospace industry, the NDE analysis is more critical for this industry. For the predictive analysis, it is quite important to simulate the heat generation and thermal conduction behavior for composite with defects and delamination. But, composite model development is quite challenging due to the anisotropic and non-linear properties. It will be another interesting project to simulate the non-linear effect of the coupling materials on composite structure. For future reference, the initiative step for this research should be conducted on the composite plates or composite bar. After that, complicated geometry can be introduced.

4. Turbine Disk Simulation

In aerospace and energy industry, turbine disk also has broad applications. The NDE analysis plays significant important role for the industry. The most challenging part of the simulation comes from the complex geometry. How to build up the model with cracks, how to simulate the friction between them are also critical for the development of the technology in this industry.

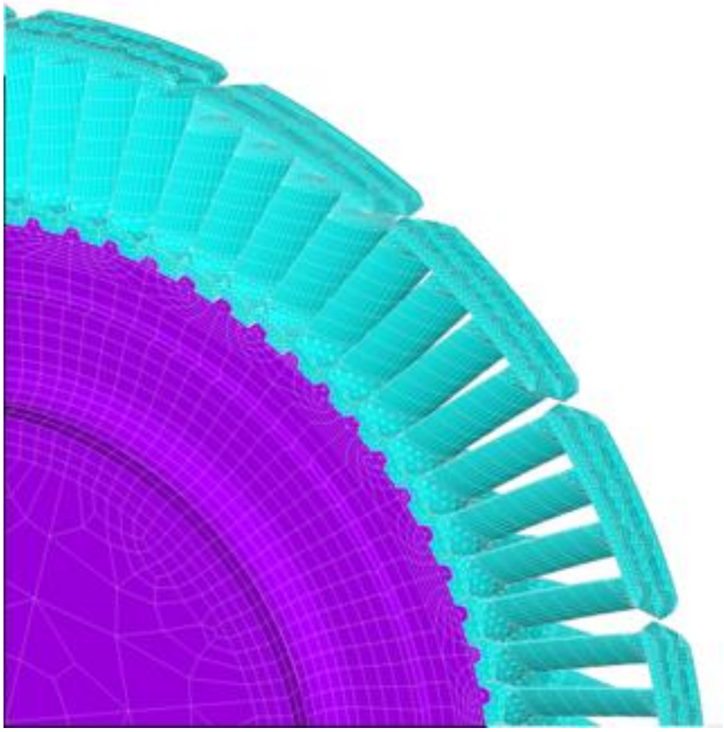

Fig.5.1 Turbine Disk meshed FEA model

REFERENCES

1. http://en.wikipedia.org/wiki/Nondestructive_testing
2. http://www.as.wm.edu/Nondestructive.html
3. Baldev Raj, C.V. Subramanian, T. Jayakumar, *Non-destructive Testing of Welds*, 2000.
4. http://www.cinde.ca/ndt.shtml
5. Xiaoyan Han, L. D. F., Zhong Ouyang, Gang Sun,Hua Sui, and R.L.Thomas (2000). Rev.Sci.Inst. 71: 2418.
6. Xiaoyan Han, L. D. F., Zhong Ouyang, and R.L Thoms, (2001). Journal of Adhension 76: 151.
7. L.D.Favro, R. L. T., X. Han, Zhong Ouyang, G.Newaz, and D.Gentile (2001). Int.Journal of Fatigue 23: S471.
8. Xiaoyan Han, L. D. F., Zhong Ouyang, and R.L Thoms, (2002). Review of Quantitative Nondestructive Evaluation 21: 552.
9. Xiaoyan Han, L. D. F., and R.L Thoms, (2003). Review of Quantitative Nondestructive Evaluation 22: 500
10. A.Bulavinov,M.Dalichow,M..Kroning,J.H.Kurz,F.WalteandK.Reddy (2006),Quantitative Ultrasonic Testing of Pressurized Components Using Sampling Phased Array,NDE2006
11. Xiaoyan Han, Sonic Infrared Imaging: A novel NDE Technology for Detection of Crack/Delamination/Disbond in Materials and Structures, Development in Ultrasonic and Advanced Methods in NDT, edited by C.H. Chen, World Scientific Publishing. July, 2007.

12. Jianping Lu, Xiaoyan Han, G. Newaz, L.D. Favro, R.L. Thomas, Study of the Effect of Crack Closure in Sonic Infrared Imaging, Journal of Nondestructive Testing and Evaluation, Special Issue on Thermographic Techniques and Results in Nondestructive Testing and Evaluation, 127-135, September, 2007

13. Xiaoyan Han, Rui Yu, Studying the Effect of Coupling Materials in Sonic IR Imaging, SPIE, Smart Structures and Materials 2007, Vol. 6529, pp 652937-1-6, 2007

14. Xiaoyan Han, Qi He, Nebojsa Sebastijanovic, Tianwei Mac, Henry T.Y. Yang, Developing Hybrid Structural Health Monitoring Via Integrated Global Sensing And Local Infrared Imaging , SPIE, *Smart Structures and Materials 2007*, Vol. 6529, pp 65291E-1-6, 2007

15. Marc Dubois, Tony Dunhill, Dong Fei, Xiaoyan Han, Tammana Jayakumar, Anton Lavrentyev, Eric Lindgren, Katy Milne (Alphabetic order), *Perspectives in NDE Education*, AIP, *Review of Progress in Quantitative Nondestructive Evaluation*, Vol. 27, pp 1802-1825, 2008

16. Xiaoyan Han, W. L., Zhi Zeng, L.D.Favro, and R.L Thoms, (2002). Applied Physics Letters 81: 3188.

17. Indigo Systems, *Phoenix Camera System User's Guide.*

18. BRANSON Ultrasonic Corp., *2000t Power Supply Instruction Manual. 2000*

19. Polytec, *Polytec Vibrometer Software:* Theory manual.

20. Polytec, *Laser Doppler Vibrometer,* User manual.

21. Sandeep Degala, Piervincenzo Rizzo,Karthik Ramanathan and Kent A.Harries(2008),Acoustic Emission monitoring of CFRP reinforced concrete slabs,Construction and Building Materials

22. Xiaoyan Han, Z. Z., Md.Sarwar Islam,Wei Li, Jianping Lu,Vera Loggins, E.Yitamben, L.D.Favro,G.M.Newaz, and R.L Thoms, (2004). J.Appl.Phys. 95: 3792.
23. Xiaoyan Han, J. L., Md.Sarwar Islam,Wei Li,Zhi Zeng, L.D.Favro,G.M.Newaz, and R.L Thoms, (2005). Smart Structures and Materials 5767: 2005.
24. Xiaoyan Han, M. S. I., L.D.Favro,G.M.Newaz, and R.L Thoms, (2005). Journal of Applied Physics 98.
25. Xiaoyan Han, M. S. I., L.D.Favro,G.M.Newaz, and R.L Thoms, (2006). J.Appl.Phys.(99): 074905.
26. B.A.Korshak, I. Y. S. a. (2002). Physical Review Letters 88: 014303.
27. http://en.wikipedia.org/wiki/Finite_element_analysis
28. Livermore Software Technology Corporation, *LS-DYNA Keyword User's Manual*, version 970, April 2003.
29. John O. Hallquist, *LS-DYNA Theoretical Manual*, Livermore Software Technology Corporation, May 1998.
30. Xiaoyan Han, Y. R. (2007). Proceedings of the SPIE.
31. Xiaoyan Han, Q. H. (2006). Proceedings of SPIE.
32. Xiaoyan Han, Y. S., and Garrett Godfrey (2008). "Investigation of non-linear effects of coupling materials in sonic IR imaging." Proc.SPIE 6932(69320N).
33. Y.Song, Xiaoyan Han**,** International Journal of Modern Engineering, The Effect of Loading Force on Ultrasound Transducer Non-Linear Coupling in Sonic Infrared Imaging, v14n1,88, 2013.

34. Y.Song, Xiaoyan Han, *International Journal of Engineering Research & Innovation*, Comprehensive Study of the Non-linear Coupling Effects Between An Ultrasound Transducer and A Target Under Inspection in Sonic IR Imaging, v5n1,90, 2013
35. Han Xiaoyan; Zhang Ding; He Qi; Yuyang Song; Lubowicki, Anthony ,Zhao Xinyue; Newaz, Golam. Favro, Lawrence D.; Thomas, Robert L. AIP Conference Proceedings; Journal Volume: 1335; Review of progress in quantitative nondestructive evaluation
36. Auld, B.A. (1973). *Acoustic fields and waves in solids*; Wiley New York:
37. Krautkrämer&J, Krautkrämer.,(1990).*Ultrasonic testing of materials*.(4th) Springer;
38. Xiaoyan Han, *Frequency Dependence of the Thermosonic Effect*, Review of Scientific Instruments, Vol. 74, No. 1, pp. 414-416, January, 2003
39. Cohen, L., Ed. (1995). Time Frequency Analysis. New York, McGRAW-HILL BOOK COMPANY,Inc.
40. Altair Engineering, Inc, *Altair HyperMesh User's Guide,* version 8.0.
41. Altair Engineering, Inc, *Altair HyperMesh Interfacing with LS-DYNA,* version 8.
42. Livermore Software Technology Corporation, *LSPOST a New Post Processor for LS-DYNA*, May 2005
43. Robert D. Cook, David S. Malkus, Michael E. Plesha, Robert J. Witt, Concepts and Applications of *Finite Element Analysis*, fourth edition 2001.
44. John D. Reid, *LS-DYNA Examples Manual*, Livermore Software Technology Corporation, June 2001.
45. Wei's PhD thesis,2008

ABSTRACT

A COMPREHENSIVE STUDY OF NON-LINEAR EFFECTS OF COUPLING MATERIAL IN SONIC INFRARED IMAGING

by

YUYANG SONG

May 2014

Advisor: Dr. Xiaoyan Han

Major: Electrical Engineering

Degree: Doctor of Philosophy

Nondestructive Evaluation (NDE) is a multidisciplinary field of research, which is focused on the development of analysis and measurement technologies for the quantitative characterization of materials, components and structures. It is a key process used in product evaluation, troubleshooting for the quality assurance in industry. Sonic Infrared (IR) Imaging technology is a hybrid sensing and imaging technique, in which cracks in an object are caused to become visible in the infrared imaging through frictional heating associated with the application of a short pulse of low-frequency ultrasound. The technique uses pulses of ultrasonic excitation applied to a sample for a fraction of a second. The heating at the crack is then captured by calibrated infrared cameras using real-time video/digital imaging. It’s been demonstrated that this technique can detect surface and subsurface cracks, delaminations, and disbonds in metallic and composite materials successfully. As a promising NDE technique, ultrasonic Infrared Imaging technique has gain more attention from researchers and technicians in NDE community, it has been used in detecting cracks/defects in the automotive and aerospace industry for several years.

The purpose of the research work is to comprehensively study the non-linear effect of coupling materials used in the technique, where a coupling material is a thin layered material that separates transducer and sample. In this research, a series of coupling materials are investigated, and a comprehensive analysis, using different engagement force or different pulse frequency on two commonly used aluminum samples with different geometries and structures are studied. The combination of vibration waveforms and IR images/signals is used as an analysis method for the comprehensive study. Correlation analysis between the acoustic and thermal energy in the crack is discussed, as well. The finite element analysis is used to predict the thermal-mechanical behavior of the cracks in the samples under different boundary conditions by using different coupling media, different loading force and pulse frequency. FEA results are validated with the test results side by side. It is verified that coupling material can play an important role in crack detection.

AUTOBIOGRAPHICAL STATEMENT

Yuyang Song

Education:

- Ph.D. ECE, Wayne State University, U.S.A. March 2014
- M.S. MSE, Institute of Metal Research, Chinese Academy of Science,July2006
- B.S. MSE, Center South University, Changsha,China,2003

Working Experience:

- Research Scientist, 2011 to current, Toyota Research Institute of North America
- Graduate Research Assistant, 2006-2011, Wayne State University

Publications:

[1] Y.Song, Xiaoyan Han, International Journal of Modern Engineering, V4 (1), 88 2013.

[2] Y.Song,Xiaoyan Han, International Journal of Engineering Research & Innovation, V5(1), 2014

[3] Y.Song, Xiaoyan Han, Infrared Physics &Technology, under review, 2014

[4] Han, Xiaoyan, and Yuyang Song. *AIP Conference Proceedings*. Vol. 1511. 2013.

[5] Yuyang Song, Umesh. Gandhi, ANTEC 2013, April 21, Cincinnati, OH

[6] Song, Yuyang, and Xiaoyan Han. *AIP Conference Proceedings*. Vol. 1430. 2012.

[7] Han Xiaoyan; Zhang Ding; He Qi; Song Yuyang; Lubowicki, Anthony ,Zhao Xinyue; Newaz, Golam. Favro, Lawrence D.; Thomas, Robert L. AIP Conference Proceedings; Journal Volume: 1335; Review of progress in quantitative nondestructive evaluation

[8] YuYang Song, Garrett Godfrey, Xiaoyan Han. Review of Progress in Quantitative Nondestructive Evaluation 2009; 1096:511-517.

[9] Xiaoyan Han, Yuyang Song, Garrett Godfrey. Sensors and Smart Structures Technologies for Civil, Mechanical, and Aerospace Systems 2008